



1 Carbon-concentration and carbon-climate
2 feedbacks in CMIP6 models, and their
3 comparison to CMIP5 models

4
5 Vivek. K. Arora¹, Anna Katavouta², Richard G. Williams², Chris D. Jones³, Victor Brovkin⁴, Pierre
6 Friedlingstein⁵, Jörg Schwinger⁶, Laurent Bopp⁷, Olivier Boucher⁷, Patricia Cadule⁷, Matthew A.
7 Chamberlain⁸, James R. Christian¹, Christine Delire⁹, Rosie A. Fisher¹⁰, Tomohiro Hajima¹¹,
8 Tatiana Ilyina⁴, Emilie Joetzjer⁹, Michio Kawamiya¹¹, Charles Koven¹², John Krasting¹³, Rachel M.
9 Law¹⁴, David M. Lawrence¹⁵, Andrew Lenton⁸, Keith Lindsay¹⁵, Julia Pongratz^{4,16}, Thomas
10 Raddatz⁴, Roland Séférian⁹, Kaoru Tachiiri¹¹, Jerry F. Tjiputra⁶, Andy Wiltshire³, Tongwen Wu¹⁷,
11 Tilo Ziehn¹⁴

12
13 ¹Canadian Centre for Climate Modelling and Analysis, Environment Canada, University of Victoria,
14 Victoria, B.C., V8W 2Y2, Canada

15 ²School of Environmental Sciences, Liverpool University, Liverpool, United Kingdom

16 ³Met Office Hadley Centre, Exeter, United Kingdom

17 ⁴Max Planck Institute for Meteorology, Bundesstraße 53, 20146 Hamburg, Germany

18 ⁵College of Engineering, Mathematics and Physical Sciences, University of Exeter, Exeter, EX4 4QF, UK

19 ⁶NORCE Norwegian Research Centre, Bjerknes Centre for Climate Research, Bergen, Norway

20 ⁷IPSL, CNRS, Sorbonne Université, Paris, France

21 ⁸CSIRO Oceans and Atmosphere, Hobart, Tasmania, Australia

22 ⁹CNRM, Université de Toulouse, Météo-France, CNRS, Toulouse, France

23 ¹⁰National Center for Atmospheric Research, Boulder, CO, USA and Centre Européen de Recherche et de
24 Formation Avancée en Calcul Scientifique, (CERFACS). Toulouse, France.

25 ¹¹Research Institute for Global Change, Japan Agency for Marine-Earth Science and Technology,
26 Yokohama 236-0001, Japan

27 ¹²Climate and Ecosystem Sciences Division, Lawrence Berkeley National Lab, Berkeley California, USA

28 ¹³NOAA/Geophysical Fluid Dynamics Laboratory, Princeton, New Jersey, United States of America

29 ¹⁴CSIRO Oceans and Atmosphere, Aspendale, Victoria, Australia

30 ¹⁵Climate and Global Dynamics Laboratory, National Center for Atmospheric Research, Boulder, CO, USA

31 ¹⁶Ludwig-Maximilians University, Munich

32 ¹⁷Beijing Climate Center, China Meteorological Administration, 46 Zongguancun Nandajie, Haidian
33 District, Beijing, China

34 –

35



36 **Abstract**

37

38 Results from the fully-, biogeochemically-, and radiatively-coupled simulations in which CO₂
39 increases at a rate of 1% per year (1pctCO₂) from its pre-industrial value are analyzed to quantify
40 the magnitude of two feedback parameters which characterize the coupled carbon-climate
41 system. These feedback parameters quantify the response of ocean and terrestrial carbon pools
42 to changes in atmospheric CO₂ concentration and the resulting change in global climate. The
43 results are based on eight comprehensive Earth system models from the fifth Coupled Model
44 Intercomparison Project (CMIP5) and eleven models from the sixth CMIP (CMIP6). The
45 comparison of model results from two CMIP phases shows that, for both land and ocean, the
46 model mean values of the feedback parameters and their multi-model spread has not changed
47 significantly across the two CMIP phases. The absolute values of feedback parameters are lower
48 for land with models that include a representation of nitrogen cycle. The sensitivity of feedback
49 parameters to the three different ways in which they may be calculated is shown and, consistent
50 with existing studies, the most relevant definition is that calculated using results from the fully-
51 and biogeochemically-coupled configurations. Based on these two simulations simplified
52 expressions for the feedback parameters are obtained when the small temperature change in
53 the biogeochemically-coupled simulation is ignored. Decomposition of the terms of these
54 simplified expressions for the feedback parameters allows identification of the reasons for
55 differing responses among ocean and land carbon cycle models.

56

57



58

59 1. Introduction

60

61 The Earth system responds to the perturbation of its atmospheric CO₂ concentration ([CO₂]),
62 caused by anthropogenic fossil fuel and land use change emissions of CO₂ or any other forcing,
63 via both changes in its physical climate and the biogeochemical carbon cycle. Changes in both
64 the physical climate and the biogeochemical carbon cycle affect each other through multiple
65 feedbacks. The surface-atmosphere exchange of CO₂ over both land and ocean is modulated by
66 the changes in physical climate and [CO₂], and the resulting changes in [CO₂] modulates the
67 physical climate, among other climate forcings.

68

69 The response of the Earth's carbon cycle for both land and ocean components has been
70 characterized in terms of carbon-concentration and carbon-climate feedback parameters which
71 quantify their response to changes in [CO₂] and the physical climate, respectively (Friedlingstein
72 et al., 2006; Arora et al., 2013a). The carbon-concentration feedback (β) quantifies the response
73 of the carbon cycle to changes in [CO₂] and is expressed in units of carbon uptake or release per
74 unit change in [CO₂] (PgC ppm⁻¹). The carbon-climate feedback (γ) quantifies the response of the
75 carbon cycle to changes in physical climate and is expressed in units of carbon uptake or release
76 per unit change in global mean temperature (PgC °C⁻¹). The changes in physical climate, in this
77 framework, are expressed simply in terms of changes in global mean near surface air
78 temperature although, of course, the carbon cycle also responds to other aspects of changes in
79 climate (in particular precipitation over land and circulation changes in the ocean). The



80 assumption is that the effect of other aspects of changes in climate on the carbon cycle can be
81 broadly expressed in terms of changes in near surface air temperature. These feedback
82 parameters can be calculated from Earth system model (ESM) simulations globally, separately
83 over land and ocean, regionally, or over individual grid cells (which makes somewhat more sense
84 over land than over ocean) to investigate their geographical distribution (Friedlingstein et al.,
85 2006; Yoshikawa et al., 2008; Boer and Arora, 2010; Tjiputra et al., 2010; Roy et al., 2011; Arora
86 et al., 2013a). The feedback analysis has shown that the carbon-concentration feedback is
87 negative from the atmosphere's perspective. That is, an increase in [CO₂] leads to an increased
88 carbon uptake by land and ocean which leads to a decrease in [CO₂] thereby slowing CO₂
89 accumulation in the atmosphere. The carbon-climate feedback, in contrast, has been shown to
90 be positive in ESM simulations (at the global scale) from the atmosphere's perspective since an
91 increase in temperature decreases the capacity of land and ocean to take up carbon, thereby
92 contributing to a further increase in atmospheric CO₂.

93

94 The carbon-concentration and carbon-climate feedback parameters serve several purposes.
95 First, these feedback parameters allow comparison of models in a simple and straightforward
96 manner despite their underlying complexities and different model structures. Inter-model
97 comparisons, of course, offer several benefits as has been shown for multiple model
98 intercomparison projects (MIPs). Second, they allow the quantification of the contribution of the
99 two feedback processes to allowable anthropogenic emissions for a given CO₂ pathway. For
100 example, Arora et al. (2013) and Gregory et al. (2009) showed that the contribution of the carbon-
101 concentration feedback to allowable diagnosed emissions is about 4-4.5 times larger than the



102 carbon-climate feedback. Third, they allow the comparison of feedbacks between climate and
103 the carbon cycle to other feedbacks operating in the climate system as was done by Gregory et
104 al. (2009). Fourth, the feedback parameters can be considered as emergent properties of the
105 coupled carbon-cycle climate system which can potentially be constrained by observations as
106 Wenzel et al. (2014) attempted for the carbon-climate feedback parameter over land.

107

108 Here, we build on the work done in earlier studies that compared the strength of the carbon-
109 concentration and carbon-climate feedback in coupled general circulation models with land and
110 ocean carbon cycle components. Friedlingstein et al. (2006) (hereafter F06) reported the first
111 such results from the Coupled Climate Carbon Cycle Models Intercomparison Project (C⁴MIP).
112 Arora et al. (2013) (hereafter A13) compared the strength of the carbon-concentration and
113 carbon-climate feedbacks from models participating in the fifth phase of the Coupled Model
114 Intercomparison Project (CMIP5, <http://cmip-pcmdi.llnl.gov/cmip5/forcing.html>, Taylor et al.
115 (2012)). The A13 study found that the strength of the two feedbacks was weaker and the spread
116 between models was smaller in their study than in F06. While this comparison is useful, the
117 primary caveat when comparing results between these two studies is that their results are based
118 on different scenarios. The results from the F06 study were based on the SRES A2 emissions
119 scenario, while those in the A13 study were based on the 1% per year increasing CO₂ experiment
120 in which the atmospheric CO₂ concentration increases from its pre-industrial value of around 285
121 ppm until it quadruples over a 140-year period (referred to as the 1pctCO₂ experiment in the
122 framework of the Coupled Model Intercomparison Project, CMIP). The absolute values of the
123 feedback parameters are known to be dependent on the state of the system, the timescale of



124 forcing (i.e. underlying emissions/concentration scenario) and the approach used to calculate
125 them (Plattner et al., 2008; Gregory et al., 2009; Boer and Arora, 2010; Zickfeld et al., 2011;
126 Hajima et al., 2014). The varying approaches employed over the past decade have made the
127 cross-comparison of feedbacks among the studies and different generations of Earth System
128 Models difficult.

129

130 In order to address the diversity of approaches to diagnose climate carbon cycle feedbacks, and
131 to promote a robust standard moving forward, the C⁴MIP community has endorsed a framework
132 of tiered experiments (Jones et al., 2016) that builds upon the core preindustrial control and
133 1pctCO₂ experiments performed as part of the CMIP DECK (Diagnostic, Evaluation and
134 Characterization of Klima) experiments (Eyring et al., 2016). Here, we compare carbon-
135 concentration and carbon-climate feedbacks from models participating in the C⁴MIP (Jones et al.,
136 2016) contribution to the sixth phase of CMIP (CMIP6, Eyring et al., 2016). To maintain continuity
137 and consistency, feedback parameters are derived from the 1pctCO₂ experiments as was done
138 in A13. The 1pctCO₂ experiment is a DECK experiment in the CMIP6 framework. All participating
139 modelling groups are expected to perform DECK experiments to help document basic
140 characteristics of models across different phases of CMIP (Eyring et al., 2016).

141

142 2. Feedbacks in the coupled climate-carbon system

143

144 We largely follow the climate carbon cycle feedbacks framework presented in A13 (which in turn
145 was built on F06) but with some additional modifications that are explained below. Only the



146 primary equations are presented here while the bulk of the framework is summarized in the
147 Appendix for completeness. We also provide some history of how the carbon feedbacks analysis
148 reached its current stage.

149

150 Carbon feedbacks analysis is traditionally based on simulations run with fully-, radiatively-, and
151 biogeochemically-coupled model configurations of an Earth system model. The objective of these
152 simulations is to isolate feedbacks discussed above. In a biogeochemically-coupled simulation
153 (referred to here as the BGC simulation), biogeochemical processes over land and ocean respond
154 to increasing atmospheric CO₂ while the radiative transfer calculations in the atmosphere use a
155 CO₂ concentration that remains at its preindustrial value. Small climatic changes occur in the BGC
156 simulation due to changes in evaporative (or latent heat) flux resulting from stomatal closure
157 over land (associated with increasing [CO₂]), changes in vegetation structure, and changes in
158 vegetation coverage and composition (in models which dynamically simulate competition
159 between their plant functional types) all of which affect latent and sensible heat fluxes at the
160 land surface. In a radiatively-coupled simulation (referred to here as the RAD simulation)
161 increasing atmospheric CO₂ affects the radiative transfer processes in the atmosphere and hence
162 climate but not the biogeochemical processes directly over land and ocean, for which the
163 preindustrial value of atmospheric CO₂ concentration is prescribed. In a fully-coupled simulation
164 (referred to here as the COU simulation) both the biogeochemical and the radiative processes
165 respond to increasing CO₂.

166



167 Following the F06 methodology which uses time-integrated fluxes (which are the same as the
168 changes in carbon pool sizes), the changes in land (L) or ocean (O) carbon pools (ΔC_X , $X = L, O$)
169 can be expressed using three equations corresponding to the BGC, RAD, and COU experiments,
170 as shown in equation (1) (see also the Appendix).

171

172 Radiatively coupled simulation $\Delta C_X^+ = \int F_X^+ dt = \gamma_X T^+$ (1a)

173 Biogeochemically coupled simulation $\Delta C_X^* = \int F_X^* dt = \beta_X c' + \gamma_X T^*$ (1b)

174 Fully coupled simulation $\Delta C_X' = \int F_X' dt = \beta_X c' + \gamma_X T'$ (1c)

175

176 where F^+ , F^* , and F' are the CO₂ flux changes (PgC year⁻¹), ΔC_X^+ , ΔC_X^* , and $\Delta C_X'$ the changes in
177 global carbon pools (PgC), and T^+ , T^* , and T' the temperature changes (°C) in the RAD, BGC, and
178 COU simulations, respectively, and the subscript $X = L, O$ refers to either the land or ocean
179 model components. c' is the change in [CO₂]. Here and elsewhere uppercase C is used to denote
180 pools and lowercase c is used to denote atmospheric CO₂ concentration, [CO₂]. All changes are
181 defined relative to a pre-industrial equilibrium state represented by the pre-industrial control
182 simulation. In the context of a specified-concentration simulation (the 1pctCO₂ experiment in
183 our case), c' is the same in BGC and COU simulations. There is no $\beta_X c'$ term in the RAD simulation
184 since the biogeochemistry sees pre-industrial value of [CO₂] and therefore $c' = 0$ although T^+ is
185 a function of increasing c' that is seen only by the radiative transfer calculations.

186

187 These equations assume linearization of the globally integrated surface-atmosphere CO₂ flux (for
188 land and ocean components) in terms of global mean temperature and [CO₂] change (compared



189 to a pre-industrial control run) and serve to define the carbon-concentration (β_X) and carbon-
190 climate (γ_X) feedback parameters. A similar set of equations can be written that define the
191 instantaneous values of the feedback parameters and is based on fluxes rather than their time-
192 integrated values (see equations A4 and A5 in the appendix). Both the time-integrated flux and
193 instantaneous flux based versions of the feedback parameters evolve over time as shown in A13.

194

195 There are several different ways in which the feedbacks (β_X and γ_X) in a coupled climate and
196 carbon cycle system may be evaluated: 1) the experiments may use specified (concentration-
197 driven) or freely evolving (emissions-driven) $[\text{CO}_2]$, 2) any two of the three configurations of an
198 experiment (COU, RAD, and BGC) may be used to calculate the two feedback parameters, and 3)
199 the experiment may be based on an idealized scenario (like the 1pctCO₂ experiment) or a more
200 realistic emissions scenario. In addition, the small temperature change in the BGC simulation, T^* ,
201 may be ignored, and other external forcings such as nitrogen (N) deposition, or land use change,
202 which directly affect carbon fluxes may or may not be taken into account. The original framework
203 proposed by F06 used COU and BGC versions (referred to as coupled and uncoupled in the F06
204 study) of an emissions driven simulation for the SRES A2 scenario. The F06 framework assumed
205 that the small temperature change in the BGC simulation can be ignored. A13 used BGC and RAD
206 versions of the 1pctCO₂ experiment in which the evolution of $[\text{CO}_2]$ is specified and took into
207 account the small global mean temperature change in the BGC simulation.

208

209 With regard to the use of concentration-driven versus emissions-driven simulations, Gregory et
210 al. (2009) recommended the use of specified concentration simulations, which ensures



211 consistency of [CO₂] across models, and this recommendation has now been adopted since
212 CMIP5. C⁴MIP has also adopted the use of the 1pctCO₂ simulation, i.e., an idealized scenario is
213 preferred over a more realistic scenario. This recommendation was also made by Gregory et al.
214 (2009). The 1pctCO₂ experiment provides an ideal experiment to compare carbon-climate
215 interactions across models as the experiment does not include the confounding effects of other
216 climate forcings (including land use change, non-CO₂ greenhouse gases, and aerosols) and is a
217 CMIP DECK experiment, as mentioned earlier.

218

219 Using equation (1) as an example, Table 1 shows how any two combinations of the three
220 configurations of an experiment can be used to calculate the values of the two feedback
221 parameters. The A13 study showed that under the assumption of a linear system and if the
222 conditions $F' = F^+ + F^*$ and $T' = T^+ + T^*$ are met, i.e. if the sum of flux and temperature changes
223 in the RAD and BGC simulations is the same as that in the COU simulation, then all approaches
224 yield exactly the same solution. However, this is not the case because of the non-linearities
225 involved (see also Schwinger et al., 2014).

226

227 The use of BGC and RAD simulations that have only biogeochemistry or radiative forcing
228 responding to increases in [CO₂] to find the feedback parameters is attractive since these
229 simulations were designed to isolate the feedbacks. In the RAD simulation (whose purpose is to
230 quantify the carbon-climate feedback, γ_X) the pre-industrial global carbon pools for both land
231 and ocean typically decrease in response to an increase in global temperature (hence the positive
232 carbon-climate feedback and the negative value of γ_X). Consequently, negative values of γ_X



233 (positive carbon-climate feedback) are obtained when using the RAD-BGC and RAD-COU
234 approaches (see Table 1). If, however, γ_X is determined using the BGC-COU approach, then γ_X is
235 calculated using BGC and COU simulations in both of which the globally-summed carbon pools
236 for land and ocean are increasing in response to increasing $[\text{CO}_2]$. As a result, the calculated value
237 of γ_X is different than that obtained using the RAD-BGC and RAD-COU approaches. In the ocean,
238 the RAD simulation mainly measures the loss of near-surface carbon owing to warming of the
239 surface ocean layer (Schwinger et al., 2014). The RAD simulation misses the suppression of
240 carbon drawdown to the deep ocean due to weakening ocean circulation, because there is no
241 buildup of a strong carbon gradient from the surface to the deep ocean in contrast to the BGC
242 and COU simulations. Therefore, the absolute value of γ_X is smaller (less negative) when
243 calculated using the RAD simulation (Schwinger et al., 2014). Over land, in the RAD simulation
244 carbon is lost in response to increasing temperatures primarily due to an increase in
245 heterotrophic respiration. However, an increase in temperature also potentially increases
246 photosynthesis at high latitudes, and this increase compensates for carbon lost due to increased
247 heterotrophic respiratory losses, especially in the presence of continuously increasing $[\text{CO}_2]$ seen
248 in the COU configuration. These are some mechanisms that lead to non-linearities. Since the
249 ongoing climate change (predominantly caused by increasing $[\text{CO}_2]$) is best characterized by the
250 COU simulation, it can be argued that feedback parameters are more representative when
251 calculated using the BGC-COU approach. Here, we propose to use the COU and BGC
252 configurations of an experiment as the standard set from which to calculate the feedback
253 parameters as recommended in the C⁴MIP protocol (Jones et al., 2016). However, we also
254 quantify the values of feedback parameters when using the RAD simulation for comparison. The



255 calculated values of the carbon-concentration feedback parameter (β_X) in contrast, are less
256 sensitive to the approach used as shown in A13.

257

258 There is no broad consensus on whether temperature change in the BGC simulation should be
259 assumed to be zero ($T^* = 0$) as standard practice when calculating the strengths of the
260 feedbacks, as done in F06. While the globally-averaged value of T^* is an order of magnitude
261 smaller than T' , the spatial pattern of T^* is quite different from that of T' . The spatial pattern of
262 temperature change in the COU simulation (T') is dominated by radiative forcing of increased
263 $[\text{CO}_2]$ with greater warming at high latitudes and over land than over ocean. In contrast, the
264 spatial pattern of temperature change in the BGC simulation (T^*) is determined primarily by
265 reduction in latent heat flux associated with stomatal closure as $[\text{CO}_2]$ increases which reduces
266 transpiration from vegetation (Ainsworth and Long, 2005; Bounoua et al., 1999). This process
267 leads to a much more spatially variable pattern of temperature change (than T') and the
268 associated changes in precipitation patterns due to soil moisture-atmosphere feedbacks
269 (Chadwick et al., 2017; Skinner et al., 2017). The difference in spatial patterns of temperature
270 and precipitation change in the RAD versus the COU simulation is another reason that the values
271 of the carbon-climate feedback (γ_X) depend on the simulation used, and this is another pathway
272 for non-linearities to occur. A complete analysis of the effect of differences in spatial patterns of
273 climate change and the carbon state on the calculated value of γ_X when using the RAD versus
274 the COU simulation, and if or not the assumption of $T^* = 0$ should be a standard practice, is
275 beyond the scope of this study but remains a topic for additional scientific investigation. In the



276 interim, we report here values of β_X and γ_X by explicitly considering T^* but also assuming $T^* =$
277 0.

278

279 Following Table 1, when using results from the BGC and the COU versions of a specified-
280 concentration experiment the values of the feedback parameters are written as

281

$$282 \quad \beta_X = \frac{1}{c'} \left(\frac{\Delta C_X^* T' - \Delta C_X' T^*}{T' - T^*} \right) \quad (2)$$

$$283 \quad \gamma_X = \frac{\Delta C_X' - \Delta C_X^*}{T' - T^*} \quad (3)$$

284

285 Equations (2) and (3) may be rearranged to explicitly calculate the effect of the $T^* = 0$
286 assumption on calculated values of feedback parameters, as shown in equations (4) and (5). Here,
287 the T^* term is retained only in the second part of the equations whose contribution becomes
288 zero when T^* is ignored.

289

$$290 \quad \beta_X = \frac{\Delta C_X^*}{c'} + \frac{1}{c'} \left[\frac{(\Delta C_X' - \Delta C_X^*) T^*}{(T' - T^*)} \right] \quad (4)$$

$$291 \quad \gamma_X = \frac{\Delta C_X' - \Delta C_X^*}{T'} + \frac{(\Delta C_X' - \Delta C_X^*) T^*}{T' (T' - T^*)} \quad (5)$$

292

293 Finally, in regards to other external forcings such as nitrogen (N) deposition that directly affect
294 carbon fluxes, the C⁴MIP protocol for CMIP6 (Jones et al., 2016) recommended performing
295 additional simulations for BGC and COU versions of the 1pctCO₂ experiment with time varying N
296 deposition in addition to their standard versions which keep N deposition rates at their pre-
297 industrial level. Simulations with N deposition can only be performed for models that explicitly



298 model the N cycle and its interactions with the carbon (C) cycle. The rationale for recommending
299 increasing N deposition, in conjunction with temperature and CO₂ increase, is to be able to
300 quantify the response of feedback parameters to this third forcing. However, here we restrict
301 ourselves to the traditional analysis that considers the climate and CO₂ forcings only. We do
302 highlight, however, which models include coupled C-N cycle interactions over land. Analysis of
303 runs with N deposition forcing is left for future studies.

304

305 2.1. Reasons for differences in feedback parameters among models

306

307 As shown later in this paper, the contribution of the second term involving T^* in expressions for
308 the carbon-concentration (β_X) and carbon-climate (γ_X) feedback parameters (in equations 4 and
309 5, when using the BGC-COU approach) is around 1% to 5%. This allows to investigate reasons for
310 differences in the feedback parameters across models as the expressions for the feedback
311 parameters can be simplified in terms of the changes in the sizes of carbon pools ($\Delta C'_X$ and ΔC^*_X),
312 the temperature change in the COU simulation (T') and the specified change in [CO₂] (c') as
313 follows.

314

$$315 \quad \beta_X \approx \frac{\Delta C^*_X}{c'} \quad (6)$$

$$316 \quad \gamma_X \approx \frac{\Delta C'_X - \Delta C^*_X}{T'} \quad (7)$$

317

318

319 2.1.1 Land



320

321 Over land, equations (6) and (7) can be expanded to investigate, firstly, the contributions from
 322 changes in live vegetation pool (ΔC_V) and dead litter plus soil carbon pools (ΔC_S), to the strength
 323 of the feedback parameters, since $\Delta C_L = \Delta C_V + \Delta C_S$. Secondly, equation (6) can be further
 324 decomposed to gain insight into the reasons for differences across models, in a manner similar
 325 to Hajima et al. (2014).

$$\begin{aligned}
 327 \quad \beta_L &\approx \frac{\Delta C_L^*}{c'} = \frac{\Delta C_V^* + \Delta C_S^*}{c'} = \left(\frac{\Delta C_V^*}{\Delta NPP^*} \frac{\Delta NPP^*}{\Delta GPP^*} \frac{\Delta GPP^*}{c'} \right) + \left(\frac{\Delta C_S^*}{\Delta R_h^*} \frac{\Delta R_h^*}{\Delta LF^*} \frac{\Delta LF^*}{c'} \right) \\
 328 \quad &= \tau_{veg\Delta} \cdot CUE_{\Delta} \cdot \frac{\Delta GPP^*}{c'} + \tau_{soil\Delta} \frac{\Delta R_h^*}{\Delta LF^*} \frac{\Delta LF^*}{c'} \quad (8)
 \end{aligned}$$

$$329 \quad \gamma_L \approx \frac{\Delta C'_L - \Delta C_L^*}{T'} = \frac{\Delta C'_V - \Delta C_V^*}{T'} + \frac{\Delta C'_S - \Delta C_S^*}{T'} \quad (9)$$

329 The superscript * in equation (8) implies that the terms are calculated here using the BGC version
 330 of the 1pctCO2 experiment. In equation (8), ΔNPP and ΔGPP represent the change in net and
 331 gross primary productivity, ΔLF the change in litterfall flux, and ΔR_h the change in heterotrophic
 332 respiration, compared to the preindustrial control experiment. The multiplicative terms in
 333 equation (8) do indeed have some physical meaning although they are based on change in the
 334 magnitude of quantities as opposed to their absolute magnitudes. We note here explicitly that
 335 as such, these terms cannot be compared directly to the terms which are based on absolute
 336 magnitudes.

337 The term $\frac{\Delta NPP}{\Delta GPP}$ (fraction) is the fraction of GPP (above its pre-industrial value) that is turned into
 338 NPP after autotrophic respiratory losses are taken into account. We use the term carbon use



339 efficiency but subscripted by Δ (CUE_{Δ}) to represent $\frac{\Delta NPP}{\Delta GPP}$. The subscripted Δ allows CUE_{Δ} to be
340 differentiated from CUE as used in the existing literature (Choudhury, 2000) which represents
341 the fraction of absolute GPP that is converted to NPP rather than its change over some time
342 period, as well as the point that we consider globally-integrated rather than locally-derived
343 quantities. Similarly, the term $\frac{\Delta C_V}{\Delta NPP}$ represents a measure of turnover or residence timescale of
344 carbon in the vegetation pool ($\tau_{veg\Delta}$, years). The term $\frac{\Delta GPP}{c'}$ ($\text{PgC yr}^{-1} \text{ppm}^{-1}$) is a measure of the
345 strength of the globally-integrated CO_2 fertilization effect. However, in the models that
346 dynamically simulate changes in vegetation cover, the effect of changes in vegetation coverage is
347 implicitly included in this term. The term $\frac{\Delta C_S}{\Delta R_h}$ is a measure of the average residence time of carbon
348 in the dead litter and soil carbon pools ($\tau_{soil\Delta}$, years). However, as with CUE , this quantity cannot
349 be compared directly to the residence time of carbon in the litter plus soil carbon pool calculated
350 using the absolute values of C_S and R_h . Nor can it be compared to the changes in carbon residence
351 time due to the “false priming effect” associated with the increase in NPP inputs, as $[\text{CO}_2]$
352 increases, into the dead carbon pools (Koven et al., 2015). $\frac{\Delta R_h}{\Delta LF}$ (fraction) is a measure of the
353 increase in heterotrophic respiration per unit increase in litterfall rate, and $\frac{\Delta LF}{c'}$ ($\text{PgC yr}^{-1} \text{ppm}^{-1}$)
354 indicates global increase in litterfall rate per unit increase in CO_2 , which in principle, should be
355 close to the change in net primary productivity per unit increase in CO_2 , ($CUE_{\Delta} \frac{\Delta GPP}{c'}$).
356 Comparison of these terms across models can potentially yield insight into the reasons for large
357 differences in land carbon uptake across models.

358



359 2.1.2 Ocean

360

361 The change in the ocean carbon inventory, ΔC_o , is defined by an integral of the change in the
362 dissolved inorganic carbon, ΔDIC , and density over the ocean volume,

363
$$\Delta C_o = 12 \text{ gC mol}^{-1} \int_V \Delta DIC \, dV \times 10^{-15} \quad (10)$$

364 where ΔC_o is in PgC, the ocean dissolved inorganic carbon, DIC in mol m⁻³ and the ocean volume
365 V in m³, and the multiplier 10^{-15} converts g to Pg of carbon.

366 To gain insight into how the ocean carbon distribution is controlled, the ocean dissolved inorganic
367 carbon, DIC , may be defined in terms of separate carbon pools (Ito and Follows, 2005; Williams
368 and Follows, 2011; Lauderdale et al., 2013; Schwinger and Tjiputra, 2018):

369
$$\begin{aligned} DIC &= DIC_{preformed} + DIC_{regenerated} \\ &= DIC_{sat} + DIC_{disequilib} + DIC_{regenerated} \end{aligned} \quad (11)$$

370 where the preformed carbon, $DIC_{preformed}$, is the amount of carbon in a water parcel when in
371 the mixed layer at the time of subduction, and the regenerated carbon, $DIC_{regenerated}$, is the
372 amount of dissolved inorganic carbon accumulated below the mixed layer due to biological
373 regeneration of organic carbon. The preformed carbon is affected by the carbonate chemistry
374 and ocean physics. To gain further insight into how close the ocean is to an equilibrium with the
375 atmosphere, the preformed carbon, $DIC_{preformed}$, is further split into saturated, DIC_{sat} , and
376 disequilibrium, $DIC_{disequilib}$ components. The saturated component represents the
377 concentration in surface water fully equilibrated with the contemporary atmospheric CO₂



378 concentration. The disequilibrium component represents the extent that surface water is
379 incompletely equilibrated before subduction, which is affected by the strength of the ocean
380 circulation altering the residence time in the mixed layer and the ocean ventilation rate. Each of
381 these components is affected by the increase in atmospheric CO₂ and the changes in climate.

382

383 The change in the global ocean carbon inventory, ΔC_O , relative to the preindustrial may then be
384 related to the global volume integral of the change in each of these DIC pools,

$$\begin{aligned} \Delta C_O &= \Delta C_{preformed} + \Delta C_{regenerated} \\ &= \Delta C_{sat} + \Delta C_{disequib} + \Delta C_{regenerated} \end{aligned} \quad (12)$$

386 where $\Delta C_{preformed}$ is the preformed carbon inventory, ΔC_{sat} is the saturated carbon inventory,
387 $\Delta C_{disequib}$ is the disequilibrium carbon inventory and $\Delta C_{regenerated}$ is the regenerated carbon
388 inventory.

389

390 The simplified expressions for carbon-cycle feedback parameters (6) and (7) based on the air-sea
391 flux changes to the ocean may then be approximated by the global ocean carbon inventory
392 changes, which may be expressed in terms of these different global ocean carbon pools
393 (Williams et al., 2019):

$$\begin{aligned} \beta_O &\approx \frac{\Delta C_O^*}{C'} = \frac{\Delta C_{preformed}}{C'} + \frac{\Delta C_{regenerated}}{C'} \\ &= \frac{\Delta C_{sat}}{C'} + \frac{\Delta C_{disequib}}{C'} + \frac{\Delta C_{regenerated}}{C'} \end{aligned} \quad (13)$$



$$\begin{aligned}
 \gamma_O &\approx \frac{\Delta C'_O - \Delta C^*_O}{T'} = \frac{\Delta C'_{preformed} - \Delta C^*_{preformed}}{T'} + \frac{\Delta C'_{regenerated} - \Delta C^*_{regenerated}}{T'} \\
 &= \frac{\Delta C'_{sat} - \Delta C^*_{sat}}{T'} + \frac{\Delta C'_{disequib} - \Delta C^*_{disequib}}{T'} + \frac{\Delta C'_{regenerated} - \Delta C^*_{regenerated}}{T'}
 \end{aligned}
 \tag{14}$$

The anomalies for each of these carbon pools are calculated as

$$\Delta DIC_{regenerated} = -R_{CO} \Delta AOU + \frac{1}{2} (\Delta Alk - \Delta Alk_{pre} - R_{NO} \Delta AOU)
 \tag{15}$$

$$\Delta DIC_{sat} = f(pCO_2^{atm}, T_o, S_o, P, Si, Alk_{pre})_t - f(pCO_2^{atm}, T_o, S_o, P, Si, Alk_{pre})_{t=0}
 \tag{16}$$

$$\Delta DIC_{disequib} = \Delta DIC - \Delta DIC_{regenerated} - \Delta DIC_{sat}
 \tag{17}$$

where R_{CO} and R_{NO} are constant stoichiometric ratios, ΔAOU is the change in apparent oxygen utilization from its pre-industrial value (where preformed oxygen is assumed to be approximately saturated with respect to atmospheric oxygen), ΔAlk is the change in alkalinity, T_o and S_o are the ocean temperature and salinity, respectively, P and Si are the phosphate and silicate concentrations, and ΔAlk_{pre} is the change in preformed alkalinity (Ito and Follows, 2005; Appendix of Lauderdale et al., 2013; Williams and Follows, 2011). In equation (16), ΔDIC_{sat} is calculated using values of pCO_2^{atm} , T_o , S_o , P , Si , and Alk_{pre} at time t and the pre-industrial values at time $t=0$. The preformed alkalinity is estimated from a multiple linear regression using salinity and the conservative tracer PO ($PO=O_2-R_{O_2:P}$) (Gruber et al., 1996), with the coefficients of this regression estimated based on the upper ocean (first 10 meters) alkalinity, salinity, oxygen and phosphate in each model. The small contribution from minor species (borate, silicate, phosphate) to the alkalinity is removed from the total alkalinity before using it for estimates of the carbon system following the algorithm of (Follows et al., 2006). Our diagnostics of the ocean feedbacks



414 and carbon pools depend primarily upon changes in DIC, the preformed and regenerated pools,
415 relative to the pre industrial, although differences in the pre-industrial ocean do slightly affect
416 the saturated DIC due to the non-linearity of the carbonate chemistry.

417

418 3. Model descriptions

419

420 Table 2 summarizes the primary features of the eleven comprehensive ESMs that contributed
421 results to this study. Brief descriptions of land and ocean carbon cycle components of these ESMs
422 are provided in the Appendix. The eleven ESMs, in alphabetical order, are the 1) Commonwealth
423 Scientific and Industrial Research Organisation (CSIRO) ACCESS-ESM1.5, 2) Beijing Climate Centre
424 (BCC) BCC-CSM2-MR, 3) Canadian Centre for Climate Modelling and Analysis (CCCma) CanESM5,
425 4) Community Earth System Model, version 2 (CESM2), 5) Centre National de Recherches
426 Météorologiques (CNRM) CNRM-ESM2-1, 6) Institut Pierre-Simon Laplace (IPSL) IPSL-CM6A-LR,
427 7) Japan Agency for Marine-Earth Science and Technology (JAMSTEC) in collaboration with the
428 University of Tokyo and the National Institute for Environmental Studies (Team MIROC) MIROC-
429 ES2L, 8) Max Planck Institute for Meteorology (MPI) MPI-ESM1.2-LR, 9) Geophysical Fluid
430 Dynamics Laboratory (GFDL) NOAA-GFDL-ESM4, 10) Norwegian Climate Centre (NCC) NorESM2-
431 LM, and 11) United Kingdom (UK) UKESM1-0-LL.

432

433 In contrast to the A13 study where only two of the eight participating comprehensive ESMs had
434 terrestrial N cycle implemented and coupled to their C cycle, in this study six of the eleven



435 participating ESMs represent coupling of terrestrial C and N cycles. These six models are the
436 ACCESS-ESM1.5, CESM2, MIROC-ES2L, MPI-ESM1.2-LR, NorESM2-LM, and UKESM1-0-LL. Note
437 that CESM2 and NorESM2-LM employ the same land surface component – the version 5 of the
438 Community Land Model (CLM5) so we expect the land carbon cycle to respond very similarly in
439 the two models. Three of the ESMs have land components which dynamically simulated
440 vegetation cover and competition between their PFTs - NOAA-GFDL-ESM4, MPI-ESM1.2-LR, and
441 UKESM1-0-LL.

442

443 4. Results

444

445 4.1. Global surface CO₂ fluxes and temperature change

446

447 Figure 1 shows the simulated changes in temperature in the three model configurations (COU,
448 BGC, and RAD) of the 1pctCO₂ experiment. The values show the model mean and the range
449 across the ten participating models, since results from the RAD configuration of the NorESM2-
450 LM model were not available at the time of writing of this manuscript. Here and in subsequent
451 figures, model mean results are also shown for the eight comprehensive ESMs that participated
452 in the A13 study to allow a direct comparison between CMIP5 and CMIP6 models. The eight
453 models in the A13 study are a subset of eleven models considered in this study although they
454 have been updated since CMIP5.

455



456 As expected, temperature change is higher in the COU and RAD simulations, than in the BGC
457 simulation, since the radiative forcing responds to increasing [CO₂] in these simulations. The small
458 temperature change in the BGC simulation is due to a number of contributing but also
459 compensating factors: 1) reduction in transpiration, and hence latent heat flux, due to stomatal
460 closure in response to increasing [CO₂] (Cao et al., 2010), 2) increase in vegetation leaf area index
461 (LAI), which decreases land surface albedo and hence increases absorbed solar radiation, 3)
462 increase in vegetation fraction in models that explicitly simulate competition between their plant
463 functional types (PFTs) over land (NOAA-GFDL-ESM4, MPI-ESM1.2-LR, and UKESM1-0-LL) which
464 also leads to reduced land surface albedo. As a result, temperature change in the COU simulation
465 is higher than in the RAD simulation since these biogeochemical processes are active and
466 contribute to a small additional warming. This is seen in panel (a) for CMIP6 models and panel
467 (b) for CMIP5 models.

468

469 When comparing CMIP5 and CMIP6 models, the CMIP6 models are on average slightly warmer
470 than CMIP5 models in the COU and RAD simulations. In Figure 1a, the globally-averaged near
471 surface temperature change at CO₂ quadrupling in the fully-coupled simulation is 5.00 °C (4.87
472 °C when NorESM2-LM is included) in CMIP6 models, compared to 4.74 °C in CMIP5 models. The
473 globally-averaged temperature change at CO₂ quadrupling in the fully-coupled simulation for the
474 eight models that are common to this (CMIP6) and the A13 (CMIP5) studies, are 4.97 and 4.74
475 °C, respectively. The temperature change in the BGC simulation in CMIP6 models (0.24 °C) is,
476 however, slightly smaller than in the CMIP5 models (0.26 °C). The values in Figure 1 for
477 participating CMIP5 models are slightly different than those reported in A13 study because those



478 numbers also included the UVic Earth System Climate Model (an intermediate complexity model)
479 which we have omitted here to keep the comparison consistent between comprehensive ESMs.
480 In addition, in contrast to A13, the temperature at the end of a simulation in this study is
481 calculated after fitting a polynomial to the model mean values rather than using the actual model
482 mean value at the end of the simulation which can be higher or lower than that calculated using
483 the polynomial fit due to inter-annual variability.

484

485 Figure 2 and 3 show simulated model mean values and the range across models for annual
486 simulated atmosphere-land and atmosphere-ocean CO₂ fluxes and their cumulative values for
487 participating CMIP6 and CMIP5 models from the fully-, biogeochemically- and radiatively-
488 coupled configurations of the 1pctCO₂ experiment. Here, in contrast to Figure 1, results from all
489 eleven models are included since model mean cumulative atmosphere-land and atmosphere-
490 ocean CO₂ fluxes are not particularly sensitive to inclusion/exclusion of the NorESM2-LM models
491 for which results from the RAD simulation were not available. The general results from CMIP6
492 models are broadly similar in nature to those from CMIP5 models, as would be expected, with
493 higher annual and cumulative values of atmosphere-land and atmosphere-ocean CO₂ fluxes in
494 the BGC simulation compared to the COU simulation in which the radiative warming caused by
495 increasing CO₂ weakens the land and ocean sinks. In the RAD simulation, where land and ocean
496 carbon cycle components do not respond to increasing [CO₂], both components lose carbon, for
497 reasons discussed below.

498



499 Over land, the model mean rate of increase of atmosphere-land CO₂ flux declines and even
500 becomes negative in the COU and BGC simulations as the terrestrial CO₂ fertilization effect
501 saturates and the carbon pools build up, which increases the respiratory losses. The biggest
502 difference between the CMIP5 and CMIP6 models is that the cumulative land carbon uptake in
503 the COU simulation is about 25 % higher in CMIP6 (635 ± 258 PgC, mean \pm standard deviation)
504 models than in CMIP5 (505 ± 297 PgC) models, although this increase is not statistically significant
505 across the model ensemble (Mann-Whitney test). The cumulative value of carbon loss in the RAD
506 simulation is similar in both CMIP6 and CMIP5 models, 250 ± 121 vs. 252 ± 158 PgC, respectively.
507 This carbon loss occurs due both to increased heterotrophic respiration per unit carbon mass and
508 reduced GPP (and consequently NPP) in the RAD simulation (not shown). While NPP declines
509 globally in response to increase in temperature, mid- to high-latitude net primary production
510 increases (Qian et al., 2010) so the reduction in global NPP comes largely from the reduction in
511 the tropics. The large range across land carbon cycle models, seen also in earlier F06 and A13
512 studies, has not meaningfully declined for CMIP6 models participating in this study and its
513 implications will be discussed in more detail in Section 5. This is also seen later in Figure 6 which
514 compares the absolute magnitude and the standard deviation of the strength of the feedback
515 parameters from CMIP5 and CMIP6 models.

516

517 Over the ocean, the response to increasing [CO₂] and changing climate remains fairly similar
518 across CMIP5 and CMIP6 models. The cumulative ocean carbon uptake in the COU simulation is
519 593 ± 54 and 611 ± 50 PgC in CMIP6 and CMIP5 models, respectively. Unlike the land uptake,
520 however, the ocean carbon uptake does not saturate over the length of the simulation in the BGC



521 simulation (Figure 3, panels a and b); it keeps on increasing albeit at a declining rate. The
522 cumulative ocean carbon loss in the RAD simulation is 23 ± 19 and 37 ± 17 PgC in CMIP6 and
523 CMIP5 models, respectively, and associated with warmer temperatures which reduce CO₂
524 solubility (Goodwin and Lenton, 2009).

525

526 Figure 4 shows results from individual CMIP6 models for which model means and ranges were
527 shown in Figures 1, 2, and 3. Figure 4 allows identification of models which behave differently
528 compared to the majority of models. In Figure 4, panels a and c, CanESM5 shows the largest
529 temperature increase, and NorESM2-LM and MIROC-ES2L the smallest, in response to increase
530 in [CO₂] for the COU and RAD simulations, respectively. For cumulative atmosphere-land CO₂ flux
531 in the COU simulation (panel d), CanESM5 simulates the largest land carbon uptake and ACCESS-
532 ESM1.5 the smallest. This is not the case for the BGC simulation (panel e) where land carbon
533 uptake from the BCC-CSM2-MR and CNRM-ESM2.1 are the largest among all models, while land
534 carbon uptake from the ACCESS-ESM1.5 is the lowest. Finally, in the RAD simulation (panel f) the
535 loss of carbon from land in response to increasing temperatures is lowest in the MPI-ESM1.2-LR
536 and largest in the BCC-CSM2-MR. Over the ocean, while most models behave very similarly, the
537 carbon uptake in the BCC-CSM2-MR, ACCESS-ESM1.5, and NOAA-GFDL-ESM4 are larger than
538 most models in the COU and BGC simulations. In the RAD simulation, almost all models simulate
539 a loss of carbon from the ocean, but the CNRM-ESM2.1 shows a small uptake. Reasons for
540 divergent response of some models are presented later.

541



542 As in F06 and A13, the range in cumulative atmosphere-land CO₂ fluxes among models at the end
543 of the simulation, in response to changes in atmospheric CO₂ concentration and surface
544 temperature, is three to four times larger than for the atmosphere-ocean CO₂ fluxes.

545

546 4.2. Carbon budget terms

547

548 Figure 5a shows the carbon budget components of the diagnosed cumulative fossil fuel emissions
549 at the end of the 140-year period of the 1pctCO₂ COU experiment when CO₂ concentration
550 quadruples ($\tilde{E}_{4\times\text{CO}_2}$ or simply \tilde{E}), from CMIP6 models. Cumulative emissions can similarly also
551 be calculated at 2×CO₂ ($\tilde{E}_{2\times\text{CO}_2}$). The term “carbon budget” in this context refers to the
552 accounting of carbon internal to individual ESMs. The sum of ocean ($\Delta C'_O$) and land ($\Delta C'_L$) sinks
553 and the resulting atmospheric CO₂ growth rate ($\Delta C'_A$) yields cumulative fossil fuel emissions
554 which are consistent with the specified CO₂ pathway (the 1pctCO₂ scenario in this case) as
555 indicated in the appendix. The corollary to this is that, in a specified emissions simulation, if the
556 respective fossil fuel emissions were to be used in their models, each model will yield CO₂
557 concentrations that rise at a rate of 1% per year. The term “diagnosed” implies that the
558 cumulative fossil fuel emissions are calculated after the fact from changes in atmosphere, land
559 and ocean carbon pools in the specified-concentration 1pctCO₂ experiment. In Figure 5a, the
560 results are arranged in an ascending order according to models’ diagnosed cumulative fossil fuel
561 emissions. Figure 5b shows the terms of the budgets as fractional components for atmosphere
562 (A), land (L) and ocean (O) based on equation (A7), where f_A is the airborne fraction of emissions



563 and f_L and f_O are the fractions of emissions take up by land and ocean, respectively. More details
564 are provided in the Appendix.

$$565 \quad \Delta C'_A + \Delta C'_L + \Delta C'_O = \int_0^t E dt = \tilde{E} \quad (18)$$

$$566 \quad f_A + f_L + f_O = 1 \quad (19)$$

567 All panels in Figure 5 identify models whose land component includes a representation of the N
568 cycle – the cumulative land carbon uptake (panels a and c) and fractional emissions taken up by
569 land (panels b and d) for these models are shown in red. Finally, model mean values are also
570 shown for all models and for models whose land components include and do not include a
571 representation of the land N cycle. For comparison, panels c and d in Figure 5 show the same
572 results but for CMIP5 models reported in A13.

573

574 Consistent with Figure 4, and CMIP5 results reported in the A13 study, the differences among
575 models are primarily due to the diverse response of the land carbon cycle components. While
576 the model mean cumulative carbon uptake by the ocean is fairly similar between participating
577 CMIP5 (611 ± 50 PgC) and CMIP6 (593 ± 54 PgC) models, the land uptake is higher in CMIP6 (635
578 ± 258 PgC) compared to CMIP5 (505 ± 297 PgC) models, as mentioned earlier. This is the case
579 even when the CanESM5, the model with the largest land carbon uptake, is omitted from CMIP6
580 models (model mean land carbon uptake for the remaining ten models is 578 ± 185 PgC). As a
581 result, model mean cumulative diagnosed emissions from CMIP6 models (3031 ± 242 PgC) are
582 about 4% higher than for CMIP5 models (2927 ± 294 PgC). In Figure 5a, the land carbon uptake



583 in CESM2 (656 PgC) and NorESM2-LM (652 PgC) model are very similar; as noted above these
584 models employ the same land component.

585

586 Model mean estimates that are reported separately for models whose land component do and
587 do not include a representation of N cycle, for both CMIP5 and CMIP6 models, show that model-
588 mean land carbon uptake is lower for models that explicitly represent the N cycle. As a
589 consequence, the airborne fraction of emissions is also higher for models that represent land N
590 cycle and their diagnosed cumulative fossil fuel emissions are lower (Figure 5).

591

592 Figure 5a and 5c allow direct comparison of models from the same modelling group. CanESM2,
593 from the Canadian Centre for Climate Modelling and Analysis, which had below average land
594 carbon uptake among CMIP5 models, has evolved to CanESM5, a model with the largest land
595 carbon uptake among CMIP6 models. The reason for this is an increase in the strength of its CO₂
596 fertilization effect as explained in Arora and Scinocca (2016). CESM1, which had one of the lowest
597 land carbon uptake among CMIP5 models, because of its apparently excessive nitrogen limitation
598 effect in CLM4, has evolved to CESM2 (with CLM5 land component) with near average land
599 carbon uptake among CMIP6 models. The transition of CLM from CLM4 to CLM5, and the
600 reduction in its nutrient constraints on photosynthesis and the parametric controls on
601 fertilization responses are discussed in Wieder et al. (2019) and Fisher et al. (2019), respectively.
602 The land carbon uptake in MIROC-ESM increased from the lowest among CMIP5 models (149
603 PgC) to 701 PgC for MIROC-ES2L, among CMIP6 models, due to a new terrestrial biogeochemical



604 component (Ito and Inatomi, 2012). Although the CO₂ fertilization effect in this new land model
605 is weaker likely due to the incorporation of the nitrogen cycle, the model yields relatively higher
606 NPP (Hajima et al., 2019a), due to a higher CUE_{Δ} (as confirmed later in section 4.4.1). The land
607 carbon uptake in the IPSL-CM5A-LR model decreased from being the second largest in CMIP5
608 models (741 PgC) to below average for the IPSL-CM6A-LR model (477 PgC) due to implementation
609 of terrestrial photosynthesis downregulation, as a function of CO₂ concentration, which leads to
610 a decrease in GPP across all latitudes, with the largest decrease in the tropics.

611 The ocean carbon uptake in the IPSL model decreased from being the largest among CMIP5
612 models at 670 PgC in IPSL-CM5A-LR to 579 PgC for IPSL-CM6A-LR, and this is attributed to a
613 greater ocean stratification in the IPSL-CM6A-LR. The annual mean mixed layer depth is 46.7 m
614 and 40.2 m in IPSL-CM5A-LR and IPSL-CM6A-LR, respectively. While NorESM1-ME was one of the
615 CMIP5 models with the largest ocean carbon uptake (667 PgC), NorESM2-LM has an ocean
616 carbon uptake (599 PgC) close to the CMIP6 model mean. This is a consequence of changes in
617 the simulated (shallower depth and weaker strength) Atlantic meridional overturning circulation
618 and reduced mixed layer biases particularly at high latitudes (less deep winter mixing). Due to
619 these modifications, the efficiency of carbon export below the mixed layer in NorESM2-LM is
620 considerably reduced compared to the NorESM1-ME. This, in turn, leads to less excess carbon
621 stored in the North Atlantic Deep Water (below 2000 m) as well as in the Antarctic Intermediate
622 Water. For the MPI ESM, the decrease in land carbon uptake from 825 PgC in MPI-ESM-LR for
623 CMIP5 to 586 PgC in MPI-ESM1.2-LR for CMIP6 is associated with implementation of nitrogen
624 cycle model (Goll et al., 2017) and a new soil carbon model YASSO (Goll et al., 2015). Compared
625 to its predecessor HadGEM2-ES, UKESM1 represents a prognostic treatment of terrestrial



626 nitrogen including its impact on carbon storage in vegetation biomass and soil organic matter.
627 Limitation on terrestrial productivity from available nitrogen is the main reason for reduced land
628 carbon storage in UKESM1-0-LL (408 PgC) compared to HadGEM2-ES (768 PgC).

629

630 Figure A1 in the appendix shows the version of Figure 5 but at the time of CO₂ doubling (at year
631 70). Interestingly, the ordering of the models according to their diagnosed cumulative emissions
632 at 2×CO₂ is different from that at 4×CO₂. As expected, however, the model mean fractional
633 emissions taken up by land and ocean at 2×CO₂ are higher than at 4×CO₂, because both land and
634 ocean carbon sinks relatively weaken as CO₂ continues to increase.

635

636 4.3. Feedback parameters

637 Figure 6, panels a and b, compares the carbon-concentration (β_L) and carbon-climate feedback
638 (γ_L) parameters over land from participating CMIP6 models. The plots show feedback parameters
639 from different models as coloured dots but also their mean ± 1 standard deviation as a box. The
640 feedback parameters are calculated using all of the four approaches that are summarized in Table
641 1 to illustrate their sensitivity to the approach used. In addition, models whose land component
642 includes a representation of the N cycle are identified by an additional circle around their
643 coloured dots. Figure 6 also shows the mean ± 1 standard deviation values separately for models
644 that do and do not include a representation of the land N cycle using the BGC-COU approach, in
645 an attempt to understand the reason for the diverse responses of the land models. Results from
646 CMIP5 models in the A13 study are shown in a similar format for comparison in panels c and d.



647

648 Three primary observations can be made from Figure 6. First and foremost, the spread in the
649 magnitude of carbon-concentration and carbon-climate feedback over land in CMIP6 models is
650 of similar magnitude to that of CMIP5 models. Second, the carbon-climate feedback (γ_L) is more
651 sensitive to the approach used (and hence the type of simulations used) to derive its value than
652 the carbon-concentration feedback (β_L). Third, in the model mean sense, the absolute strength
653 of the feedback parameters is weaker for models that include a representation of the N cycle, for
654 both CMIP5 and CMIP6 models. Both the carbon gain due to increase in atmospheric CO₂
655 concentration and the carbon loss due to increase in globally average temperature in models
656 with representation of land N cycle is much lower than models that do not include the N cycle.
657 This response is most likely explained by the N limitation of photosynthesis as CO₂ increases and
658 additional release of N from dead organic matter as warming increases which boosts productivity
659 thereby compensating for carbon lost due to increased respiratory losses, as also discussed in
660 A13. The values of the feedback parameters, however, overlap between models that do and do
661 not include a representation of the N cycle, given the wider spread in the feedback parameter
662 values among models that do not include a representation of land N cycle, compared to models
663 that do.

664

665 Figure 7, panels a and b, compare the carbon-concentration (β_O) and carbon-climate feedback
666 (γ_O) parameters over the ocean from participating CMIP6 models. As in Figure 6, the feedback
667 parameters are calculated using all of the four approaches that are summarized in Table 1 and



668 results from CMIP5 models are shown for comparison in panels c and d. For both CMIP5 and
669 CMIP6 models, the absolute spread in the magnitude of the feedback parameters across the
670 participating models is an order of magnitude smaller for the ocean C cycle component compared
671 to the land C cycle component, as was also seen in F06 and A13. Similar to the land, the calculated
672 values of the ocean carbon-climate feedback (γ_O) are more sensitive to the approach used (and
673 hence the type of simulations used) than the ocean carbon-concentration feedback (β_O). In
674 agreement with Schwinger et al. (2014), the absolute values of γ_O are 2-3 times larger when
675 calculated using the COU and BGC simulations, compared to cases when RAD simulation is used,
676 for reasons mentioned earlier. Figures 6 and 7 show also that while the strength of the carbon-
677 concentration feedback is similar over land and ocean, the strength of the carbon-climate
678 feedback parameter over ocean is much weaker than over land.

679

680 Section A2 in the appendix discusses how Figures 6 and 7 and corroborate existing studies for the
681 preferred use of the BGC and COU simulations for finding the feedback parameters. Figure 6 and
682 7 also show that the effect of assuming T^* (the temperature change in the BGC simulation) zero
683 is around 1% for the calculated value of the carbon-concentration feedback parameter ($\beta_X, X =$
684 L, O) and around 5% for the carbon-climate feedback parameter ($\gamma_X, X = L, O$). This small effect
685 of T^* on the calculated global values of the feedback parameter allows investigation of the
686 reasons for differences among model by using simplified forms of β_X and γ_X as presented in
687 equations (6) and (7).

688



689 For completeness, Table A1 in the appendix summarizes the values of feedback parameters for
690 both land and ocean from CMIP6 and CMIP5 models (corresponding to Figures 6 and 7) at $4\times\text{CO}_2$
691 but also at $2\times\text{CO}_2$. Table A1 also shows the value of parameter α , the linear transient climate
692 sensitivity to CO_2 , following F06 (their equation 6) which is calculated as

$$693 \quad T' = \alpha c' \quad (20)$$

694 at $4 \times \text{CO}_2$.

695

696 4.4. Reasons for differences among models

697 4.4.1 Land

698 Equations (8) and (9) in Section 2.1.1 are used to gain insight into reasons for differing responses
699 of land models. In the BGC-COU approach and assuming $T^*=0$ (equation 8), the carbon uptake in
700 the BGC simulation is used to calculate the carbon-concentration feedback parameter (β_L).
701 Figure 8 shows how this carbon uptake over land is separated into vegetation and soil+litter
702 components both in absolute (panel a) and fractional terms (panel b). The models are arranged
703 from lowest to highest in terms of their land carbon uptake in the BGC simulation. The
704 partitioning into vegetation and soil+litter components is not shown for the BCC-CSM2-MR
705 model because total land carbon uptake in this model exceeded the sum of changes in the
706 vegetation and soil+litter carbon pools by more than 10% likely because of incomplete
707 accounting of pool sizes. Figure 8b shows that models vary widely in terms of how the carbon
708 uptake over land is split into vegetation and soil+litter components. The model mean values



709 indicate that slightly more of the carbon sequestered is allocated to vegetation (55%) than to the
710 soil+litter pools (45%).

711

712 Figure 9 shows the individual components of equation (8) which contribute to terms
713 corresponding to changes in vegetation (ΔC_V) and soil+litter (ΔC_S) carbon pools. Panel (a) of
714 Figure 8 is repeated in Figure 9 for easy correspondence of individual terms with their models.
715 The model mean values of individual terms do not take into account the results from the BCC-
716 CSM2-MR model. In essence, the terms in Figure 9 are emergent properties of the land models
717 of the individual ESMs and result from their multiple interacting processes. The comparison of
718 the individual terms of equation (8) provides additional insight into the reasons for differences in
719 land models. For example, the CNRM-ESM2-1 model has the highest land carbon uptake among
720 all models in the BGC simulation. However, this is not caused by a strong CO₂ fertilization effect
721 (the $\frac{\Delta GPP}{c'}$ term), but rather by the relatively high $\tau_{veg\Delta}$ and $\tau_{soil\Delta}$ values. The CO₂ fertilization
722 effect is strongest for the three models that simulate vegetation cover dynamically ($\frac{\Delta GPP}{c'} =$
723 0.141, 0.128, and 0.117 PgC yr⁻¹ ppm⁻¹ for NOAA-GFDL-ESM4, MPI-ESM1.2-LR, and UKESM1-0-
724 LL, respectively) since the $\frac{\Delta GPP}{c'}$ term also implicitly includes the effect of increasing vegetation
725 cover as CO₂ increases. The tree cover in the NOAA-GFDL-ESM4 model, for example, increases in
726 the BGC simulation – particularly in dry, high-latitude regions above 50° N (not shown). However,
727 these models do not simulate the largest land carbon uptake because of their lower than average
728 $\tau_{veg\Delta}$ and $\tau_{soil\Delta}$ values. The $\frac{\Delta GPP}{c'}$ term is unable to capture the CO₂ fertilization effect separately



729 from increasing vegetation cover and this illustrates the challenge in comparing models that do
730 and do not simulate vegetation cover dynamically. The CanESM5 model exhibits higher than
731 average land carbon uptake despite its near average strength of the CO₂ fertilization effect, and
732 $\tau_{veg\Delta}$ and $\tau_{soil\Delta}$ values. However, its CUE_{Δ} is the highest and therefore a much larger fraction of
733 GPP is converted to NPP. Although CUE_{Δ} is not the same as CUE , we found that CUE_{Δ} and CUE
734 (calculated at the end of the 1pctCO₂ simulation at 4xCO₂) are strongly correlated with a
735 correlation of around 0.90 (not shown). Similarly, $\tau_{veg\Delta}$ is strongly correlated, with a correlation
736 of 0.96, to $\tau_{veg} = C_V/NPP$ calculated at the end of the simulation. The ACCESS-ESM1.5 model
737 exhibits the lowest land carbon uptake because of its weak CO₂ fertilization effect and the lowest
738 CUE_{Δ} of all models. Finally, the $\frac{\Delta R_h}{\Delta LF}$ term shows the least variability across models, which is
739 reflective of the fact that the magnitude of the heterotrophic respiration flux is dominated by
740 NPP inputs into the dead carbon pools (Koven et al., 2015). Several of these individual terms are
741 strongly correlated. The $\frac{\Delta GPP}{c'}$ and $\frac{\Delta LF}{c'}$ terms have a correlation of 0.77, and $CUE_{\Delta} \frac{\Delta GPP}{c'}$ and
742 $\frac{\Delta LF}{c'}$ have a correlation of 0.94, since a stronger CO₂ fertilization effect also implies a larger litter
743 fall flux per unit CO₂. Surprisingly, CUE_{Δ} and τ_{veg} are negatively correlated (correlation = -0.49)
744 across models indicating that models which retain a higher fraction of GPP as NPP typically get
745 rid of vegetation carbon sooner via litter fall as indicated by a faster turnover of vegetation (lower
746 τ_{veg}), there by partially compensating for higher CUE_{Δ} .

747



748 While Figure 9 investigates reasons for differences among models that lead to different values of
749 their carbon-concentration feedback over land (β_L), Figure 10 investigates the reasons for varying
750 magnitudes of the carbon-climate feedback over land (γ_L). In equation (9), γ_L is a function of
751 change in land carbon (divided into vegetation and soil+litter components) in the COU relative to
752 the BGC simulation and the temperature change in the COU simulation (T'). Over land, the higher
753 temperatures in the COU relative to the BGC simulation affect both autotrophic and
754 heterotrophic respiratory fluxes, from live and dead vegetation pools, respectively, but also gross
755 photosynthesis rates. The primary effect of this temperature change in COU versus the BGC
756 simulation is the loss of carbon from the soil+litter carbon pool (hence the negative sign of γ_L for
757 most models, Figure 6b and 6d) but changes in the vegetation carbon pool also occur. Although
758 γ_L also depends on T' , Figure 10 arranges models in order from largest to smallest loss of land
759 carbon in COU relative to the BGC simulation to illustrate the varying response of the models.
760 This ordering of models changes slightly if the carbon loss (or gain in the CanESM5 model) is
761 divided by the temperature change T' in the COU simulation (yielding the value of γ_L which
762 assumes $T^*=0$ as in equation 9).

763

764 As shown in Figure 10, all models lose carbon from the soil+litter carbon pool but with widely
765 varying magnitudes. Although typically smaller than the change in soil+litter carbon pool, the
766 change in the vegetation carbon pool in the COU relative to the BGC simulation is not of the same
767 sign across models. Six of the eleven participating models lose carbon in the vegetation pool in
768 the COU relative to the BGC simulation thereby contributing to increasing the absolute
769 magnitude of γ_L , while the remaining five exhibit an increase in the vegetation carbon pool



770 thereby decreasing the absolute magnitude of γ_L . The largest increase in the vegetation carbon
771 pool is seen in the CanESM5 model that more than compensates for the carbon loss from the
772 soil+litter carbon pool yielding a positive value of γ_L in contrast to other models. This is one of
773 the few times a positive value of γ_L is seen in an Earth system model. Preliminary analysis of
774 CanESM5 data shows the increase in vegetation carbon, in the COU relative to the BGC
775 simulation, is caused by the increase in GPP and the resulting vegetation growth at mid-to-high
776 latitudes in response to warming temperatures and increasing CO₂. Interestingly, this doesn't
777 happen at 2×CO₂ (see Table A1 in the Appendix). At 2×CO₂ γ_L is still negative for CanESM5.

778

779 The loss in land carbon in the COU relative to the BGC simulation (except the CanESM5 model
780 that gains carbon), indicated by the orange bar in Figure 10, is strongly correlated with the carbon
781 gain in the BGC simulation (Figure 4e) (correlation is 0.59 for all models and 0.87 when CanESM5
782 is excluded) but not with the absolute amount of total land carbon. Figure A2 in the appendix
783 shows the absolute amount of carbon in soil+litter and vegetation pools, and their change from
784 the beginning, for the BGC simulation. The models vary widely in terms of the absolute size of
785 the carbon pools, especially for the soil+litter pool. There are two implications of models losing
786 more carbon in the COU relative to BGC simulation when they take up more carbon in the BGC
787 simulation alone. First, the transient behaviour of a model is determined primarily by its response
788 of CO₂ and temperature perturbations and not by the absolute amount of land carbon. Second,
789 that carbon-concentration (β_X) and carbon-climate (γ_X) feedback parameters must be correlated
790 as well. Indeed, this is the case over land for both CMIP5 and CMIP6 models, but also true for
791 ocean feedbacks although the correlations are somewhat weaker over the ocean. These



792 correlations are shown in Table 3 and are negative since higher positive values of β_x are
793 correlated with higher negative values of γ_x indicating that models that take up more carbon
794 with increasing CO₂ also release more carbon when they “see” the associated higher
795 temperatures.

796

797 4.4.2 Ocean

798 The time-integrated air-sea flux of carbon provides the dominant contribution to the increase in
799 the global ocean carbon through changes in the DIC inventory. However, the global ocean carbon
800 inventory is also affected by the land to ocean carbon flux from river runoff, and the carbon burial
801 in ocean sediments (see Table A2 in the appendix).

802

803 Ocean carbon cycle feedbacks are defined in terms of ocean carbon inventory changes for the
804 COU simulation, and the differences in COU relative to the BGC simulation. To fully understand
805 the ocean carbon-cycle feedbacks, it is necessary to understand the ocean carbon distributions
806 for the preindustrial and then analyze the carbon anomalies relative to the preindustrial for these
807 climate model experiments.

808

809 4.4.2.1 Ocean carbon distribution



810 The ocean dissolved inorganic carbon distribution, DIC, is controlled by a combination of physical,
811 chemical and biological processes. For the preindustrial period, there is less DIC in warmer waters
812 of the upper ocean and more DIC in colder mid-depth and bottom waters (Figure 11a, 12a);
813 illustrated here for UKESM1-0-LL as a representative example and Figs S1 to S7 show similar
814 distributions for all the diagnosed Earth system models. The vertical extent of the low DIC follows
815 the undulations of the thermocline, which is defined by strong vertical temperature and density
816 gradients, and is deeper over the subtropical gyres at 30°N and 30°S, and shallower in the
817 equatorial zone and at high latitudes. The greater DIC at depth is a consequence of greater
818 solubility in colder waters and the accumulation of DIC from the regeneration of organic matter.

819

820 To gain insight into how the ocean carbon distribution is controlled, the DIC is separated into
821 three pools, DIC_{sat} , $DIC_{disequib}$, and $DIC_{regenerated}$, as defined earlier. The DIC distribution for both
822 the preindustrial period and after 140 years in the 1pctCO₂ simulation reveal the following key
823 features for each of these carbon pools (Figures 11a,b and 12a,b):

- 824 • The saturated carbon pool provides the dominant contribution to the DIC, holding more than
825 $2.15 \text{ mol C m}^{-3}$, particularly within cooler waters below the thermocline;
- 826 • The regenerated carbon pool enhances the carbon stored below the surface waters, typically
827 providing an additional 0.2 mol C m^{-3} within the Southern Ocean and older waters spreading
828 from the Southern Ocean into the Atlantic and below the thermocline in the Pacific;
- 829 • The disequilibrium carbon is small close to the surface, representing waters close to an
830 equilibrium with the atmosphere. There is sometimes a positive disequilibrium of up to 0.05



831 mol C m⁻³ in some surface waters, which is associated with upwelling transferring carbon-rich
832 deeper waters to the surface. The disequilibrium carbon is more strongly negative below the
833 thermocline, typically reaching -0.1 mol C m⁻³ in the Atlantic and -0.02 mol C m⁻³ in the
834 Southern Ocean and Pacific. In the preindustrial, the undersaturation in carbon below the
835 thermocline is due to the subduction of cold waters at high latitudes that have not
836 equilibrated fully with the atmosphere, which then spread by advection along density
837 surfaces. In the model integrations reaching year 140, the carbon below the thermocline
838 become further undersaturated relative to the contemporary atmosphere due to the rapid
839 rise in [CO₂].

840

841 Next we consider the anomalies in the DIC at year 140 in the COU configurations of the 1pctCO₂
842 simulation calculated relative to the preindustrial period. The carbon anomaly, ΔDIC , in the
843 COU configuration is positive over the upper thermocline over the Atlantic and Pacific basins,
844 reaching +0.3 mol C m⁻³, coinciding with regions that are well ventilated. This gain in carbon is
845 made up of an increase in the saturated carbon over all depths due to higher atmospheric CO₂.
846 There is a dipole in the disequilibrium anomaly (Figures 11b,c and 12 b,c), generally weakly
847 positive in the upper ocean and more strongly negative in deeper waters below the thermocline
848 reaching up to -0.2 mol C m⁻³. This negative disequilibrium anomaly in deeper waters is smallest
849 in the relatively well-ventilated mid-depth waters of the North Atlantic, but extends over nearly
850 all of the more poorly ventilated mid-depth waters of the Pacific (Figures 11b and 12b).

851



852 The regenerated carbon anomaly is relatively small in magnitude reaching less than 0.05 mol C
853 m⁻³ and varies regionally, enhanced within much of the North Atlantic and the thermocline of the
854 Pacific, but with little change in the deep waters of the Pacific (Figures 11b and 12b). The increase
855 in regenerated carbon is due to a weakening of ocean overturning leading to an increase in
856 residence time and an associated accumulation of DIC from the regeneration of biologically-
857 cycled carbon (Bernardello et al., 2014; Schwinger et al., 2014). The regenerated carbon signal
858 does not change in the mid depths and deep Pacific as 140 years is too short an integration
859 timescale for any effect to be detected.

860

861 To diagnose the carbon-cycle feedback parameters, the ocean carbon response needs to be
862 considered for the BGC configuration where there is no additional warming from the increase in
863 atmospheric CO₂ and limited change in climate and ocean circulation. The resulting DIC
864 anomalies are generally very similar to those for the COU configuration (Figures 11b,c and 12b,c),
865 which is to be expected as the dominant effect for the ocean carbon response is the enhanced
866 ocean uptake of carbon in response to the increase in [CO₂]. There is a weakening in ventilation
867 in the COU configuration due to the additional radiative forcing. In comparison, in the BGC
868 configuration, there is no change in the circulation as there is no radiative warming effect, so that
869 there is slightly more carbon uptake in the northern North Atlantic, such as revealed at around
870 50°N, compared with the COU configuration. For the BGC configuration, the saturated carbon
871 pool is slightly greater at depth due to the water masses being cooler than in the COU
872 configuration, the disequilibrium anomaly shows a less negative anomaly in the northern North



873 Atlantic because there is little or no change in ventilation, and there are only slight differences in
874 the regenerated pool.

875

876 The climate response to rising [CO₂] is now considered in terms of the difference in the COU and
877 BGC configurations, which includes the combined effects of warming and circulation changes
878 (Figures 11d and 12d). The surface warming drives a decrease in solubility, an increase in
879 stratification and a reduction in ventilation, which leads to an overall decrease in carbon uptake
880 over the Southern Ocean and Pacific basins, and much of the Atlantic basin. There is a decrease
881 in the saturated carbon pool associated with the warming acting to inhibit carbon uptake. The
882 regenerated carbon anomaly is enhanced in the deep northern North Atlantic and in the
883 Southern Ocean. The regenerated carbon anomaly for this climate response is very similar to that
884 for the COU configuration, suggesting that the regenerated carbon anomaly is mainly due to
885 circulation changes: the gain in regenerated carbon anomaly is consistent with the expected
886 longer residence time from a weaker overturning and ventilation. There is a more negative
887 disequilibrium anomaly in the deep waters of the North Atlantic, which is a consequence of
888 weaker ventilation.

889

890 To gain more insight into the disequilibrium response, the ocean DIC response is also considered
891 for the radiatively-coupled integration (RAD), where there is no increase in [CO₂]. The additional
892 warming leads to a weakening in the overturning, which enhances the residence time in the
893 surface waters and so generally decreases the magnitude of the disequilibrium anomaly in the



894 North Atlantic (Figure S8), making the disequilibrium less negative relative to the preindustrial
895 and so forming a positive disequilibrium anomaly at year 140. In comparison the COU-BGC
896 captures the effect of the warming under rising [CO₂] leading to the disequilibrium anomaly
897 instead becoming more negative at depth, since the weakening in the ventilation leads to more
898 of the anthropogenic carbon remaining at the surface rather than being transferred into the
899 deeper ocean (Schwinger et al., 2014).

900

901 4.4.2.2 Changes in ocean carbon pools for diagnosing feedback parameters

902 The ocean carbon-concentration feedback parameter, β_O , is diagnosed from the changes in the
903 ocean carbon inventories for the BGC configuration, which does not include radiative warming
904 due to increasing [CO₂] (equation 13). There is a consistent increase in ocean carbon storage
905 across all models with a model mean value of around 670 PgC (Figure 13, light blue bars). This
906 increase in ocean carbon storage is made up of an increase in the saturated carbon inventory,
907 ΔC_{sat} , by about 3100 PgC from the increase in [CO₂] (Figure 13, red bars). This increase is partly
908 offset by a more negative disequilibrium carbon, $\Delta C_{disequilib}$, of typically -2500 PgC (Figure 13,
909 dark blue bars), representing how the ocean carbon uptake cannot keep up with the rate of [CO₂]
910 increase. There is relatively little change in the regenerated carbon inventory, $\Delta C_{regenerated}$. The
911 resulting β_O is positive and mainly explained by the chemical response involving the rise in ocean
912 saturation with no significant biological changes, although the physical uptake of carbon within
913 the ocean is unable to keep pace with the rise in [CO₂].

914



915 The ocean carbon-climate feedback parameter, γ_o , is diagnosed from the difference between
916 the COU model configuration and the BGC configuration, and so includes the effect of an
917 increasing surface warming under rising $[\text{CO}_2]$ (equation 14). There is a broadly consistent
918 response across models, with a model mean decrease in carbon inventory of around 80 PgC due
919 to the additional warming in the COU configuration relative to the BGC configuration (Figure 14,
920 light blue bars). The effect of this additional warming and the associated climate change leads to
921 a decrease in both the saturated carbon and disequilibrium carbon of typically -60 and -70 PgC
922 (Figure 14, orange and dark blue bars), representing the decrease in solubility and decreased
923 ocean ventilation. There is an increase in the regenerated carbon of typically 50 PgC (Figure 14,
924 green bars), which is due to a weaker circulation leading to a longer residence time of
925 thermocline and deep waters, so that there is more time for the accumulation of regenerated
926 carbon below the mixed layer. The resulting γ_o is negative, indicating that the ocean takes up
927 less carbon in response to the combination of surface warming and a weakening in ocean
928 ventilation. This response involves a combination of chemical, physical and biological changes
929 where the warming reduces the solubility of the carbon in the ocean and a weakening in the
930 circulation decreases the disequilibrium pool, but lengthens the residence time and so increases
931 the regenerated pool.

932

933 Overall, the ocean carbon inventory increases in the BGC configuration by 666 ± 53 PgC (model
934 mean \pm ensemble standard deviation), and decreases in COU relative to BGC by -80 ± 15 PgC. The
935 resulting β_o is very similar across all the models (0.78 ± 0.06 PgC ppm⁻¹), reflecting the strong
936 control of carbonate chemistry by rising atmospheric CO_2 (Katavouta et al., 2018). The dominant



937 contributions are composed of a positive contribution from the saturated carbon (3.66 ± 0.16 PgC
938 ppm^{-1}) and a negative contribution from the disequilibrium carbon (-2.98 ± 0.16 PgC ppm^{-1}) (see
939 Table A3 in the Appendix); these inter-model differences are relatively small with ratios of the
940 standard deviation to model mean of only 0.05 and 0.06 respectively. The regenerated
941 contribution is over two orders of magnitude smaller than the sum of the saturated and
942 disequilibrium contributions, and so may be neglected for evaluating β_0 .

943

944 The values of γ_0 differ more strongly across the models (-16.95 ± 5.62 PgC $^{\circ}\text{C}^{-1}$) and arise from
945 differences in the extent of the surface warming and the dynamical changes in the ocean
946 circulation and resulting changes in ventilation, residence time and biological regeneration (Table
947 A3). The contributions to γ_0 include negative contributions from the saturated (-12.78 ± 2.50 PgC
948 $^{\circ}\text{C}^{-1}$) and disequilibrium (-16.36 ± 5.31 PgC $^{\circ}\text{C}^{-1}$) components, which are partly opposed by a
949 positive contribution from the regenerated component (12.25 ± 8.53 PgC $^{\circ}\text{C}^{-1}$). The largest
950 intermodel differences are in the regenerated and disequilibrium responses and a relatively small
951 spread in the saturated response, with the ratios of the standard deviation to the model mean
952 are 0.70, 0.33 and 0.20 respectively (Table A3).

953

954 4.5. Transient climate response (TCR) and transient climate response to cumulative
955 emissions (TCRE)

956



957 Other than the feedbacks associated with the coupled carbon cycle and climate system, the
958 idealized 1pctCO2 simulation is also used for calculating two other climate metrics routinely. The
959 first is the transient climate response (TCR) which is defined as the temperature change, relative
960 to the preindustrial state, at the time of CO₂ doubling ($\Delta T_{2\times CO_2}$), that occurs at 70 years after the
961 start of the simulation. The second is the transient climate response to cumulative emissions
962 (TCRE) which is defined as ratio of TCR to diagnosed cumulative fossil fuel emissions also at the
963 time of CO₂ doubling ($\tilde{E}_{2\times CO_2}$) (Matthews et al., 2009) typically expressed in units of °C/EgC (1
964 EgC = 1000 PgC).

$$965 \quad TCRE = \frac{\Delta T_{2\times CO_2}}{\tilde{E}_{2\times CO_2}} \quad (21)$$

966 It has been shown that TCRE is approximately constant over a wide range of cumulative emissions
967 and emission pathways (e.g. see review by MacDougall, 2016). Therefore, although non-CO₂
968 GHGs and other climate forcings (e.g. aerosols and land use change) also affect the realized
969 warming, TCRE is a considered to be a straightforward measure of peak warming caused by
970 anthropogenic CO₂ emissions.

971

972 We do not discuss here TCR and TCRE in detail since the focus of our study is on carbon feedbacks.
973 However, both these quantities are readily calculated using results presented in this study. Table
974 A4 in the appendix lists TCR, $\tilde{E}_{2\times CO_2}$, and TCRE from the eleven CMIP6 models considered in this
975 study. The mean \pm standard deviation range for TCR, $\tilde{E}_{2\times CO_2}$, and TCRE from the eleven CMIP6
976 models considered here are 1.99 ± 0.44 °C, 1121 ± 73 PgC, and 1.78 ± 0.41 °C EgC⁻¹, respectively.



977 For fifteen CMIP5 models, Gillett et al. (2013) calculated the mean \pm standard deviation range for
978 TCRE to be $1.63 \pm 0.48 \text{ }^\circ\text{C EgC}^{-1}$ and a 5%-95% range for its observationally constrained value as
979 $0.7\text{-}2.0 \text{ }^\circ\text{C EgC}^{-1}$. The TCRE metric has gained significant policy relevance (Frame et al., 2014;
980 Millar et al., 2016) and it is used to calculate the remaining allowable carbon emissions to reach
981 a specified temperature change target above the preindustrial level (Millar et al., 2017; Rogelj et
982 al., 2019).

983

984 The uncertainties in TCRE stem from uncertainties both in TCR and $\tilde{E}_{2\times\text{CO}_2}$ which is directly
985 affected by land and ocean carbon uptake. A large fraction of uncertainty in $\tilde{E}_{2\times\text{CO}_2}$ comes from
986 the diverse response of land carbon cycle models and the results presented here indicate that
987 representation of the nitrogen cycle is helpful in reducing this uncertainty, as indicated by the
988 spread across land models. For the results reported here from eleven CMIP6 models, however,
989 the uncertainty in TCR (mean \pm standard deviation = $1.99 \pm 0.44 \text{ }^\circ\text{C}$) is much greater than the
990 uncertainty in $\tilde{E}_{2\times\text{CO}_2}$ ($1121 \pm 73 \text{ PgC}$) so that TCR contributes about 90% of the total uncertainty
991 in the calculated TCRE value ($1.78 \pm 0.41 \text{ }^\circ\text{C EgC}^{-1}$) (see section A6 in the Appendix).

992

993 The TCRE may also be expressed in terms of a product of a thermal contribution from the
994 dependence of surface warming on radiative forcing and a carbon contribution from the
995 dependence of radiative forcing on cumulative carbon emissions (Williams et al., 2016; Katavouta
996 et al., 2018), as



997
$$TCRE = \frac{\Delta T_{2 \times CO_2}}{\Delta R_{2 \times CO_2}} \frac{\Delta R_{2 \times CO_2}}{\tilde{E}_{2 \times CO_2}} \quad (22)$$

998 where $\Delta R_{2 \times CO_2}$ is the change in radiative forcing relative to the preindustrial period. For a suite
999 of ten CMIP5 models, Williams et al. (2017) show that the inter-model spread in the TCRE
1000 calculated from the 1pctCO2 experiment, is again dominated by the inter-model differences in
1001 the thermal contribution, $\frac{\Delta T_{2 \times CO_2}}{\Delta R_{2 \times CO_2}}$, due to climate feedback and ocean heat uptake over the first
1002 few decades, but the inter-model differences in the carbon contribution, $\frac{\Delta R_{2 \times CO_2}}{\tilde{E}_{2 \times CO_2}}$, due to land and
1003 ocean carbon uptake become of comparable importance after 80 years.

1004

1005 Although a large fraction of uncertainty in TCRE is contributed by physical climate system
1006 processes that determine TCR and not the biogeochemical processes that determine $\tilde{E}_{2 \times CO_2}$,
1007 reducing the uncertainty in land and ocean carbon uptake across models will still contribute to
1008 reducing the uncertainty in the estimates of TCRE on centennial timescales.

1009

1010 5. Summary and conclusions

1011 Model intercomparison projects offer several benefits including calculation of model mean
1012 response, quantification of the uncertainty based on the spread across models, and how this
1013 uncertainty changes over time that allows modellers to evaluate how their model's response is
1014 different from others'. The carbon feedbacks analysis presented here based on the C⁴MIP



1015 protocol of experiments (Jones et al., 2016) allows to investigate how feedback strengths have
1016 evolved since CMIP5 and also attempts to understand the reasons behind the spread in models.
1017

1018 The carbon uptake over land and ocean, in response to increasing atmospheric CO₂
1019 concentration, is well known to be dominated by the positive contribution from the carbon-
1020 concentration feedback (Arora et al., 2013a; Gregory et al., 2009). The strength of this feedback
1021 is of comparable magnitudes over land (mean ± standard deviation = 0.97±0.40 PgC ppm⁻¹) and
1022 ocean (0.79±0.07 PgC ppm⁻¹) although the feedback is much more uncertain over land as
1023 indicated by the standard deviation across the eleven models considered here. This dominant
1024 positive contribution from the carbon-concentration feedback is, however, opposed by the
1025 weaker negative carbon-climate feedback that is associated with the climate change that results
1026 due to increasing atmospheric CO₂. The absolute magnitude of this weaker negative feedback is
1027 about three times larger, but an order of magnitude more uncertain, over land (-45.1±50.6 PgC
1028 °C⁻¹) than over ocean (-17.2±5.0 PgC °C⁻¹). Model estimates of the ocean carbon-concentration
1029 feedback are very consistent with each other, reflecting the strong control of how carbonate
1030 chemistry alters with rising atmospheric CO₂. There is a relatively wider range in the model
1031 estimates of the ocean carbon-climate feedback, particularly in terms of how changes in ocean
1032 circulation alter the disequilibrium and regeneration terms. Over land, however, since the
1033 carbon-concentration and carbon-climate feedbacks are determined entirely by biological
1034 process, which are much less understood, the resulting uncertainty is much higher across land
1035 models than across the ocean models. This uncertainty in the strength of carbon-concentration
1036 and carbon-climate feedbacks over land is well known (Arora et al., 2013b; Friedlingstein et al.,



1037 2006). The inclusion of N cycle results in lower absolute strength of the feedback parameters
1038 over land but also a reduced spread across the land models. While the uncertainty in TCRE is
1039 dominated by physical processes affecting the thermal response involving climate feedbacks and
1040 heat uptake on decadal timescales, a reduction in the uncertainty in land and ocean carbon
1041 uptake across models will reduce the uncertainty in the TCRE on centennial timescales.

1042

1043 The additional analyses that we have performed to gain further insight into the reasons for
1044 differences among models provide insight into their diverse response, especially for land models.
1045 Over land, the diverse response of models is found to be primarily due to the wide range of the
1046 strength of the CO₂ fertilization effect, the fraction of GPP that is converted to NPP, and the
1047 residence times of carbon in the live (vegetation) and dead (litter plus soil) carbon pools across
1048 models. There is more consistency in the response of the ocean models, although inter-model
1049 differences arise from differences in the ventilation and residence time altering the ocean
1050 disequilibrium and regenerated carbon.

1051

1052 Finally, the decision to use fully- and biogeochemically coupled configurations of the 1pctCO₂
1053 experiment as the standard simulations to diagnose carbon cycle and climate system feedbacks
1054 from should provide consistency and continuity for future versions of Earth system models to be
1055 compared against their predecessors.

1056



1057 **Table 1:** The values of the carbon-concentration (β) and carbon-climate (γ) feedback parameters
 1058 can be solved using results from any two combinations of the RAD, BGC and COU versions of an
 1059 experiment as shown in equation (1). In addition, when using results from the BGC and COU
 1060 simulations the effect of temperature change in the BGC simulation (T^*) can be neglected, as was
 1061 done in the F06 study, yielding approximate values for β_X and γ_X .
 1062
 1063
 1064

Approach	γ_X	β_X
The RAD-BGC approach	$\gamma_X = \frac{\Delta C_X^+}{T^+}$	$\beta_X = \frac{\Delta C_X^*}{c'} - \frac{\gamma_X T^*}{c'}$
The RAD-COU approach	$\gamma_X = \frac{\Delta C_X^+}{T^+}$	$\beta_X = \frac{\Delta C_X'}{c'} - \frac{\gamma_X T'}{c'}$
The BGC-COU approach	$\gamma_X = \frac{\Delta C_X' - \Delta C_X^*}{T' - T^*}$	$\beta_X = \frac{1}{c'} \left(\frac{\Delta C_X^* T' - \Delta C_X' T^*}{T' - T^*} \right)$
The BGC-COU approach with $T^* = 0$	$\gamma_X = \frac{\Delta C_X' - \Delta C_X^*}{T'}$	$\beta_X = \frac{\Delta C_X^*}{c'}$

1065

1066

1067

1068



1069

Modelling group	CSIRO	BCC	CCCma	CESM	CNRM	GFDL
ESM	ACCESS-ESM1.5	BCC-CSM2-MR	CanESM5	CESM2	CNRM-ESM2-1	GFDL-ESM4
Atmosphere resolution	1.875°x1.25°, L38	1.125°x1.125°, L46	2.81° x2.81°, L49	0.9°x1.25°	T127 (1.4°x1.4°) L91	Cube-sphere C96 (1-1072 degree)
Ocean resolution	1° but finer between 10S-10N and in the Southern Ocean, L50	1° but becoming finer to 1/3° within 30°N - 30°S, L40	1° but becoming finer to 1/3° within 20°N - 20°S, L45.	gx1v7 displaced pole grid (384 x 320 lat x lon)	1°but becoming 0.3° in the Tropics, L75	0.5 degree tri-polar grid
Land carbon/biogeochemistry component						
Model name	CABLE2.4 with CASA-CNP	BCC-AVIM2	CLASS-CTEM	CLM5	ISBA-CTRIP	LM4p1
Number of live carbon pools	3	3	3	22	6	6 1076
Number of dead carbon pools	6	8	2	7	7	4
Number of plant functional types (PFTs)	13	16	9	22	16	6 1078
Fire	No	No	No	Yes	yes	Yes
Dynamic vegetation cover	No	No	No	No	no	Yes 1080
Nitrogen cycle	Yes (and phosphorus)	No	No	Yes	No (implicit, derived from Yin 2002)	No
Ocean carbon/biogeochemistry component						
Model name	WOMBAT	MOM4_L40, Ocean carbon cycle follows OCMIP2	CMOC (biology), carbonate chemistry follows OMIP protocol.	MARBL	PISCESv2-gas	COBALTv2
Number of phytoplankton types	1	0	1	3	2	2 1085
Number of zooplankton types	1	0	1	1	2	3
Explicit nutrients considered	Phosphorus, Iron	Phosphorus	Nitrogen	Nitrogen, Phosphorus, Silica, Iron	Nitrogen, Phosphorus, Silica, Iron	Nitrogen, Phosphorus, Silica, Iron 1088

1089

1090

1091

1092

1093

1094

1095



1096

1097

1098

1099

1100

1101

1102

1103

1104

1105

1106

1107

1108

1109

1110

1111 **Table 2:** Primary features of the physical atmosphere and ocean components, and land and ocean
 1112 carbon cycle components of the eleven participating models in this study.

1113

1114

Modelling group	IPSL	JAMSETC (Team MIROC)	MPI	NCC	UK
ESM	IPSL-CM6A-LR	MIROC-ES2L	MPI-ESM1.2-LR	NorESM2-LM	UKESM1-0-LL
Atmosphere resolution	2.5°x.3°, L79	2.81x2.81, L40	T63, 1.8°x1.8°. L47	1.9°x2.5°, L32	1.875° x1.25°, L85
Ocean resolution	1°-0.3° in the Tropics L75	Almost 1° but becoming finer to North pole and equator (Tripolar system: 360x256), L62	GR1.5 (1.5°, finer close to Antarctica and Greenland), L40	1° with enhanced meridional resolution near the Equator, L53	1°
Land carbon/biogeochemistry component					
Model name	ORCHIDEE, branch 2.0	MATSIRO (physics) VISIT-e (BGC)	JSBACH3.2	CLM5	JULES-ES-1.0
Number of live carbon pools	8	3	3	22	3
Number of dead carbon pools	3	6	18	7	4
Number of plant functional types (PFTs)	15	13	13	22	13
Fire	No	No	Yes	Yes	No
Dynamic vegetation cover	No	No	Yes	No	Yes
Nitrogen cycle	No	Yes	Yes	Yes	Yes
Ocean carbon/biogeochemistry component					
Model name	PISCES-v2	OECO2	HAMOCC6	Modified HAMOCC5.1	MEDUSA-2.1
Number of phytoplankton types	2	2 (non-diazotroph and diazotroph)	2	1	2
Number of zooplankton types	2	1	1	1	2
Explicit nutrients considered	Nitrogen, Phosphorus, Silica, Iron	Nitrogen, Phosphorus, Iron	Nitrogen, Phosphorus, Silica, Iron	Nitrogen, Phosphorus, Silica, Iron	Nitrogen, Silica, Iron



1115

1116 **Table 3:** Correlation between carbon-concentration (β_X) and carbon-climate (γ_X) feedback
1117 parameters over land and ocean across comprehensive ESMs from the CMIP5 intercomparison
1118 in the A13 study and CMIP6 intercomparison in this study. For land correlation is also shown
1119 when CanESM5 is excluded from CMIP6 models.

1120

Land	Ocean	
-0.69	-0.64	CMIP6 (11 models)
-0.92 (excluding CanESM5)		
-0.82	-0.75	CMIP5 (8 models)

1121

1122

1123

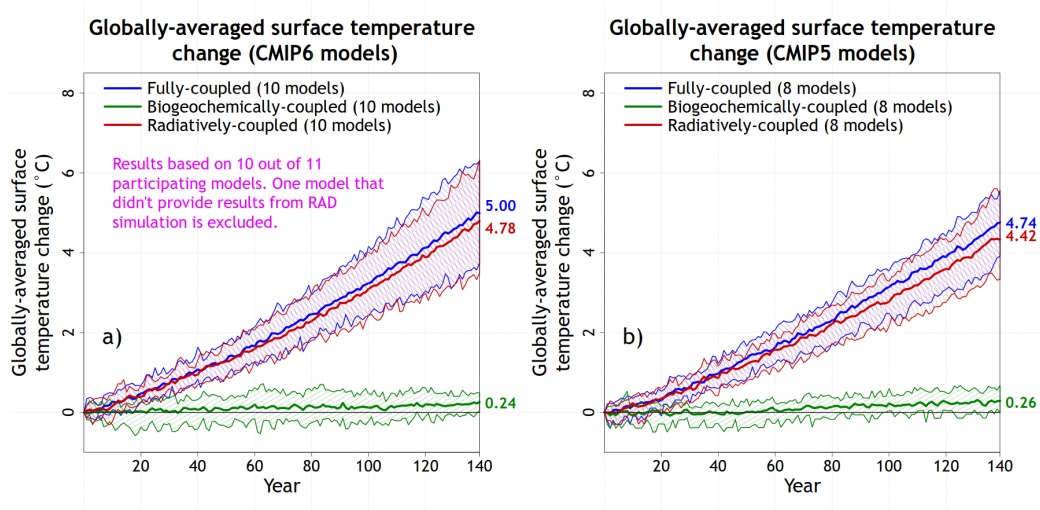
1124

1125



1126

1127

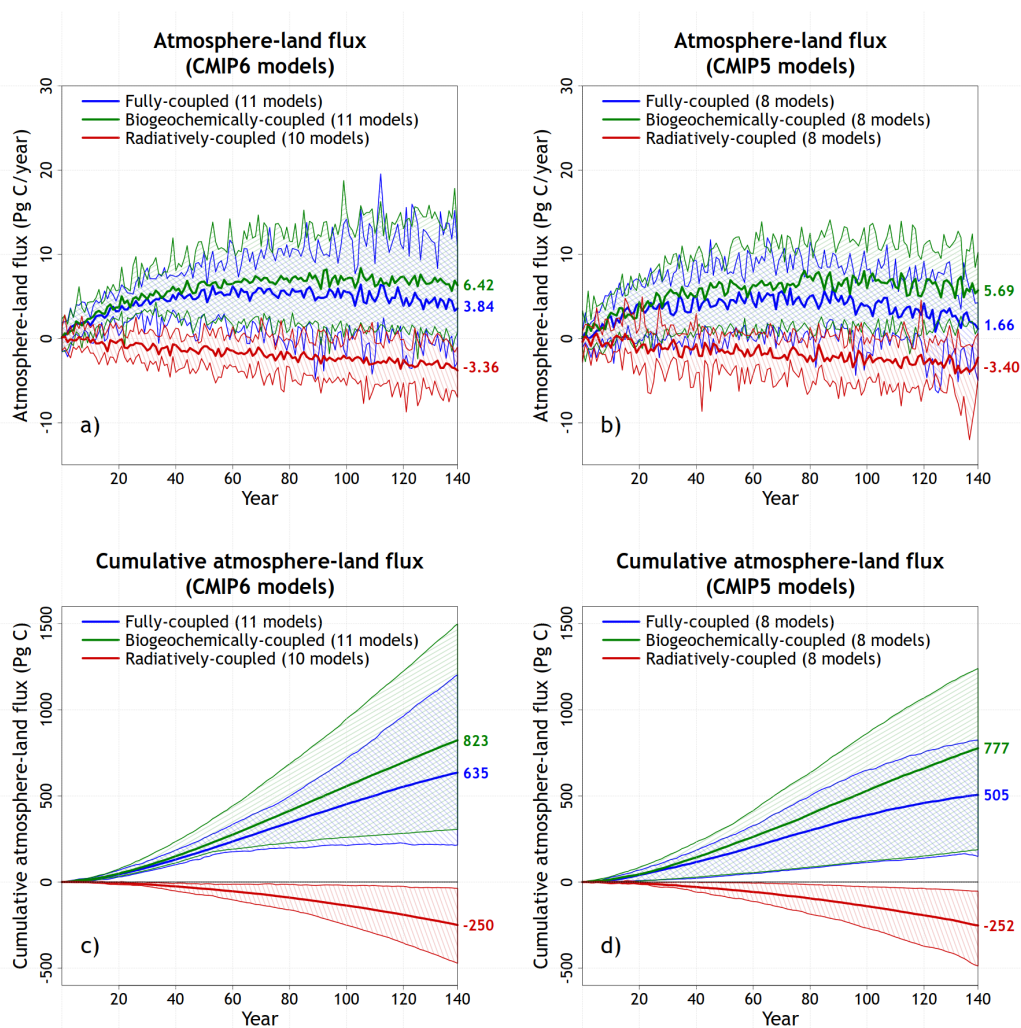


1128

1129 Figure 1: Temperature changes in the fully-, biogeochemically- and radiatively-coupled
1130 configurations of the 1pctCO₂ experiment across participating CMIP6 (panel a) and CMIP5 (panel
1131 b) comprehensive ESMs that participated in this and the Arora et al. (2013) study, respectively.
1132 Model mean is indicated by the solid lines and the range across the models is indicated by shading
1133 around the solid lines. Individual model results are shown in Figure 4.

1134

1135



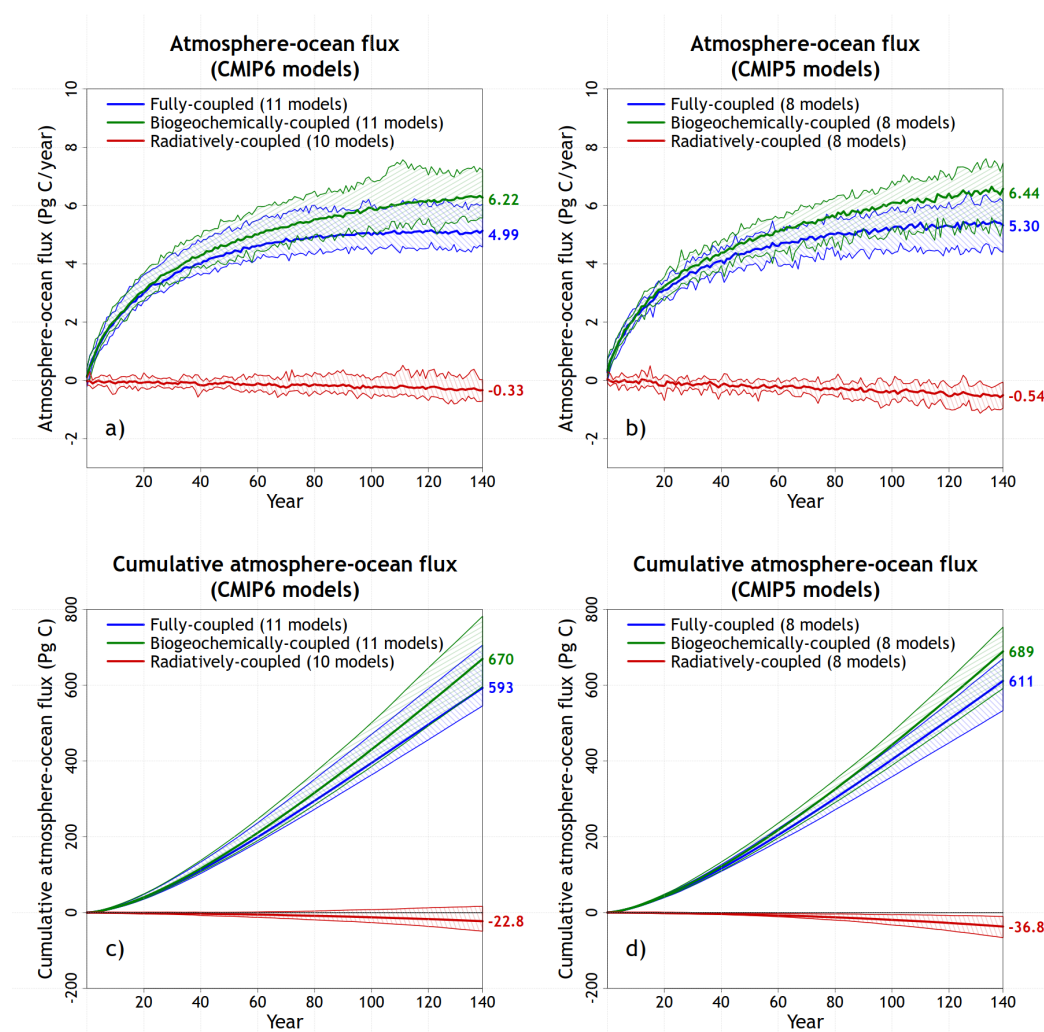
1136

1137 Figure 2: Model mean values and the range across models for annual simulated atmosphere-land
 1138 CO₂ flux (top row) and their cumulative values (bottom row) for participating CMIP6 (left column)
 1139 and CMIP5 (right column) models from the fully-, biogeochemically- and radiatively-coupled
 1140 versions of the 1pctCO₂ experiment. Individual model results are shown in Figure 4.

1141



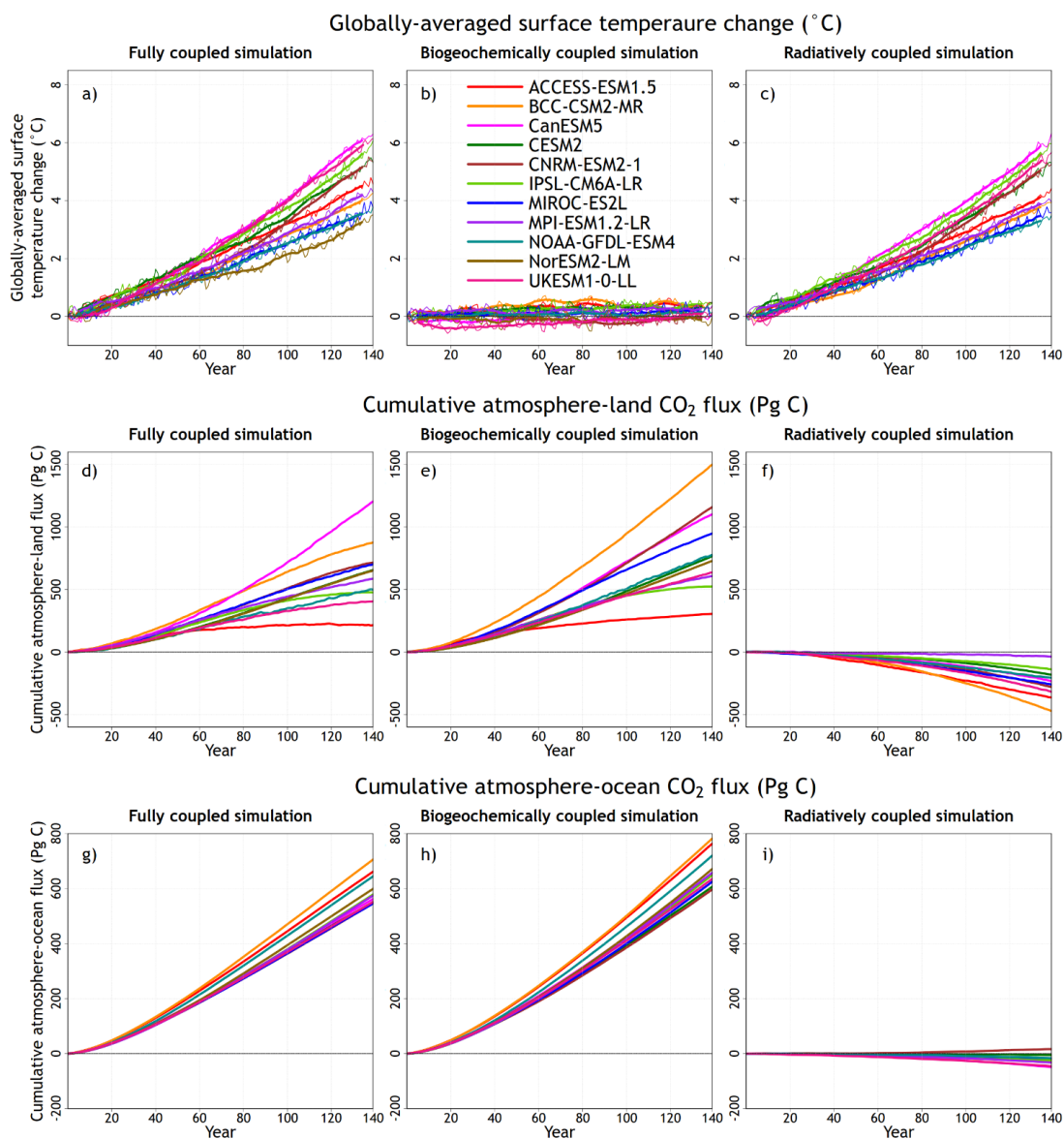
1142



1143

1144 Figure 3: Model mean values and the range across models for annual simulated atmosphere-
 1145 ocean CO₂ flux (top row) and their cumulative values (bottom row) for participating CMIP6 (left
 1146 column) and CMIP5 (right column) models from the fully-, biogeochemically- and radiatively-
 1147 coupled versions of the 1pctCO₂ experiment. Individual model results are shown in Figure 4.

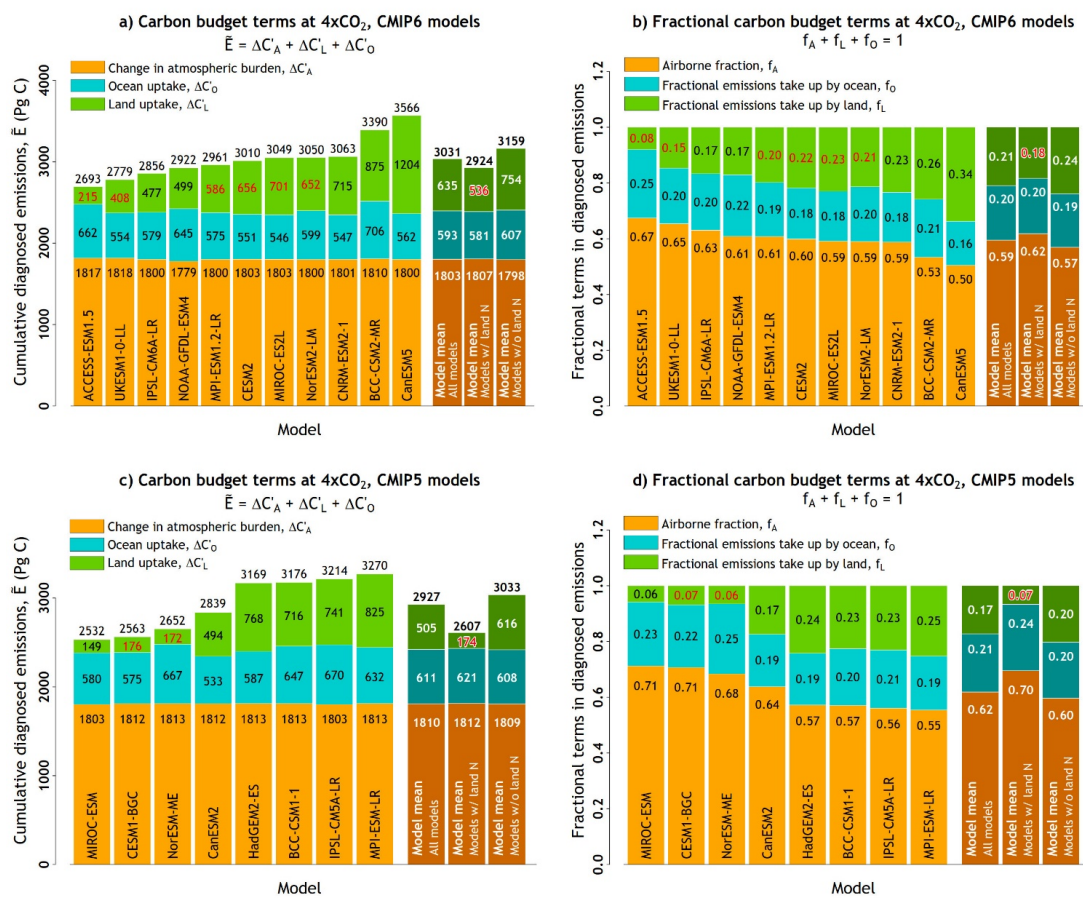
1148



1149 Figure 4: Individual model values from CMIP6 models for globally-averaged surface temperature
1150 change (top row), cumulative atmosphere-land CO_2 flux (middle row), and cumulative
1151 atmosphere-ocean CO_2 flux (bottom row) from the fully-, biogeochemically- and radiatively-
1152 coupled versions of the 1pct CO_2 experiment. Results from the radiatively-coupled configuration
1153 were not available from NorESM2-LM models at the time of writing.



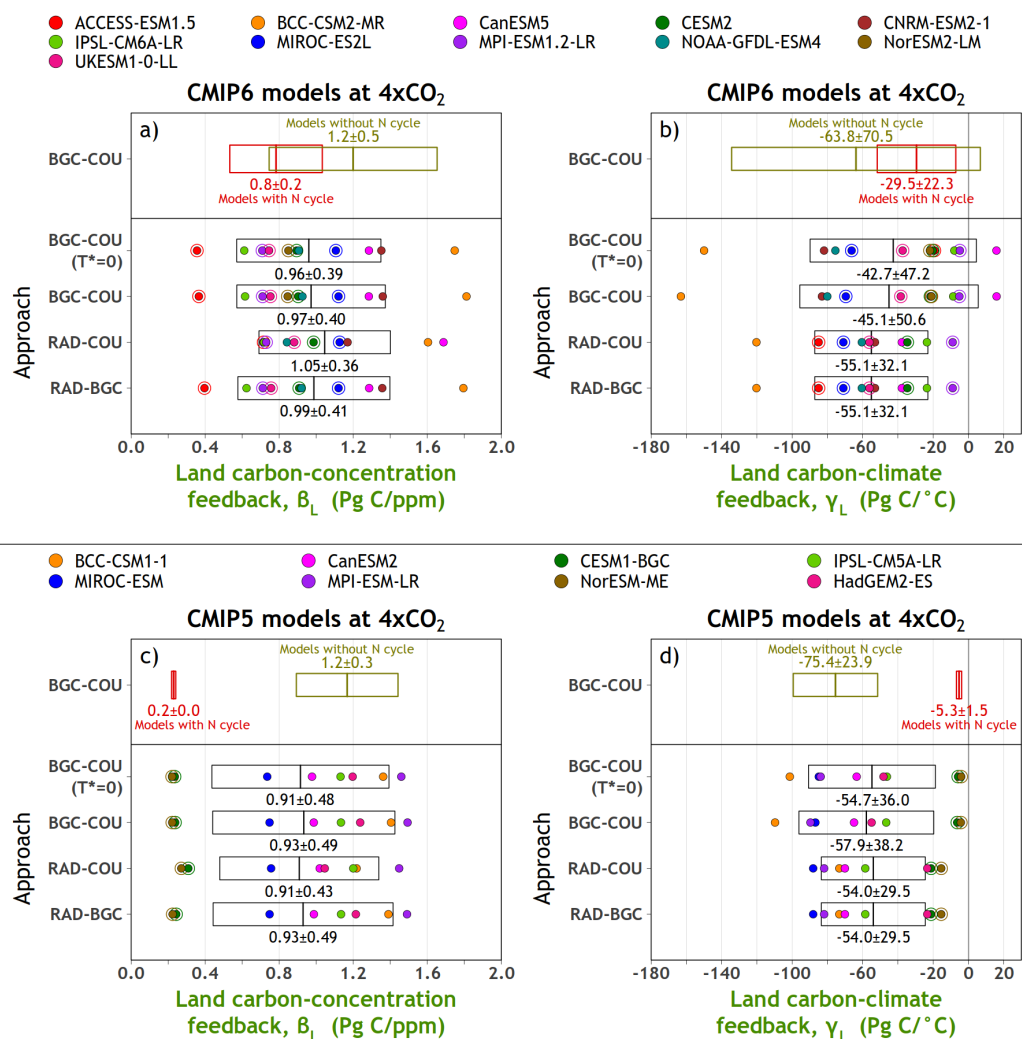
1154



1155 Figure 5: Components of the carbon budget terms in cumulative emissions from the eleven
 1156 participating CMIP6 models based on equation (15) in panel (a) and equation (16) in panel (b)
 1157 using results from the fully-coupled 1pctCO₂ simulation. The models are arranged in an
 1158 ascending order based on their cumulative emissions values. Results from participating CMIP5
 1159 models in the A13 study are shown in panels c and d. In addition, ESMs whose land component
 1160 includes a representation of N cycle are identified by red font colour for cumulative land carbon
 1161 uptake (panels a and c) and fractional emissions taken up by land (panels b and d). Model mean
 1162 is shown for all models but also separately for models whose land components include or do not
 1163 include a representation of the N cycle.

1164

1165

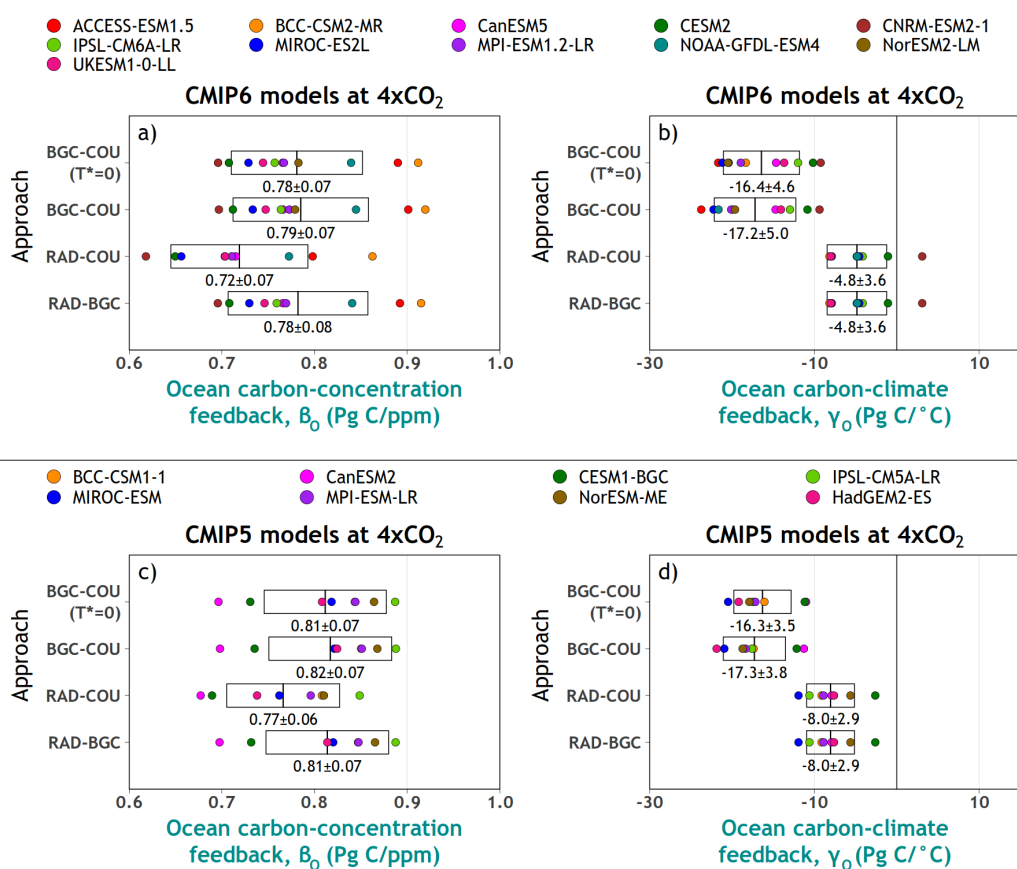


1166

1167 Figure 6: Carbon-concentration (panel a) and carbon-climate (panel b) feedback parameters
 1168 over land from participating CMIP6 models calculated using the approaches summarized in
 1169 Table 1. The boxes show the mean \pm 1 standard deviation range and the individual coloured
 1170 dots represent individual models. Models which include a representation of land nitrogen cycle
 1171 are identified with a circle around their dot. Model-mean \pm 1 standard deviation range of
 1172 feedback parameters is also separately shown for models which do and do not represent land
 1173 land nitrogen cycle using the BGC-COU approach. Results from participating CMIP5 models in the
 1174 A13 study are shown in panels c and d. Note that among CMIP6 models results from NorESM2-
 1175 LM were not available for the RAD simulation at the time of writing.

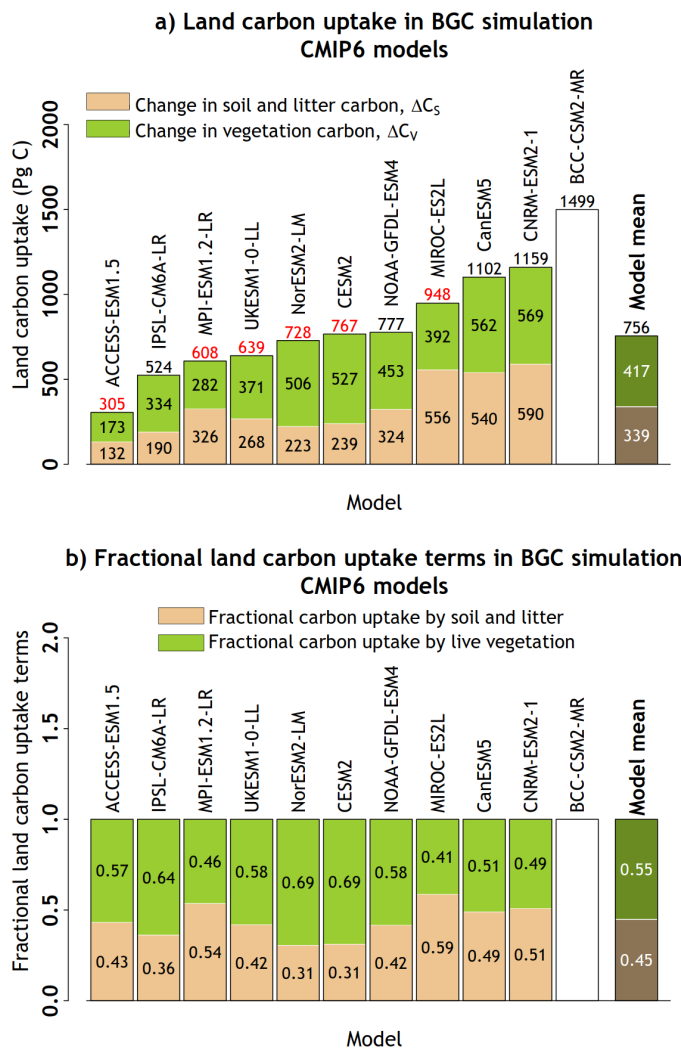


1176



1177

1178 Figure 7: Carbon-concentration (panel a) and carbon-climate (panel b) feedback parameters
 1179 over ocean from participating CMIP6 models calculated using the approaches summarized in
 1180 Table 1. The boxes show the mean \pm 1 standard deviation range. Results from participating
 1181 CMIP5 models in the A13 study are shown in panels c and d. Note that among CMIP6 models
 1182 results from NorESM2-LM were not available for the RAD simulation at the time of writing.



1183

1184 Figure 8: Carbon uptake over land in the BGC simulation, used to calculate land carbon-
 1185 concentration feedback (β_L) and its partitioning into vegetation and soil+litter carbon pools
 1186 across the participating CMIP6 models (panel a). Panel (b) shows the fractional land carbon
 1187 uptake by vegetation and soil+litter carbon pools in the BGC simulation. No partitioning is
 1188 shown for the BCC-CSM2-MR model because total land carbon uptake in this model exceeded
 1189 the sum of changes in the vegetation and soil+litter carbon pools by more than 10%. Total land
 1190 carbon uptake in models which include a representation of the N cycle is shown in red color.
 1191 The results from the BCC-CSM2-MR model are not used in calculating the model-mean values.



1192

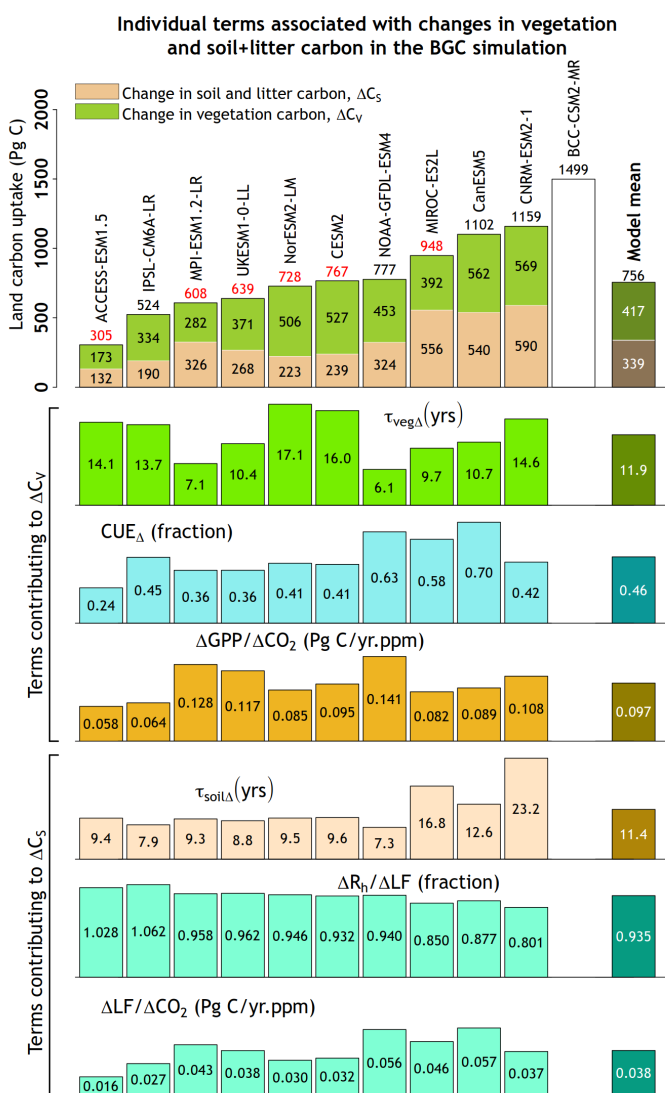


Figure 9: Individual terms of equation (8) which contribute to changes in vegetation (ΔC_V) and litter+soil (ΔC_S) carbon pools. Values from the BCC-CSM2-MR model are not used in calculating the model-mean.

1217

1218

1219

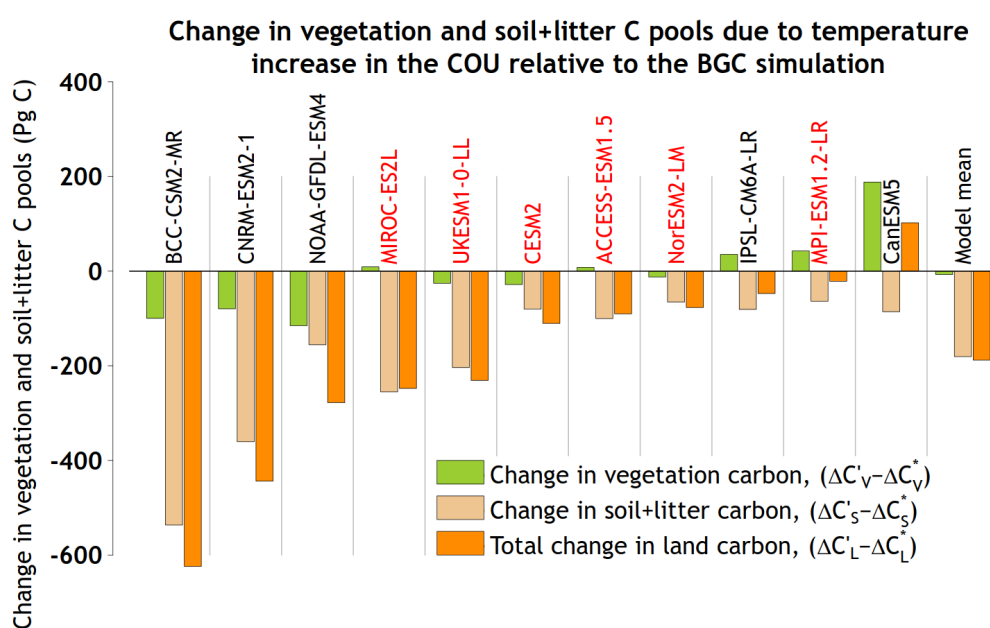
1220

1221



1222

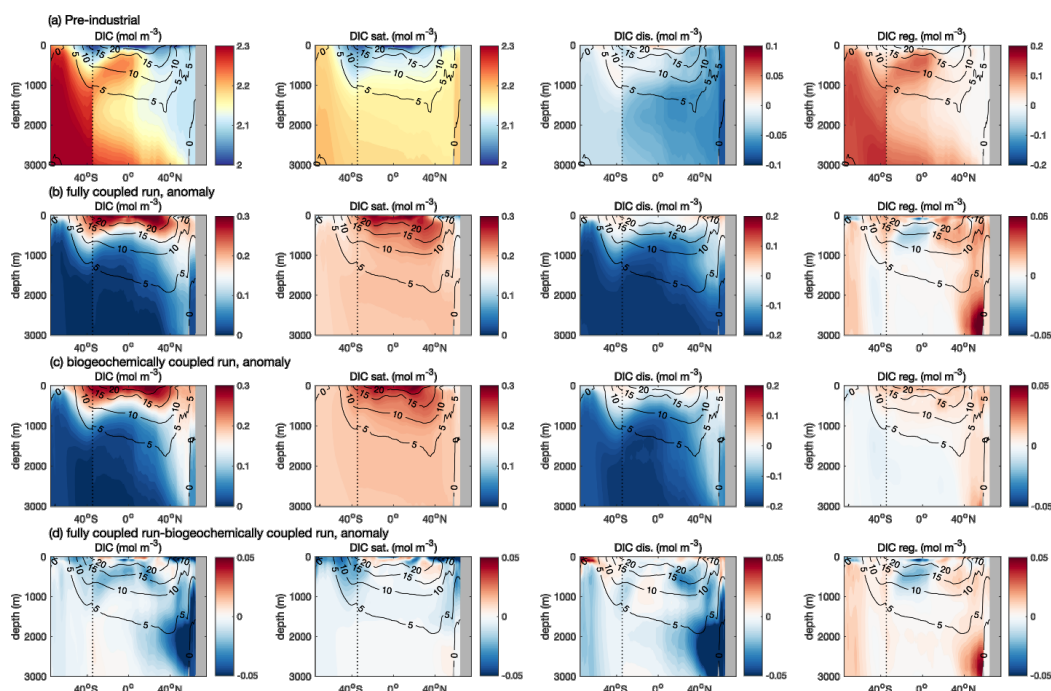
1223



1224

1225 Figure 10: The changes in vegetation and soil+litter carbon pools in the COU relative to the BGC
 1226 simulation, as shown in equation (9), which contribute to the calculation of carbon-climate
 1227 feedback over land (γ_L) in the BGC-COU approach.

1228



1229

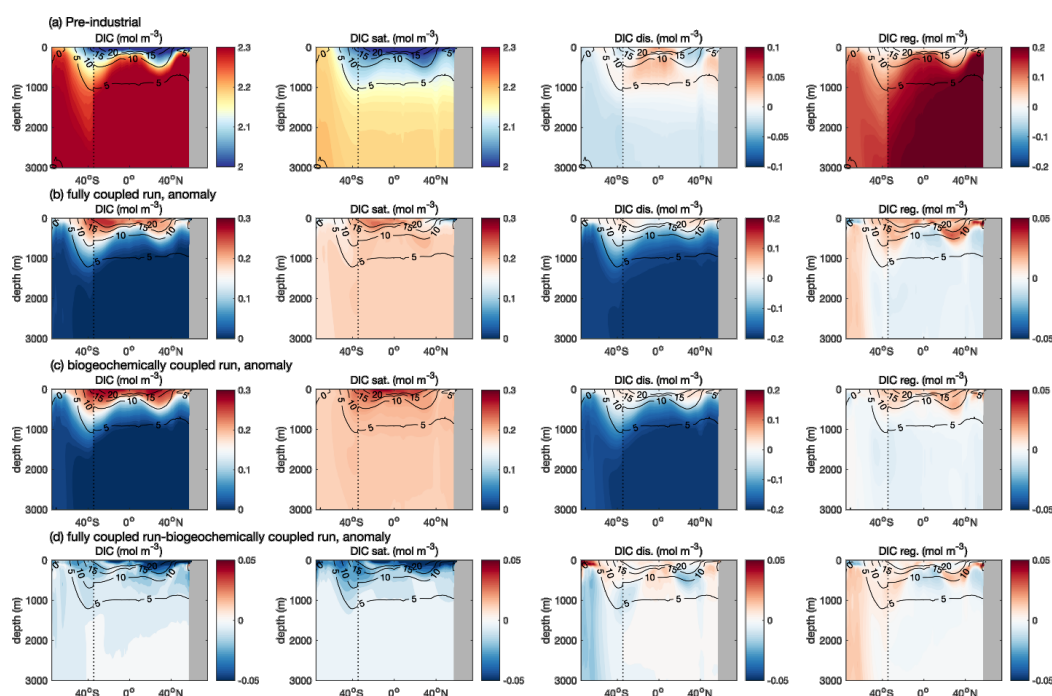
1230

1231 Figure 11. Meridional section of the dissolved inorganic carbon, DIC (mol m^{-3}), and constituent
 1232 carbon pools in UK-ESM1-0-LL for the zonally-averaged Atlantic and Southern Ocean: (a) the
 1233 preindustrial absolute concentrations, and the anomalies relative to the preindustrial state at
 1234 year 140 for (b) the COU configuration, (c) the BGC configuration and (d) the COU minus the
 1235 BGC configuration. The DIC is separated into saturated carbon, DIC_{sat} , the disequilibrium
 1236 carbon, $DIC_{disequib}$, and the regenerated carbon, $DIC_{regenerated}$. The Atlantic and Southern Ocean
 1237 domains are separated by a black vertical line.

1238



1239



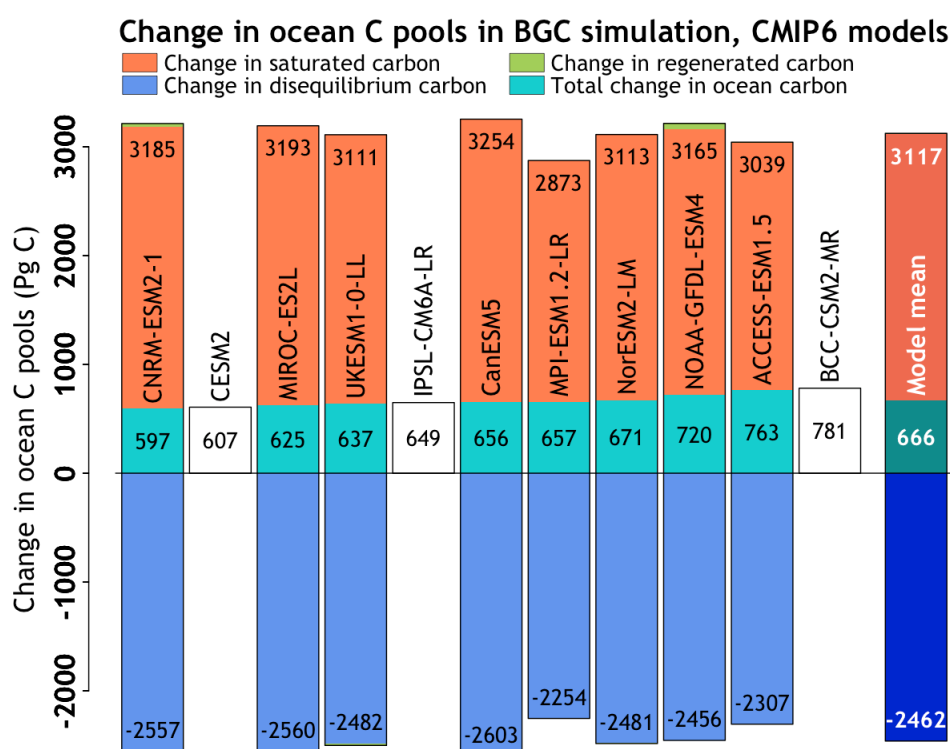
1240

1241 Figure 12. Meridional section of the dissolved inorganic carbon, DIC (mol m^{-3}), and constituent
1242 carbon pools in UK-ESM1-0-LL for the zonally-averaged Pacific and Southern Ocean: (a) the
1243 preindustrial absolute concentrations, and the anomalies relative to the preindustrial state at
1244 year 140 for (b) the COU configuration, (c) the BGC configuration and (d) the COU minus the
1245 BGC configuration. The DIC is separated into saturated carbon, DIC_{sat} , the disequilibrium
1246 carbon, $DIC_{disequib}$, and the regenerated carbon, $DIC_{regenerated}$. The Pacific and Southern Ocean
1247 domains are separated by a black vertical line.

1248



1249



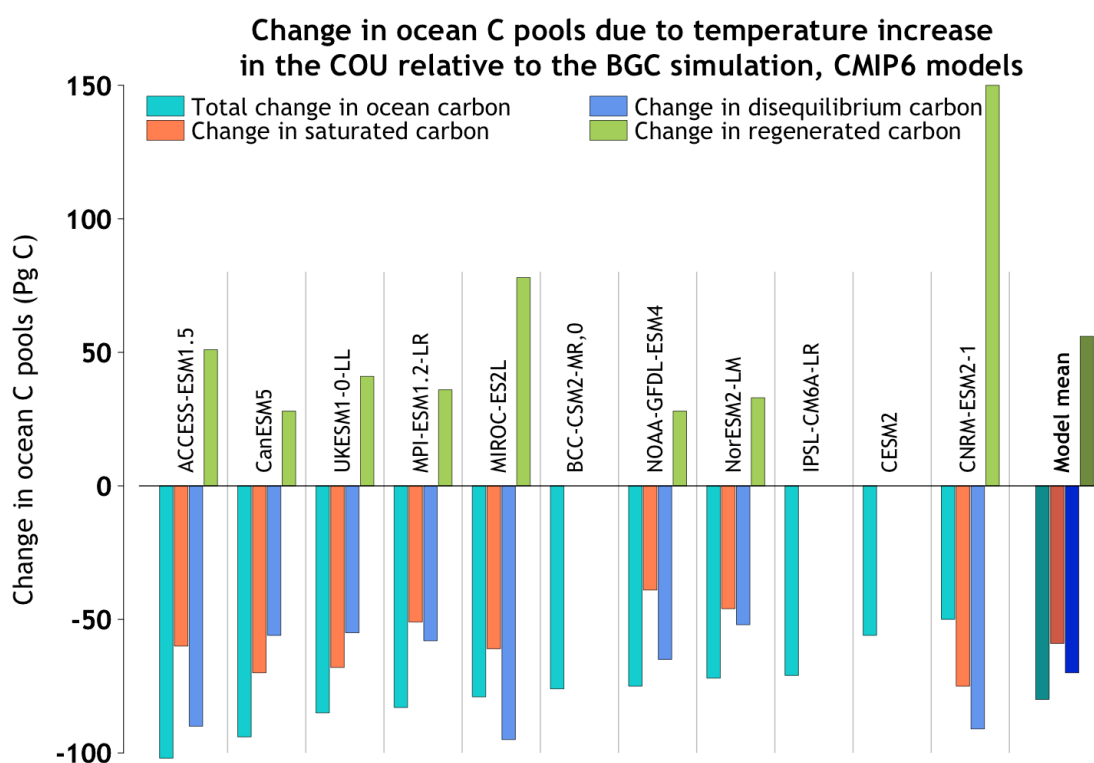
1250

1251 Figure 13. Carbon uptake over the ocean in the biogeochemically-coupled simulation, used to
 1252 calculate ocean carbon-concentration feedback and its partitioning into saturated, disequilibrium
 1253 and regenerated carbon pools across the participating CMIP6 models (left panels) using equation
 1254 (12). No partitioning is shown for models for which 3D ocean fields were not available and the
 1255 results of these models are not used in calculating the model mean values (right panel). The sum
 1256 of the partitions does not exactly match the total ocean uptake diagnosed from the air-sea fluxes
 1257 due to land-ocean interactions involving storage in sediments and river inputs.

1258



1259



1260

1261 Figure 14. Change in saturated, disequilibrium and regenerated carbon pools in the fully coupled
 1262 minus the biogeochemical simulation using equation (12), which contribute to the calculation of
 1263 carbon-concentration feedback over the ocean. The sum of the partitions does not exactly match
 1264 the total ocean uptake diagnosed from the air-sea fluxes due to land-ocean interactions involving
 1265 storage in sediments and river inputs.

1266



1267

1268 **Appendix**

1269

1270 **A1. The climate carbon cycle feedbacks framework**

1271

1272 The rate of change of carbon in the combined atmosphere-land-ocean system is written as

1273

1274
$$\frac{dC_G}{dt} = \frac{dC_A}{dt} + \frac{dC_L}{dt} + \frac{dC_O}{dt} = E \quad (\text{A1})$$

1275

1276 where the Global carbon pool $C_G = C_A + C_L + C_O$ is the sum of carbon in the Atmosphere, Land
1277 and Ocean components (PgC), and E is the rate of anthropogenic CO₂ emission (PgC/yr) into the
1278 atmosphere. The equations for the atmosphere, land and ocean are

1279
$$\begin{aligned} \frac{dC_A}{dt} &= F_A(T, c) + E \\ \frac{dC_L}{dt} &= F_L(T, c) \\ \frac{dC_O}{dt} &= F_O(T, c) \end{aligned} \quad (\text{A2})$$

1280 where $(F_L + F_O) = -F_A$ are the fluxes between the atmosphere and the underlying land and
1281 ocean, taken to be positive into the components. The fluxes F are expressed as functions of
1282 surface temperature T and the surface atmospheric CO₂ concentration c . Here and subsequently,
1283 uppercase C denotes carbon pools and lowercase c denotes atmospheric CO₂ concentration.



1284 In the fully-, biogeochemically-, and radiatively-coupled versions of the 1pctCO₂ experiments
1285 analyzed here, the rate of change of atmospheric carbon dC_A/dt is specified in equations (A1)
1286 and (A2). The uptake or release of CO₂ by the underlying land and ocean yields an effective
1287 emission E which serves to maintain the budget.

1288

1289 The changes in atmosphere carbon budgets, from the pre-industrial control simulation, in the
1290 differently coupled simulations are represented as

1291

1292 Radiatively-coupled
$$\frac{dC'_A}{dt} - E^+ = F_A^+ = -F_L^+ - F_O^+ = \Gamma_A T^+ \quad (\text{A3a})$$

1293 Biogeochemically-coupled
$$\frac{dC'_A}{dt} - E^* = F_A^* = -F_L^* - F_O^* = \Gamma_A T^* + B_A c' \quad (\text{A3b})$$

1294 Fully-coupled
$$\frac{dC'_A}{dt} - E = F'_A = -F'_L - F'_O = \Gamma_A T' + B_A c' \quad (\text{A3c})$$

1295

1296

1297 which serve to define the instantaneous carbon-concentration (B_A) and carbon-climate (Γ_A)
1298 feedback parameters and assume linearization of the globally integrated surface-atmosphere
1299 CO₂ flux in terms of global mean temperature and concentration change. In equation (A3), F^+ ,
1300 F^* , and F' are the flux changes and T^+ , T^* , and T' the temperature changes in the radiatively-,
1301 biogeochemically- and fully-coupled simulations, and E^+ , E^* , and E are the resulting implicit
1302 emissions. c' is the specified CO₂ concentration change above its pre-industrial level in the
1303 1pctCO₂ simulations. In the biogeochemically-coupled simulation there is no radiative forcing
1304 due to increasing CO₂ so T^* is small, although not zero and exhibits a distinct spatial pattern. The



1305 assumption made in equation (A3) is that the feedback parameters are the same in the three
1306 cases.

1307

1308 Carbon budget changes for the land component parallel (A3) but without the emissions terms as

1309 Radiatively-coupled $\frac{dC_L'}{dt} = F_L^+ = \Gamma_L T^+$ (A4a)

1310 Biogeochemically-coupled $\frac{dC_L^*}{dt} = F_L^* = \Gamma_L T^* + B_L c'$ (A4b)

1311 Fully-coupled $\frac{dC_L^*}{dt} = F_L' = \Gamma_L T' + B_L c'$ (A4c)

1312

1313 and similarly for the ocean component. Since $F_A = -(F_L + F_O)$ it follows that $\Gamma_A = -(\Gamma_L + \Gamma_O)$
1314 and $B_A = -(B_L + B_O)$. There are no terms involving c' in the radiatively-coupled simulation
1315 (equations 3a and 4a) since the pre-industrial value of atmospheric CO₂ concentration is
1316 prescribed for the biogeochemistry components so $c' = 0$ and does not affect the flux.

1317

1318 The instantaneous feedback parameters (B_L and Γ_L) differ from that in the integrated flux
1319 approach of Friedlingstein et al. (2006) who express time integrated flux changes (i.e. change in
1320 pool or reservoir sizes) as functions of temperature and CO₂ concentration changes with

1321 Radiatively-coupled $\int F_L^+ = \Delta C_L^+ = \gamma_L T^+$ (A5a)

1322 Biogeochemically-coupled $\int F_L^* = \Delta C_L^* = \gamma_L T^* + \beta_L c'$ (A5b)

1323 Fully-coupled $\int F_L' = \Delta C_L' = \gamma_L T' + \beta_L c'$ (A5c)

1324



1325 and similarly for the ocean component, with the assumption that the $\Delta C'_o$ term includes changes
1326 in the carbon amount of ocean sediment as well.

1327

1328 The units of instantaneous and integrated flux based parameters are different (Γ - PgC yr⁻¹ °C⁻¹,
1329 B - PgC yr⁻¹ ppm⁻¹ and γ - PgC °C⁻¹, β - PgC ppm⁻¹). Arora et al. (2013) show how the
1330 instantaneous and integrated flux based feedback parameters are related to each other

1331

1332 Integrating equations (A1) and (A2) from initial time to t gives

1333
$$\Delta C'_A + \Delta C'_L + \Delta C'_O = \int_0^t E dt = \tilde{E} \quad (A6)$$

1334 Where $\Delta C'_A = 2.12 (c(t) - c(0))$ is the change in atmospheric carbon burden (the factor 2.12
1335 converts atmospheric CO₂ concentration from ppm to atmospheric burden in PgC) and $\Delta C'_X =$
1336 $\int_0^t F'_X dt, X = L, O$ is the cumulative flux equal to the change in the land or ocean carbon pool
1337 for the fully-coupled simulation. The terms in equation (A6) indicate the contribution of changes
1338 in atmosphere, land and ocean carbon pools to cumulative emissions \tilde{E} . Finally, division by the
1339 cumulative emissions term in equations (A6) gives all the terms in a fractional form as

1340

1341
$$f_A + f_L + f_O = 1 \quad (A7)$$

1342



1343 where f_A is the airborne fraction of cumulative emissions and f_L and f_O are fractional emissions
1344 taken up by the land and ocean. These components are evaluated at the time of CO₂ quadrupling.

1345

1346 **A2. Justification for using BGC and COU simulations for finding feedback parameters**

1347 Figures 6 and 7 provide justification for using the BGC-COU approach, over the RAD-BGC and
1348 RAD-COU approaches, in calculating the feedback parameters as discussed below. In Figure 7,
1349 the absolute magnitude of γ_O when using the BGC-COU approach is about twice in CMIP5 models
1350 (and more than three times in CMIP6 models) compared to its model-mean value calculated using
1351 the RAD-BGC and RAD-COU approaches. The reason for this is that the RAD simulation misses the
1352 suppression (due to weakening of the ocean circulation) of carbon drawdown to the deep ocean.
1353 This is because there is no buildup of a strong carbon gradient from the atmosphere to the deep
1354 ocean in the RAD simulation. This process is important when climate change is forced by
1355 increasing atmospheric CO₂, and therefore feedback parameters calculated using the BGC-COU
1356 approach are more likely to include all processes relevant to application for realistic scenarios. In
1357 Figure 6, although the carbon-climate feedback parameter over land (γ_L) is larger in absolute
1358 amount, it is comparatively less sensitive to the approach used, than over ocean, because over
1359 land an increase in temperature not only increases the respiratory losses but also affects
1360 photosynthetic processes especially in conjunction with increasing CO₂. Warmer temperatures
1361 increase photosynthesis over mid to high latitude regions where photosynthesis is currently
1362 limited by temperature and more so with increasing CO₂, but decrease photosynthesis over
1363 tropical regions where the temperatures are already too warm for optimal photosynthesis. The



1364 net result of these compensating processes plays out very differently in different models and in
1365 the model-mean sense this results in less sensitivity of the calculated value of carbon climate
1366 feedback parameter over land (γ_L) to the different approaches than over ocean. This is seen in
1367 both CMIP5 and CMIP6 models. When γ_L is calculated using the RAD-BGC and RAD-COU
1368 approaches, it is exclusively calculated using results from the RAD simulation. However, since
1369 over land photosynthesis is also affected by temperature in addition to respiration (with widely
1370 varying responses between models) the γ_L values vary widely between models between the RAD-
1371 BGC/RAD-COU approach and the BGC-COU approach. This is seen, for example, for ACCESS-
1372 ESM1.5, IPSL, and CanESM5 models in Figure 6b. The very different values of γ_L for individual
1373 models, when using different approaches to calculate them, are the result of the differing
1374 responses of the vegetation and soil+litter carbon pools, in the RAD and COU simulations, and
1375 this is supported by results that were presented in Section 4.3.2.

1376

1377 In Figure 7 value of γ_O changes sign for the CNRM-ESM2-1 model from positive when calculated
1378 using the RAD-BGC or RAD-COU approaches to negative when calculated using the BGC-COU
1379 approach and this further illustrates the sensitivity of feedback parameters to the approach used
1380 to calculate them. This non-linear behaviour for a previous version of the CNRM model has been
1381 document in Schwinger et al. (2014) and caused by the large increase in regenerated DIC in the
1382 RAD simulation, similar to the increase in the COU relative to the BGC simulation, as shown in
1383 Figure 14 for the CNRM-ESM2-1 model. This non-linear behaviour is stronger in CNRM-ESM2-1,
1384 compared to CNRM-ESM1, its previous version (Séférián et al., 2016), most likely due to a new
1385 parameterization for N fixation which increases ocean NPP and a revised parameterization for



1386 organic matter remineralization in the model's ocean biogeochemistry component (PISCESv2-
1387 gas). A contribution to a positive γ_0 is also made by declining sea ice in the RAD simulation which
1388 leads to changes in the sign of the air-sea carbon exchange in the Southern Ocean. The vertical
1389 profile of dissolved inorganic carbon in the Southern Ocean in BGC and COU simulations (with
1390 rising $[\text{CO}_2]$) is different from that in the RAD simulation (for the preindustrial $[\text{CO}_2]$) and this
1391 leads to additional non-linearities.

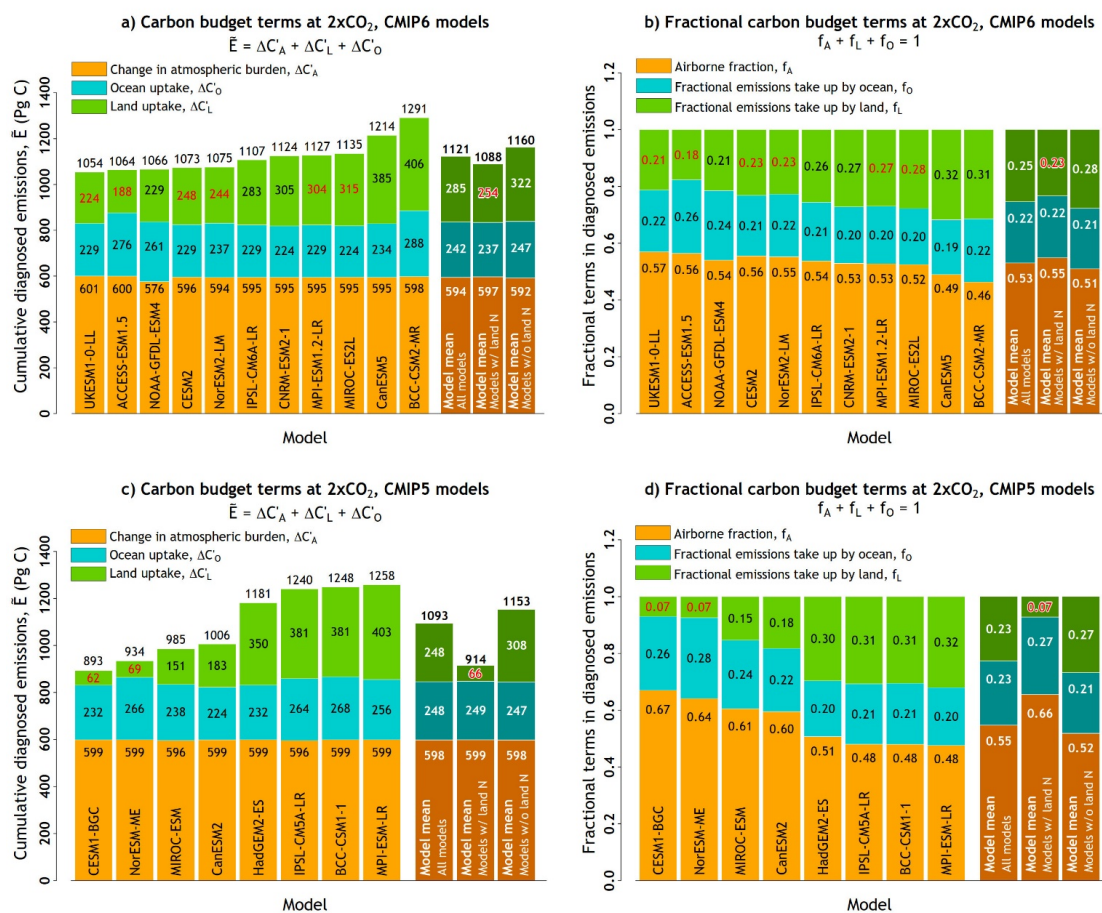
1392

1393



1394 **A3. Additional Figures**

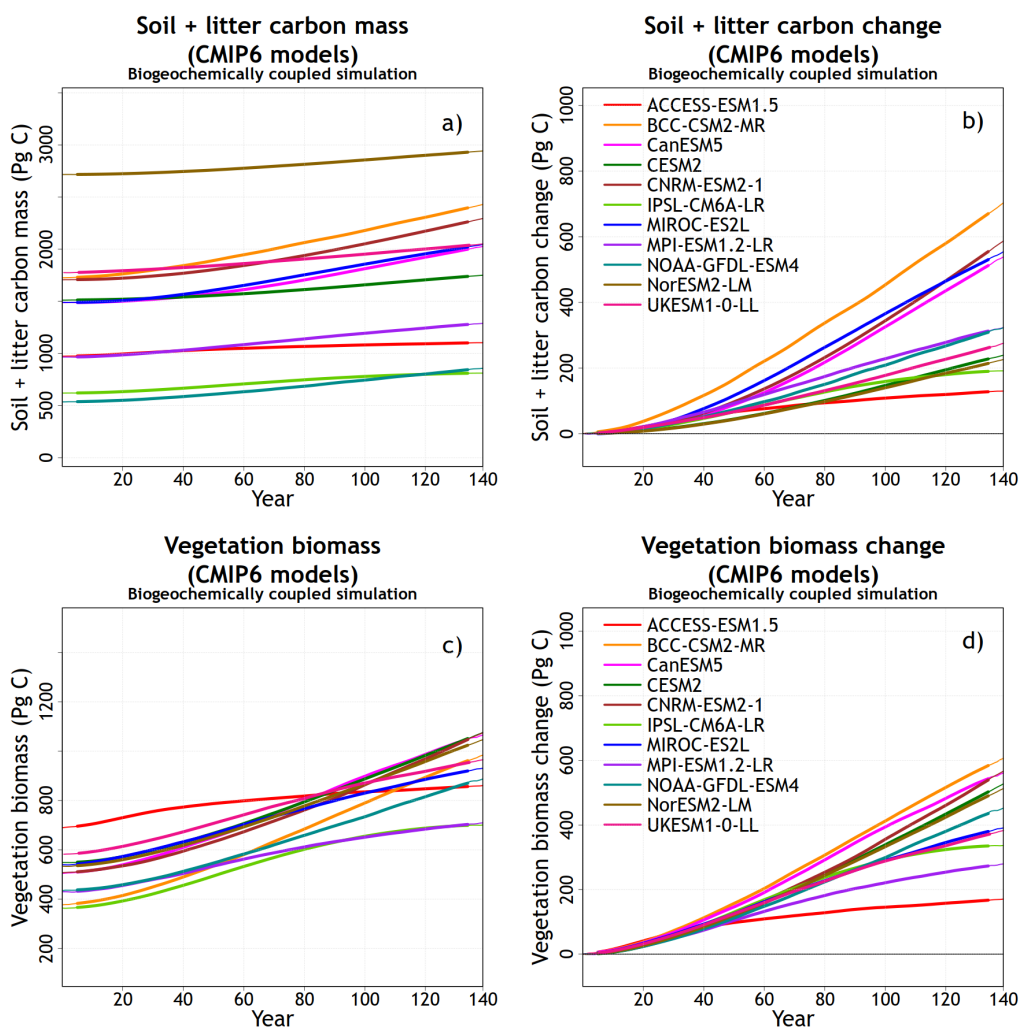
1395



1396 Figure A1: Components of the carbon budget terms in cumulative emissions from the eleven
 1397 participating CMIP6 models based on equation (15) in panel (a) and equation (16) in panel (b)
 1398 using results from the fully-coupled 1% per year increasing CO₂ simulation but at 2xCO₂ (year 70)
 1399 in contrast to Figure 5 which showed these results at 4xCO₂. The models are arranged in an
 1400 ascending order based on their cumulative emissions values. Results from participating CMIP5
 1401 models in the A13 study are shown in panels c and d. In addition, ESMs whose land component
 1402 includes a representation of N cycle are identified by red font colour for cumulative land carbon
 1403 uptake (panels a and c) and fractional emissions taken up by land (panels b and d). Model mean
 1404 is shown for all models but also separately for models whose land components include or do not
 1405 include a representation of the N cycle.



1406



1407

1408 Figure A2: Absolute amounts and the change from the beginning of the BGC simulation for carbon
1409 in soil+litter (panels a and b) and vegetation (panels c and d) pools.

1410

1411



1412

1413 **A4. Additional tables**

1414 **Table A1:** Values of carbon-concentration and carbon-climate feedback parameters for land and
 1415 ocean calculated using the B-C approach (using results from the COU and BGC simulations), and
 1416 the linear transient climate sensitivity to CO₂, from CMIP6 and CMIP5 models at 4×CO₂ (i.e. at
 1417 the end of the 1pctCO₂ simulation) and 2×CO₂.

CMIP6 models at 4×CO ₂					
	Land		Ocean		
	Carbon-climate feedback, γ_L	Carbon-concentration feedback, β_L	Carbon-climate feedback, γ_O	Carbon-concentration feedback, β_O	Climate sensitivity, α
	PgC °C ⁻¹	PgC ppm ⁻¹	PgC °C ⁻¹	PgC ppm ⁻¹	°C ppm ⁻¹
ACCESS-ESM1.5	-21.1	0.37	-23.75	0.9	0.00546
BCC-CSM2-MR	-163.1	1.81	-19.94	0.92	0.00485
CanESM5	15.95	1.28	-14.72	0.77	0.00751
CESM2	-21.6	0.9	-10.85	0.71	0.00637
CNRM-ESM2-1	-83.11	1.36	-9.38	0.7	0.00632
IPSL-CM6A-LR	-8.67	0.62	-12.97	0.76	0.00687
MIROC-ES2L	-69.57	1.12	-22.25	0.73	0.00436
MPI-ESM1.2-LR	-5.17	0.71	-20.11	0.77	0.00512
NOAA-GFDL-ESM4	-80.06	0.93	-21.65	0.84	0.00430
NorESM2-LM	-20.95	0.85	-19.64	0.78	0.00410
UKESM1-0-LL	-38.4	0.75	-14.07	0.75	0.00721
Model mean	-45.07	0.97	-17.21	0.78	0.00568
Standard deviation	48.24	0.38	4.72	0.07	0.00118

1418

CMIP6 models at 2×CO ₂					
	Land		Ocean		
	Carbon-climate feedback, γ_L	Carbon-concentration feedback, β_L	Carbon-climate feedback, γ_O	Carbon-concentration feedback, β_O	Climate sensitivity, α
		PgC °C ⁻¹	PgC ppm ⁻¹	PgC °C ⁻¹	PgC ppm ⁻¹
ACCESS-ESM1.5	-12	0.75	-11.72	1.06	0.00750
BCC-CSM2-MR	-132.84	2.22	-12.38	1.09	0.00592
CanESM5	-6.22	1.42	-7.71	0.9	0.00950
CESM2	-12.76	0.98	-4.24	0.84	0.00789
CNRM-ESM2-1	-44.51	1.37	-3.58	0.81	0.00650
IPSL-CM6A-LR	-12.24	1.11	-7.37	0.87	0.00876
MIROC-ES2L	-63.36	1.45	-10.44	0.85	0.00530
MPI-ESM1.2-LR	-0.81	1.08	-11.4	0.88	0.00636
NOAA-GFDL-ESM4	-50.69	1.08	-8.97	0.97	0.00543
NorESM2-LM	-15.61	0.94	-9.34	0.88	0.00509
UKESM1-0-LL	-24.01	1	-7.35	0.88	0.00885
Model mean	-34.10	1.22	-8.59	0.91	0.00701
Standard deviation	36.61	0.38	2.76	0.09	0.00150



1419

CMIP5 models at 4xCO ₂					
	Land		Ocean		
	Carbon-climate feedback, γ_L	Carbon-concentration feedback, β_L	Carbon-climate feedback, γ_O	Carbon-concentration feedback, β_O	Climate sensitivity, α
		PgC °C ⁻¹	PgC ppm ⁻¹	PgC °C ⁻¹	PgC ppm ⁻¹
BCC-CSM1-1	-109.7	1.4	-17.4	0.85	0.00511
CanESM2	-64.9	0.99	-11.28	0.7	0.00623
CESM1-BGC	-6.39	0.24	-12.16	0.74	0.00481
IPSL-CM5A-LR	-46.65	1.13	-17.6	0.89	0.00559
MIROC-ESM	-86.82	0.75	-20.94	0.82	0.00660
MPI-ESM-LR	-89.64	1.49	-18.36	0.85	0.00582
NorESM-ME	-4.3	0.22	-18.72	0.87	0.00441
HadGEM2-ES	-54.94	1.24	-21.88	0.82	0.00607
Model mean	-57.92	0.93	-17.29	0.82	0.00558
Standard deviation	35.77	0.46	3.54	0.06	0.00070

1420

CMIP5 models at 2xCO ₂					
	Land		Ocean		
	Carbon-climate feedback, γ_L	Carbon-concentration feedback, β_L	Carbon-climate feedback, γ_O	Carbon-concentration feedback, β_O	Climate sensitivity, α
		PgC °C ⁻¹	PgC ppm ⁻¹	PgC °C ⁻¹	PgC ppm ⁻¹
BCC-CSM1-1	-57.61	1.75	-11.06	1.03	0.00676
CanESM2	-48.13	1.05	-6.64	0.85	0.00830
CESM1-BGC	-5.02	0.25	-4.41	0.86	0.00603
IPSL-CM5A-LR	-37.28	1.58	-8.88	0.99	0.00609
MIROC-ESM	-64.79	1.04	-12.36	0.94	0.00778
MPI-ESM-LR	-62.52	1.86	-11.24	0.99	0.00686
NorESM-ME	1.02	0.24	-9.53	1	0.00506
HadGEM2-ES	-21.78	1.43	-11.27	0.92	0.00836
Model mean	-37.01	1.15	-9.42	0.95	0.00690
Standard deviation	24.17	0.59	2.53	0.06	0.00110

1421

1422

1423



1424 **Table A2:** Estimate of the change in the ocean carbon inventory (PgC) expected from a time
 1425 integral of the global air-sea carbon flux into the ocean versus the volume integral of the change
 1426 in the dissolved inorganic carbon, together with the small residual. The time integral of the air-
 1427 sea carbon flux provides the dominant contribution to the change in the ocean carbon inventory,
 1428 although there is a small mismatch due to the land to ocean carbon flux from river runoff and the
 1429 ocean to land carbon flux from carbon burial in ocean sediments.

1430

Model	Time integral of the global air-sea carbon flux into the ocean (PgC)	Global ocean volume integral of Δ DIC (PgC)	Residual (PgC)
ACCESS-ESM1.5	763	736	27
CanESM5	656	651	5
CNRM-ESM2-1	597	658	-61
MIROC-ES2L	625	632	-7
MPI-ESM1.2-LR	657	621	36
NOAA-GFDL-ESM4	720	759	-39
NorESM2-LM	671	628	43
UKESM1-0-LL	637	609	28
Model mean (\bar{x})	666	662	
Standard deviation (σ_x)	53	55	
Coefficient of variation ($\sigma_x/ \bar{x} $)	0.08	0.08	

1431

1432

1433



1434

1435 **Table A3:** Carbon-cycle feedback parameters for the ocean, β_o and γ_o , diagnosed from the air-
 1436 sea carbon fluxes and separately diagnosed for the ocean carbon inventory and its separate
 1437 ocean saturated, disequilibrium and regenerated DIC pools for the subset of eight CMIP6 models
 1438 for which 3D ocean data were available; their sum does not exactly match the diagnostics from
 1439 the air-sea fluxes due to land-ocean interactions involving storage in sediments and river inputs.

1440

	Carbon-concentration feedback (PgC ppm ⁻¹)				Carbon-climate feedback (PgC °C ⁻¹)			
	β_o	β_{sat}	β_{dis}	β_{reg}	γ_o	γ_{sat}	γ_{dis}	γ_{reg}
ACCESS-ESM1.5	0.90	3.54	-2.69	0.005	-23.75	-13.60	-20.47	11.52
CanESM5	0.77	3.83	-3.06	-0.001	-14.72	-10.72	-8.62	4.29
CNRM-ESM2-1	0.70	3.75	-3.01	0.03	-9.38	-14.56	-17.66	29.27
MIROC-ES2L	0.73	3.76	-3.01	-0.001	-22.25	-16.48	-25.50	21.08
MPI-ESM1.2-LR	0.77	3.34	-2.62	0.002	-20.11	-14.37	-15.37	8.40
NorESM2-LM	0.78	3.67	-2.92	-0.004	-19.64	-12.91	-14.44	9.19
UKESM1-0-LL	0.75	3.62	-2.88	-0.02	-14.07	-8.87	-11.04	6.56
NOAA-GFDL-ESM4	0.84	3.77	-2.93	0.05	-21.65	-10.75	-17.77	7.7
Model mean (\bar{x})	0.78	3.66	-2.89	-0.003	-16.95	-12.78	-16.36	12.25
Standard deviation (σ_x)	0.06	0.16	0.16	0.009	5.62	2.50	5.31	8.53
Coefficient of variation ($\sigma_x/ \bar{x} $)	0.08	0.05	0.06	3.00	0.33	0.20	0.33	0.70

1441

1442 **Table A4:** Transient Climate Response (TCE, $\Delta T_{2\times CO_2}$), diagnosed cumulative emissions at
 1443 $2\times CO_2$ ($\bar{E}_{2\times CO_2}$), and transient climate response to cumulative emissions (TCRE) for the eleven
 1444 CMIP6 models considered in this study.

1445

CMIP6 model	TCR (°C)	Cumulative diagnosed emissions (PgC)	TCRE (°C EgC ⁻¹)
ACCESS-ESM1.5	2.13	1064	2.00
BCC-CSM2-MR	1.68	1291	1.30
CanESM5	2.69	1214	2.21
CESM2	2.24	1073	2.08
CNRM-ESM2-1	1.84	1124	1.64
IPSL-CM6A-LR	2.48	1107	2.24
MIROC-ES2L	1.50	1135	1.32
MPI-ESM1.2-LR	1.80	1127	1.60
NOAA-GFDL-ESM4	1.54	1066	1.44
NorESM2-LM	1.44	1075	1.34
UKESM1-0-LL	2.51	1054	2.38
Mean	1.99	1121	1.78
Standard deviation	0.42	70	0.39

1446

1447



1448 **A5. Model descriptions**

1449 **A5.1. Commonwealth Scientific and Industrial Research Organisation (CSIRO) ACCESS-ESM1.5**

1450 The Australian Community Climate and Earth System Simulator ACCESS-ESM1.5 (Ziehn et al.,
1451 2017; Ziehn et al., 2019, The Australian Earth System Model: ACCESS-ESM1.5, in prep) is
1452 comprised of a number of component models. The atmospheric model is the UK Met Office
1453 Unified Model at version 7.3 (Martin et al., 2010, 2011) with their land surface model replaced
1454 with the Community Atmosphere Biosphere Land Exchange (CABLE) model (Kowalczyk et al.,
1455 2013). The ocean component is the NOAA/GFDL Modular Ocean Model (MOM) at version 5
1456 (Griffies, 2014) with the same configuration as the ocean model component of ACCESS1.0 and
1457 ACCESS1.3 (Bi et al., 2013). Sea ice is simulated using the LANL CICE4.1 model (Hunke and
1458 Lipscomb, 2010). Coupling of the ocean and sea-ice to the atmosphere is through the OASIS-MCT
1459 coupler (Valcke, 2013). The physical climate model configuration used here is very similar to the
1460 version (ACCESS1.3) that contributed to the Coupled Model Intercomparison Project Phase 5
1461 (CMIP5) (Bi et al., 2013). The carbon cycle is included in ACCESS through the CABLE land surface
1462 model and its biogeochemistry module, CASA-CNP (Wang et al., 2010), and through the World
1463 Ocean Model of Biogeochemistry and Trophic-dynamics (WOMBAT) (Oke et al., 2013).

1464

1465 The WOMBAT model is based on a NPZD (nutrient-phosphate, phytoplankton, zooplankton and
1466 detritus) model with the additions of bio-available iron limitation, dissolved inorganic carbon,
1467 calcium carbonate, alkalinity and oxygen. Productivity drives uptake and formation of carbon
1468 and oxygen which exchange with the atmosphere. Sinking and remineralization of detritus



1469 carries biogeochemical tracers to the deep ocean. Iron is supplied by dust deposition, continental
1470 shelves and background ocean values.

1471

1472 The Australian community model CABLE simulates the fluxes of momentum, heat, water and
1473 carbon at the surface. The biogeochemistry module CASA-CNP simulates the flow of carbon and
1474 nutrients such as nitrogen and phosphorus between three plant biomass pools (leaf, wood, root),
1475 three litter pools (metabolic, structural, coarse woody debris) and three organic soil pools
1476 (microbial, slow, passive) plus one inorganic soil mineral nitrogen pool and three phosphorus soil
1477 pools.

1478

1479 In the CABLE configuration applied here we use 10 vegetated types and 3 non-vegetated types.
1480 CABLE calculates gross primary production (GPP) and leaf respiration at every time step using a
1481 two-leaf canopy scheme (Wang and Leuning, 1998) as a function of the leaf area index (LAI). This
1482 set-up uses a simulated (prognostic) LAI based on the size of the leaf carbon pool and the specific
1483 leaf area. Daily mean GPP and leaf respiration values are then passed onto CASA-CNP to calculate
1484 daily respiration fluxes and the flow of carbon and nutrients between the pools. Similar to the
1485 previous version, ACCESS-ESM1 (Law et al., 2017; Ziehn et al., 2017), the model is run with
1486 nitrogen and phosphorus limitation enabled.

1487



1488 **A5.2. Beijing Climate Center (BCC) Climate System Model version 2 with Medium Resolution**

1489 **(BCC-CSM2-MR)**

1490 BCC-CSM2-MR (Wu et al., 2019) is the second generation of the BCC model with medium
1491 resolution that was released to run CMIP6 simulations. It is a fully-coupled global climate model
1492 and updated from its previous version of BCC-CSM1.1 used for CMIP5 (Wu et al., 2013). The
1493 atmospheric component of BCC-CSM2-MR is the BCC Atmospheric General Circulation Model
1494 version 3 (BCC-AGCM3-MR, Wu et al., 2019). The land component is the BCC Atmosphere and
1495 Vegetation Interaction Model version 2.0 (BCC-AVIM2, Li et al., 2019) with terrestrial carbon
1496 cycle. The oceanic component is the Modular Ocean Model version 4 with 40 levels (hereafter
1497 MOM4-L40). The sea ice component is Sea Ice Simulator (SIS). These components are physically
1498 coupled through fluxes of momentum, energy, water, and carbon at their interfaces. The
1499 coupling was realized with the flux coupler version 5 developed by the National Center for
1500 Atmosphere Research (NCAR).

1501

1502 The atmospheric component of BCC-CSM2-MR has a horizontal resolution of T106 approximately
1503 1.125° and 46 vertical levels in a hybrid sigma/pressure vertical coordinate system with the top
1504 level at 1.459 hPa. The ocean component resolution of BCC-CSM2-MR is 1° longitude by $1/3^\circ$
1505 latitude between 30°S and 30°N ranged to 1° latitude at 60°S and 60°N and nominally 1°
1506 polarward with tripolar coordinates, and there are 40 z-levels in the vertical.

1507



1508 The atmospheric component model BCC-AGCM3-MR in BCC-CSM2-MR is developed from its
1509 previous CMIP5 version (Wu et al., 2008). The main updates include a modification of deep
1510 convection parameterization, a new scheme for cloud fraction, indirect effects of aerosols
1511 through clouds and precipitation, and the gravity wave drag generated by deep convection (Wu
1512 et al., 2019). Atmospheric CO₂ concentration in BCC-AGCM3-MR for this work is a prognostic
1513 variable and calculated through a budget equation which considered advective transport in the
1514 atmosphere, anthropogenic CO₂ emissions, and interactive CO₂ fluxes at the interfaces with land
1515 and ocean. But chemical processes are not taken into account. The terrestrial carbon cycle in
1516 BCC-AVIM2 (Li et al., 2019) operates through a series of biochemical and physiological processes
1517 on photosynthesis and respiration of vegetation, and takes into account carbon loss due to
1518 turnover and mortality of vegetation, and CO₂ release into atmosphere through soil respiration.
1519 The vegetation litter to the ground surface and into the soil is divided into eight terrestrial carbon
1520 pools (surface structural, surface metabolic, surface microbial, soil structural, soil metabolic, soil
1521 microbial, slow, and passive carbon pools) according to the timescale of the decomposition of
1522 carbon in each pool and transfers between different pools. Allocation to and from the three
1523 vegetation biomass pools (leaf, stem, root) leads to dynamic vegetation that in turn produces
1524 litter fall and ultimate transfer to soil organic carbon. The allocation of carbon to the three
1525 vegetation biomass pools is dependent on light availability, water stress and phenology stages of
1526 the canopy and follows the formulations of Arora and Boer (2005).

1527

1528 The biogeochemistry module to simulate the ocean carbon cycle in MOM4_L40 is based on the
1529 protocols from the Ocean Carbon Cycle Model Intercomparison Project–Phase 2 (OCMIP2,



1530 <http://www.ipsl.jussieu.fr/OCMIP/phase2/>). The OCMIP biogeochemistry module parameterizes
1531 the process of marine biology in terms of geochemical fluxes without explicit representation of
1532 the marine ecosystem and food web processes, and includes five prognostic variables:
1533 phosphate, dissolved organic phosphorus, dissolved oxygen, dissolved inorganic carbon, and
1534 alkalinity. Ocean carbon cycle processes in BCC-CSM2-MR follow OCMIP, except for
1535 parameterizing the export of organic matter from surface waters to deep oceans (Wu et al.,
1536 2013).

1537

1538 **A5.3. Canadian Centre for Climate Modelling and Analysis (CCCma) fifth generation Earth**
1539 **System Model, CanESM5**

1540 CanESM5 has evolved from its predecessor CanESM2 (Arora et al., 2011) that was used in the
1541 Coupled Model Intercomparison Project phase 5 (CMIP5). CanESM5 represents a major update
1542 to CanESM2 and described in detail in Swart et al. (2019). The major changes relative to CanESM2
1543 are the implementation of completely new models for the ocean, sea-ice, marine ecosystems,
1544 and a new coupler. The resolution of CanESM5 (T63 or $\sim 2.8^\circ$ in the atmosphere and $\sim 1^\circ$ in the
1545 ocean) remains similar to CanESM2, and is at the lower end of the spectrum of CMIP6 models.
1546 The atmospheric component of CanESM5 is represented by version 5 of the Canadian
1547 Atmospheric Model (CanAM5) has several improvements relative to its predecessor, CanAM4
1548 (von Salzen et al., 2013) including changes to aerosol, clouds, radiation, land surface and lake
1549 processes. CanAM5 uses a triangular spectral truncation in the model dynamical core, with an
1550 approximate horizontal resolution of 2.8 degrees in latitude/longitude. It uses a hybrid vertical



1551 coordinate system with 49 levels between the surface and 1 hPa, with a vertical resolution of
1552 about 100 m near the surface. Relative to the 35 levels used in CanESM2 most of the additional
1553 14 levels were added in the upper troposphere and stratosphere.

1554

1555 The land surface in CanESM5 is modelled using the Canadian Land Surface Scheme (CLASS;
1556 Verseghy, 2000) and the Canadian Terrestrial Ecosystem Model (CTEM; Arora and Boer, 2005,
1557 2010) which together form the land component of CanESM5. CLASS-CTEM simulate the physical
1558 and biogeochemical land surface processes, respectively, and together they calculate fluxes of
1559 energy, water, CO₂ and wetland CH₄ emissions at the land-atmosphere boundary. Over land,
1560 three permeable soil layers are used with default thicknesses of 0.1, 0.25, and 3.75 m for which
1561 liquid and frozen soil moistures and temperature are prognostically calculated. The depth to
1562 bedrock is specified on the basis of the global data set which reduces thicknesses of the
1563 permeable soil layers where soil depth is less than 4.1 meters. Snow is represented using one
1564 layer whose snow water equivalent and temperature are modelled prognostically. The
1565 introduction of dynamic wetlands and their methane emissions is a new biogeochemical process
1566 added since the CanESM2 (Arora et al., 2018). Nitrogen cycle over land is not represented but
1567 the effect of photosynthesis down-regulation as CO₂ increases is represented. The magnitude of
1568 the parameter representing this down-regulation is increased in CanESM5, compared to
1569 CanESM2, following Arora and Scinocca (2016) who found best value of this parameter that
1570 reproduced various aspects of the historical carbon budget for CanESM4.2 (a model version more
1571 similar to CanESM2 than CanESM5). Other than wetlands, and the changes to the strength of the



1572 CO₂ fertilization effect, the remaining terrestrial ecosystem processes are represented the same
1573 as in CanESM2.

1574

1575 The physical ocean component of CanESM5 is based on NEMO version 3.4.1. It is configured on
1576 the tripolar ORCA1 C-grid with 45 z-coordinate vertical levels, varying in thickness from ~6 m near
1577 the surface to ~250 m in the abyssal ocean. The horizontal resolution is based on a 1° Mercator
1578 grid, varying with the cosine of latitude, with a refinement of the meridional grid spacing to 1/3°
1579 near the equator. Two modifications have been introduced to the NEMO's mesoscale and small-
1580 scale mixing physics in CanESM5 and these are detailed in Swart et al. (2019). Sea ice is
1581 represented using the LIM2 sea ice model (Bouillon et al., 2009; Fichefet and Morales Maqueda,
1582 1997), which is run within the NEMO framework.

1583

1584 Ocean carbon cycle is represented using the Canadian Model of Ocean Carbon (CMOC) which
1585 was developed for earlier versions of CanESM (Arora et al., 2011; Christian et al., 2010), and
1586 includes carbon chemistry and biology. The biological component is a simple Nutrient-
1587 Phytoplankton-Zooplankton-Detritus (NPZD) model, with fixed Redfield stoichiometry, and
1588 simple parameterizations of iron limitation, nitrogen fixation, and export flux of calcium
1589 carbonate.

1590

1591 **A5.4. Community Earth System Model, version 2 (CESM2)**



1592 The CESM2 (Danabasoglu et al., 2019: The Community Earth System Model version 2 - CESM2,
1593 in preparation) contains substantial improvements since CESM1. The resolution remains the
1594 same as in CESM1 (0.9° latitude x 1.25° longitude for the atmosphere and land with 32 vertical
1595 atmospheric levels and 25 ground levels and ~1° for the ocean). The Community Atmosphere
1596 Model version 6 (Neale, R. B. et al., 2019: The NCAR Community Atmosphere Model version 6
1597 (CAM6): Scientific configuration and simulation fidelity, in preparation) includes many changes
1598 to the representation of physical processes with the primary change being the inclusion of the
1599 Cloud Layers Unified By Binormals (CLUBB) unified turbulence scheme.

1600

1601 The CESM2 ocean component (POP2) is largely the same as that used in CESM1 except with a
1602 new parameterization for mixing effects in estuaries along with several other numerical and
1603 physics improvements. The sea ice model is CICE version 5.1.2 (CICE5; (Hunke et al., 2015) .
1604 Ocean biogeochemistry is represented by the Marine Biogeochemistry Library (MARBL). MARBL
1605 represents multiple nutrient co-limitation (N, P, Si, and Fe). It includes three explicit
1606 phytoplankton functional groups (diatoms, diazotrophs, and pico/nano phytoplankton), one
1607 implicit phytoplankton group (calcifiers) and one zooplankton group. MARBL includes prognostic
1608 carbonate chemistry and simulates sinking particulate organic matter. Major updates relative to
1609 CESM1 include a representation of subgrid-scale variations in light and variable C:P
1610 stoichiometry. Atmospheric deposition of iron is computed prognostically in CESM2 as a function
1611 of dust and black carbon deposition simulated by CAM6. Riverine nutrient, carbon, and alkalinity
1612 fluxes are supplied to the ocean from a dataset.



1613

1614 The land component is the Community Land Model version 5 (CLM5, Lawrence et al., 2018) which
1615 simulates land water, energy, momentum, carbon and nitrogen cycling. CLM5 includes an
1616 extensive suite of new and updated processes and parameterizations that collectively improve
1617 the model's hydrological, biogeochemical and ecological realism and enhance the representation
1618 of anthropogenic land use activities on climate and the carbon cycle. The primary updates are as
1619 follows with details, references, and additional updates described and listed in (Lawrence et al.,
1620 2018): (1) updated parameterizations and structure for hydrology and snow (spatially explicit soil
1621 depth, dry surface layer, revised groundwater scheme, revised canopy interception and canopy
1622 snow processes, updated fresh snow density, and inclusion of the Model for Scale Adaptive River
1623 Transport); (2) a plant hydraulics scheme to more mechanistically represent plant water use and
1624 limitation; (3) vertically-resolved soil biogeochemistry with base organic matter decomposition
1625 rates varying with depth and modified by soil temperature, water, and oxygen limitation and
1626 nitrification and denitrification updated as in Century model; (4) a methane production,
1627 oxidation, and emissions model; (5) improved representation of plant N dynamics to address
1628 deficiencies in CLM4 through introduction of flexible plant carbon : nitrogen (C:N) stoichiometry
1629 which avoids the problematic CLM4 separation of potential and actual plant productivity,
1630 explicitly simulating photosynthetic capacity response to environmental conditions through the
1631 Leaf Utilization of Nitrogen for Assimilation (LUNA) module, and accounting for how N availability
1632 affects plant productivity through the Fixation and Uptake of Nitrogen (FUN) module which
1633 determines the C costs of N acquisition; methane emissions and oxidation from natural land
1634 processes; (6) a global active crop model with six crop types and time-evolving irrigated areas



1635 and industrial fertilization rates; (7) updated canopy processes including a revised canopy
1636 radiation scheme and canopy scaling of leaf processes, co-limitations on photosynthesis and
1637 updated stomatal conductance; (8) a new fire model that includes representation of natural and
1638 anthropogenic ignition sources and suppression along with agricultural, deforestation, and peat
1639 fires; and (9) inclusion of carbon isotopes.

1640

1641 **A5.5. Centre National de Recherches Météorologiques (CNRM) CNRM-ESM2-1**

1642 CNRM-ESM2-1 is the second generation Earth System model developed by CNRM-CERFACS for
1643 CMIP6 (Séférian et al., 2019).

1644

1645 The atmosphere component of CNRM-ESM2-1 is based on version 6.3 of the global spectral model
1646 ARPEGE-Climat (ARPEGE-Climat_v6.3). ARPEGE-Climat resolves atmospheric dynamics and
1647 thermodynamics on a T127 triangular grid truncation that offers a spatial resolution of about 150
1648 km in both longitude and latitude. CNRM-ESM2-1 employs a “high-top” configuration with 91
1649 vertical levels that extend from the surface to 0.01 hPa in the mesosphere; 15 hybrid σ -pressure
1650 levels are available below 1500 m.

1651

1652 The surface state variables and fluxes at the surface-atmosphere interface are simulated by the
1653 SURFEX modeling platform version 8.0 over the same grid and with the same time-step as the
1654 atmosphere model. SURFEXv8.0 encompasses several submodules for modeling the interactions



1655 between the atmosphere, the ocean, the lakes and the land surface. Over the land surface,
1656 CNRM-ESM2-1 uses the ISBA-CTRIP land surface modeling system (<http://www.umr->
1657 [cnrm.fr/spip.php?article1092&lang=en](http://www.umr-cnrm.fr/spip.php?article1092&lang=en)) to solve energy, carbon and water budgets at the land
1658 surface (Decharme et al., 2019; Delire et al., 2019). Its physical core explicitly solves the one-
1659 dimensional Fourier and Darcy laws throughout the soil, accounting for the hydraulic and thermal
1660 properties of soil organic carbon. It uses a 12-layer snow model of intermediate complexity that
1661 allows separate water and energy budgets for the soil and the snowpack. It accounts for a
1662 dynamic river flooding scheme in which floodplains interact with the soil and the atmosphere
1663 through free-water evaporation, infiltration and precipitation interception and a two-
1664 dimensional diffusive groundwater scheme to represent unconfined aquifers and upward
1665 capillarity fluxes into the superficial soil. More details on these physical aspects can be found in
1666 Decharme et al. (2019).

1667

1668 To simulate the land carbon cycle and vegetation-climate interactions, ISBA-CTRIP simulates
1669 plant physiology, carbon allocation and turnover, and carbon cycling through litter and soil. It
1670 includes a module for wild fires, land use and land cover changes, and carbon leaching through
1671 the soil and transport of dissolved organic carbon to the ocean. Leaf photosynthesis is
1672 represented by the semi-empirical model proposed by Goudriaan et al. (1985). Canopy level
1673 assimilation is calculated using a 10-layer radiative transfer scheme including direct and diffuse
1674 radiation. Vegetation in ISBA is represented by 4 carbon pools for grasses and crops (leaves, stem,
1675 roots and a non-structural carbohydrate storage pool) with 2 additional pools for trees
1676 (aboveground wood and coarse roots). Leaf phenology results directly from the carbon balance



1677 of the leaves. The model distinguishes 16 vegetation types (10 tree and shrub types, 3 grass types
1678 and 3 crop types) alongside desert, rocks and permanent snow. In the absence of nitrogen cycling
1679 within the vegetation, an implicit nitrogen limitation scheme that reduces specific leaf area with
1680 increasing CO₂ concentration was implemented in ISBA following the meta-analysis of Yin (2002).
1681 Additionally, there is an ad-hoc representation of photosynthesis down-regulation. The litter and
1682 soil organic matter module is based on the soil carbon part of the CENTURY model (Parton et al.,
1683 1988). The 4 litter and 3 soil carbon pools are defined based on their location above- or below-
1684 ground and potential decomposition rates. The litter pools are supplied by the flux of dead
1685 biomass from each biomass reservoir (turnover). Decomposition of litter and soil carbon releases
1686 CO₂ (heterotrophic respiration). During the decomposition process, some carbon is dissolved by
1687 water slowly percolating through the soil column. This dissolved organic carbon is transported by
1688 the rivers to the ocean. A detailed description of the terrestrial carbon cycle can be found in
1689 Delire et al. (2019).

1690

1691 The ocean component of CNRM-ESM2-1 is the Nucleus for European Models of the Ocean
1692 (NEMO) version 3.6 (Madec et al., 2017) which is coupled to both the Global Experimental Leads
1693 and ice for ATmosphere and Ocean (GELATO) sea-ice model (Salas Mélia, 2002) version 6 and
1694 also the marine biogeochemical model Pelagic Interaction Scheme for Carbon and Ecosystem
1695 Studies version 2-gas (PISCESv2-gas). NEMOv3.6 operates on the eORCA1L75 grid (Mathiot et al.,
1696 2017) which offers a nominal resolution of 1° to which a latitudinal grid refinement of 1/3° is
1697 added in the tropics; this grid describes 75 ocean vertical layers using a vertical z*-coordinate
1698 with partial step bathymetry formulation (Bernard et al., 2006).



1699

1700 The atmospheric chemistry scheme of CNRM-ESM2-1 is Reactive Processes Ruling the Ozone
1701 Budget in the Stratosphere version 2 (REPROBUS-C_v2). This scheme resolves the spatial
1702 distribution of 63 chemistry species but does not represent the low troposphere ozone non-
1703 methane hydrocarbon chemistry. CNRM-ESM2-1 also includes an interactive tropospheric
1704 aerosol scheme included in the atmospheric component ARPEGE-Climat. This aerosol scheme,
1705 named Tropospheric Aerosols for Climate In CNRM (TACTIC_v2), represents the main
1706 anthropogenic and natural aerosol species of the troposphere.

1707

1708 The ocean biogeochemical component of CNRM-ESM2-1 uses the Pelagic Interaction Scheme for
1709 Carbon and Ecosystem Studies model volume 2 version trace gases (PISCESv2-gas), which derives
1710 from PISCESv2 as described in Aumont et al. (2015). PISCESv2-gas simulates the distribution of
1711 five nutrients (from macronutrients: nitrate, ammonium, phosphate, and silicate to
1712 micronutrient: iron) which regulate the growth of two explicit phytoplankton classes
1713 (nanophytoplankton and diatoms). Dissolved inorganic carbon (DIC) and alkalinity (Alk) are
1714 involved in the computation of the carbonate chemistry, which is resolved by “Model the Ocean
1715 Carbonate SYstem” version 2 (MOCSY 2.0, Orr & Epitalon, 2015) in PISCESv2-gas. MOCSY 2.0
1716 enables a better and faster resolution of the ocean carbonate chemistry at thermodynamic
1717 equilibria. Oxygen is prognostically simulated using two different oxygen-to-carbon ratios, one
1718 when ammonium is converted to or mineralized from organic matter, the other when oxygen is
1719 consumed during nitrification. Their values have been set respectively to 131/122 and 32/122.



1720

1721 At ocean surface, PISCESv2-gas exchanges carbon, oxygen, dimethylsulfide (DMS) and nitrous
1722 oxide (N₂O) tracers with the atmosphere using the revised air-sea exchange bulk as published by
1723 Wanninkhof (2014). PISCESv2-gas uses several boundary conditions which represent the supply
1724 of nutrients from five different sources: atmospheric deposition, rivers, sediment mobilization,
1725 sea-ice and hydrothermal vents.

1726

1727 **A5.6. Institut Pierre Simon Laplace (IPSL) IPSL-CM6A-LR**

1728 IPSL-CM6A-LR is the coupled climate model of the Institut Pierre Simon Laplace (Servonnat et al.,
1729 2019, in preparation). It results from the integration of the following components: the LMDZ
1730 atmospheric general circulation model (version 6A-LR, Hourdin et al., 2019), the NEMO oceanic
1731 model (version 3.6, Aumont et al., 2015; Madec et al., 2017; Rousset et al., 2015; Vancoppenolle
1732 et al., 2009) and the ORCHIDEE land surface model (version 2.0, Peylin et al., 2019, in
1733 preparation).

1734

1735 The atmospheric general circulation model LMDZ6A-LR builds onto its previous version that has
1736 notably incorporated advances in the parameterization of turbulence, convection, and clouds.
1737 More specifically, LMDZ6A-LR includes a turbulent scheme based on the prognostic equation for
1738 the turbulent kinetic energy that follows Yamada (1983), a mass flux representation of the
1739 organized structures of the convective boundary layer called "Thermal Plume Model" (Hourdin



1740 et al., 2002; Rio et al., 2010; Rio and Hourdin, 2008), and a parameterization of the cold pools or
1741 wakes created below cumulonimbus by the evaporation of convective rainfall (Grandpeix et al.,
1742 2010; Grandpeix and Lafore, 2010). It is based on a regular horizontal grid with 144 grid points
1743 regularly spaced in longitude and 142 in latitude, corresponding to a resolution of $2.5^\circ \times 1.3^\circ$, and
1744 79 vertical layers.

1745

1746 IPSL-CM6A-LR further includes NEMO (Nucleus for European Models of the Ocean), which is itself
1747 composed of three major building blocks: the ocean physics NEMO-OPA (Madec et al., 2017), the
1748 sea-ice dynamics and thermodynamics NEMO-LIM3 (Rousset et al., 2015; Vancoppenolle et al.,
1749 2009), and the ocean biogeochemistry NEMO-PISCES (Aumont et al., 2015). The grid used has a
1750 nominal resolution of 1° in the zonal and meridional directions with a latitudinal grid refinement
1751 of $1/3^\circ$ in the Tropics. Vertical discretization uses a partial step formulation (Bernard et al., 2006),
1752 which ensures a better representation of bottom bathymetry, with 75 levels. The initial layer
1753 thicknesses increase non-uniformly from 1 m at the surface to 10 m at 100 m depth, and reaches
1754 200 m at the bottom, and are subsequently time-dependent. NEMO-PISCES (Aumont et al., 2015)
1755 models the lower trophic levels of marine ecosystem (phytoplankton, microzooplankton and
1756 mesozooplankton) and the biogeochemical cycles of carbon and of the main nutrients (P, N, Fe,
1757 and Si). This model is also able to compute air-sea carbon fluxes.

1758

1759 Finally, IPSL-CM6A-LR includes ORCHIDEE, a global process-based terrestrial biosphere model
1760 Krinner et al. (2005); Peylin et al., 2019, in preparation) that calculates carbon, water and energy



1761 fluxes between the land surface and the atmosphere. Photosynthesis and all components of the
1762 surface energy and water budgets are calculated at a half-hourly resolution while the dynamics
1763 of the carbon storage (including carbon allocation in plant reservoirs, soil carbon dynamics, and
1764 litter decomposition) are resolved on a daily basis. Photosynthesis depends on light availability
1765 and CO₂ concentration, soil moisture and temperature and is parameterized based on Farquhar
1766 et al. (1980) and Collatz et al. (1992) for C₃ and C₄ plants, respectively. This latest version of
1767 ORCHIDEE includes a downregulation capability that models a reduction of the terrestrial
1768 photosynthesis rates as a function of CO₂ concentration. In ORCHIDEE, the spatial distribution of
1769 vegetation is represented using 15 plant functional types (PFTs) (Cramer, 1997; Prentice et al.,
1770 1992; Wullschlegel et al., 2014). More precisely these PFTs are decomposed into 3 groups
1771 according to their physiological behavior under similar climate conditions: tall vegetation
1772 (forests) is represented by 8 PFTs, short vegetation (grasses and crops) is represented by 6 PFTs,
1773 and bare soil. The fractional coverage of these PFTs vary geographically. A soil type is associated
1774 with each one of these 3 PFT groups. This 3-group partitioning allows for dividing each grid box
1775 into 3 tiles for which an independent hydrological budget is calculated, using the 11-layer
1776 physically based hydrology scheme. In ORCHIDEE the wood harvest product from the LUHv2h
1777 database is used in addition to the annual land cover maps.

1778

1779 **A5.7. Team MIROC (Japan Agency for Marine-Earth Science and Technology / the University of**
1780 **Tokyo / the National Institute for Environmental Studies) MIROC-ES2L**

1781



1782 MIROC-ES2L (Hajima et al., 2019a) is based on the global climate model MIROC5.2 (Tatebe et al.,
1783 2018), which is a minor updated version of MIROC5 used for CMIP5 (Watanabe et al., 2010). The
1784 physical core shares almost same structure and characteristics with the latest model MIROC6
1785 (Tatebe et al., 2019), except for the atmospheric spatial resolution and treatment of cumulus
1786 clouds. This model interactively couples an atmospheric general circulation model (CCSR-NIES
1787 AGCM, Tatebe et al., 2019) including an on-line aerosol component (SPRINTARS, Takemura et al.,
1788 2000), an ocean GCM with sea-ice component (COCO, Hasumi, 2015), and a land physical surface
1789 model (MATSIRO, Takata et al., 2003). The land and ocean biogeochemical components are
1790 represented by VISIT (Ito and Inatomi, 2012) and OECO2 (Hajima et al., 2019a), respectively,
1791 which are interactively coupled to the atmospheric component. There exists another branched
1792 version that has atmospheric chemistry component with finer atmospheric grid (MIROC-ES2H),
1793 but not used in this study.

1794

1795 The atmospheric grid resolution is approximately 2.81° with 40 vertical levels between the
1796 surface and about 3 hPa. For the ocean, the model employs tripolar coordinate system with 62
1797 vertical levels. To the south of 63°N , the ocean model has longitudinal grid spacing of about 1° ,
1798 while the meridional grid spacing varies from about 0.5° near the equator to 1° in the mid-
1799 latitudes. Over the Arctic ocean the grid resolution is even finer following the tripolar coordinate
1800 system. The physical terrestrial component resolves vertical soil profile with 6 layers down to
1801 14m depth, with two types of land-use tiles (agriculture and non-agriculture). Terrestrial
1802 biogeochemical component considers two layered soil organic matter (the upper litter layer and



1803 the lower humus layer), with 5 types of land-use tiles (primary vegetation, secondary vegetation,
1804 urban, crop, and pasture).

1805

1806 The terrestrial biogeochemical component covers major processes relevant to global carbon
1807 cycle, with vegetation (leaf, stem, and root), litter (leaf, stem, and root), and humus (active,
1808 intermediate, and passive) pools and with a static biome distribution. Details on carbon cycle
1809 processes in the model can be found in (Ito and Oikawa, 2002). N cycle is simulated with N
1810 pools of vegetation (canopy and structural), organic soil (litter, humus, and microbe), and
1811 inorganic nitrogen (ammonium and nitrate). The model considers two major nitrogen influxes
1812 into ecosystem (biological nitrogen fixation and external nitrogen inputs). Fluxes out of land
1813 ecosystem in the model are N_2/N_2O emissions, leaching, NH_3 emission, and other emission like
1814 volatilization from land-use product pools. For installing into MIROC-ES2L, the terrestrial
1815 ecosystem processes were modified such that photosynthetic capacity is controlled by leaf N
1816 concentration. Processes associated with land-use change are also modified to take full
1817 advantage of CMIP6 LUC forcing dataset. Further details can be found in (Hajima et al., 2019a).

1818

1819 The new ocean biogeochemical component model, OECO2, is a NPZD-type model and modified
1820 from the previous model (Watanabe et al., 2011). The biogeochemical compartments of OECO2
1821 are nitrate, phosphate, dissolved iron, dissolved oxygen, two types of phytoplankton (non-
1822 diazotroph and diazotroph), zooplankton, and particulate detritus. There exist other
1823 compartments of dissolved inorganic carbon (DIC), total alkalinity, calcium, calcium carbonate,



1824 and N₂O. All organic materials have identical elemental stoichiometric ratio. The model considers
1825 external nutrient inputs (atmospheric N/Fe deposition, inorganic N/P from rivers, biological N
1826 fixation, Fe input from ocean bottom/shelf) and nutrient loss (denitrification for N and loss into
1827 sediment for N, P, and Fe). The emission, transportation and deposition processes of iron are
1828 explicitly simulated by the atmospheric aerosol component.

1829

1830 **A5.8. Max Planck Institute for Meteorology (MPI) MPI-ESM1.2-LR**

1831 The MPI-ESM1.2-LR model (Mauritsen et al., 2019) consists of ocean, atmosphere, land and sea-
1832 ice components which are connected via a coupler analogous to the predecessor MPI-ESM
1833 versions (Giorgetta et al., 2013). The atmosphere model, ECHAM6.3, at the LR resolution has a
1834 spectral truncation at T63 or approximately 200-km grid spacing with 47 vertical levels. It is
1835 directly coupled to the land model, JSBACH3.2, through surface exchange of mass, momentum,
1836 and heat. The ocean general circulation model, MPIOM1.6 in MPI-ESM1.2-LR runs on a bi-polar
1837 grid GR1.5 and has 40 unevenly placed levels. It computes transport of tracers of the ocean
1838 biogeochemistry model HAMOCC6 (Ilyina et al., 2013; Paulsen et al., 2017). The MPI-ESM-LR
1839 configuration computes 45–85 model years per physical day enabling new simulations which
1840 were not feasible previously, such as for instance, large ensemble simulations (Maher et al.,
1841 2019) or millennial-scale simulations with interactive carbon cycle (Brovkin et al., 2019).

1842

1843 Terrestrial vegetation in JSBACH includes vegetation dynamics which interacts with land use
1844 changes (Reick et al., 2013), accounting for the latest changes in the land use harmonization



1845 dataset by Hurtt et al. (2006). The new SPITFIRE model simulates burned area and carbon
1846 emissions to atmosphere due to wildfires and anthropogenic fires (Lasslop et al., 2014), replacing
1847 old global fire parameterization used in the CMIP5 model. Soil carbon model YASSO simulates
1848 dynamics of 4 fast soil carbon pools which are different for leaf and woody litter types, plus a
1849 slow humus pool (Goll et al., 2015). Nitrogen and carbon pools are coupled based on CO₂-induced
1850 nitrogen limitation (Goll et al., 2017).

1851

1852 The ocean biogeochemistry model HAMOCC6 has been extended as compared to the previous
1853 version described in Ilyina et al. (2013) to explicitly resolve nitrogen-fixing cyanobacteria as an
1854 additional prognostic phytoplankton class (Paulsen et al., 2017). This allows to capture the
1855 response of N₂ fixation and ocean biogeochemistry to changing climate conditions. Additionally,
1856 updates of existing processes have been performed. This includes for instance the addition of a
1857 vertically varying settling rate for detritus following the formulation by Martin et al. (1987).
1858 Finally some empirical relationships in the parameterized processes have been updated to follow
1859 recommendations of the C4MIP and OMIP protocols (Jones et al., 2016; Orr et al., 2017). The full
1860 overview of changes in HAMOCC is given in Mauritsen et al. (2019).

1861

1862 **A5.9. Geophysical Fluid Dynamics Laboratory (GFDL) NOAA-GFDL-ESM4**

1863



1864 GFDL-ESM4.1 is a comprehensive, fully-coupled Earth System Model developed by NOAA's
1865 Geophysical Dynamics Laboratory with a fully-interactive carbon cycle and interactive
1866 atmospheric chemistry (Dunne et al., 2019, in prep., The GFDL Earth System Model version 4.1
1867 (GFDL-ESM4.1): Model description and simulation characteristics) that builds on previous
1868 generation modeling efforts of the carbon cycle (ESM2-series) (Dunne et al., 2012, 2013) and
1869 atmospheric chemistry (CM3) (Donner et al., 2011) along with increased resolution and improved
1870 numerics and physics akin to GFDL's 4th generation coupled climate model (CM4.0; Held et al.,
1871 2019, in preparation), and representation of additional Earth System Processes.

1872

1873 The atmospheric component, GFDL AM4.1, is based on the third generation finite volume cube-
1874 sphere dynamical core (FV3) (Lin, 2004) with a 1° horizontal resolution and 49 vertical levels. The
1875 model top is located at ~0.1 hPa to resolve the stratosphere. AM4.1 shares the critical
1876 developments in model physics with the AM4.0 model (Zhao et al., 2018) including radiation,
1877 convection, and clouds. AM4.1 differs from the AM4.0 model in its enhanced vertical resolution
1878 and its more explicit representation of atmospheric chemistry that motivated a separate
1879 radiative and gravity wave tuning.

1880

1881 AM4.1 includes interactive tropospheric and stratospheric gas-phase and aerosol chemistry
1882 represented through 56 prognostic (transported) tracers and 36 diagnostic (non-transported)
1883 chemical tracers. The tropospheric chemistry includes reactions for the oxidation of methane
1884 among other volatile organic compounds. The stratospheric chemistry accounts for the major



1885 ozone loss cycles and heterogeneous reactions on liquid and solid stratospheric aerosols. Details
1886 on the base chemical mechanism including improvements relative to the previous generation
1887 model (AM3) are included in Horowitz et al. (2019, in prep).

1888

1889 Land hydrology and ecosystem dynamics are represented by the GFDL Land Model version 4.1
1890 (LM4p1; Shevliakova et al., 2019, in prep) and builds on the previous generation LM3.1 model
1891 (Milly et al., 2014). Soil carbon dynamics and biogeochemistry represented through the CORPSE
1892 model (Sulman et al., 2019) with an explicit treatment of soil microbes. LM4.1 also includes a
1893 new fire model FINAL (Rabin et al., 2018). Vegetation dynamics represented by the second
1894 generation age-height structured approach the Perfect Plasticity Approximation (PPA) (Weng et
1895 al., 2015, Martinez Cano et al., 2019, in prep). There are 6 carbon pools in LM4.1 representing
1896 leaves, fine roots, heartwood, sapwood, seeds, and non-structural carbon (i.e. sugars). Litter is
1897 broken into leaf and coarse wood categories as well into fast and slow timescale partitions. Soil
1898 has 20 vertical levels each with its own prognostic state for energy, water and soil carbon
1899 variables. There are 5 types of vegetation forms in LM4.1 representing C₃ grass, C₄ grass, tropical
1900 trees, temperate deciduous trees, cold evergreen trees. A combination of these vegetation types
1901 could coexist in some location. The model also includes a new treatment of stomatal conductance
1902 and plant hydraulics. The vegetation state is used to drive a dust emission model that is coupled
1903 with the atmosphere for transport (Ginoux et al., 2019, in prep.). ESM4 implementation of LM4.1
1904 does not include an interactive nitrogen cycle.

1905



1906 The ocean biogeochemical component of ESM4 is version 2 of the Carbon, Ocean
1907 Biogeochemistry and Lower Trophics (COBALTv2) model (Stock et al., 2014b). COBALTv2 uses 33
1908 tracers to represent carbon, alkalinity, oxygen, nitrogen, phosphorus, iron, silica, calcite and
1909 lithogenic mineral cycling within the ocean. Relative to previous generation ocean
1910 biogeochemistry models developed at GFDL, COBALTv2 includes an enhanced representation of
1911 plankton food web dynamics to resolve the flow of energy from phytoplankton to fish (Stock et
1912 al., 2014a) and enhance the model's capacity to resolve linkages between food webs and
1913 biogeochemical cycles. COBALTv2 explicitly includes small, large (split into diatoms and non-
1914 diatoms), and diazotrophic phytoplankton groups, three zooplankton groups, bacteria and three
1915 labilities of dissolved organic matter. Other updates include a temperature-dependence to
1916 sinking organic matter remineralization (Laufkötter et al., 2017), the addition of semi-labile
1917 dissolved organic material, carbonate chemistry calculations based on the open source Model of
1918 the Ocean Carbonate SYstem version 2.0 (Orr and Epitalon, 2015).

1919

1920 Data from the NOAA-GFDL-ESM4 model used in the analysis presented in this paper are
1921 accessible via the Earth System Grid Federation (ESGF) for 1pctCO2 (Krasting et al., 2019b)
1922 simulation and for its radiatively- and biogeochemically-coupled configurations (Krasting et al.,
1923 2019a).

1924

1925 **A5.10. Norwegian Climate Centre (NCC) NorESM2-LM**



1926 The NorESM2-LM is based on the latest release of the Community Earth System Model
1927 (CESM2.1), whose development is supported by the National Center for Atmospheric Research
1928 at the United States. NorESM2 keeps the original land and sea-ice components of CESM2.1 (i.e.,
1929 CLM5, and CICE5, respectively). The atmospheric component is CAM6 (as in CESM), but with
1930 modifications regarding the energy and angular momentum conservation. Further, the
1931 atmospheric chemistry module of CAM6 has been replaced by the scheme developed by the
1932 Norwegian Meteorological Institute. The ocean physical and biogeochemical components of
1933 NorESM2 are the isopycnal ocean circulation and carbon cycle components updated from
1934 NorESM1 version (Schwinger et al., 2016; Tjiputra et al., 2013)

1935

1936 The CLM5 (Community Land Model version 5) prognostically simulates the carbon and nitrogen
1937 cycles, which include natural vegetation, crops, and soil biogeochemistry. The carbon and
1938 nitrogen budgets comprise leaf, live stem, dead stem, live coarse root, dead coarse root, fine-
1939 root, and grain pools. Each of these pools has short-term and long-term storage of non-structural
1940 carbohydrates and labile nitrogen. In addition to the vegetation pools, CLM includes a series of
1941 decomposing carbon and nitrogen pools as vegetation successively breaks down to coarse woody
1942 debris, and/or litter, and subsequently to soil organic matter. Details on the CLM5 models are
1943 available in Lawrence et al. (2018).

1944

1945 Similar to the earlier version, the ocean carbon cycle component in NorESM2 is based on the
1946 Hamburg Oceanic Carbon Cycle (HAMOCC; Maier-Reimer et al., 2005) model, which has been



1947 adopted to the isopycnic ocean general circulation model. The current version includes new
1948 processes, refined parameterizations, as well as new diagnostic tracers. The ecosystem model is
1949 based on an NPZD-type model with multi nutrient limitation in its phytoplankton growth
1950 formulation. Riverine fluxes of inorganic and organic carbon as well as nutrients are now
1951 implemented. Unlike the earlier version, the sea-to-air dimethyl sulfate (DMS) fluxes alter the
1952 atmospheric radiative forcing and hence the climate carbon cycle feedback. More details on the
1953 ocean carbon cycle of NorESM2 are available in Tjiputra et al. (2019, in preparation).

1954

1955 **A5.11. The United Kingdom Community Earth System Model, UKESM1-0-LL**

1956 UKESM1-0-LL (Sellar et al., 2019) is based upon the HadGEM3-GC3.1 (Williams et al., 2018) global
1957 climate model which includes coupled ocean, atmosphere, land and sea-ice components. The
1958 atmosphere component is the Unified Model with a resolution of 1.875° by 1.25° with 85 vertical
1959 levels up to a model top of 90 km (Walters et al., 2019) and includes a modal aerosol scheme
1960 (Mann et al., 2010). The ocean component uses the NEMO dynamical ocean at 1° resolution with
1961 75 vertical levels (Storkey et al., 2018). The sea-ice component uses CICE on the same grid as the
1962 ocean with 5-ice thickness categories (Ridley et al., 2018). The land component uses the JULES
1963 land surface model (Wiltshire et al., in preparation), however, the land surface configuration is
1964 substantially updated for UKESM. The primary differences between the physical and earth system
1965 models is the inclusion of a terrestrial carbon and nitrogen cycle (Wiltshire et al., in preparation),
1966 ocean biogeochemistry (Yool et al., 2013) and tropospheric-stratospheric chemistry model.
1967 Atmospheric chemistry in UKESM1 is simulated by the UKCA chemistry and aerosol model with



1968 the specific configuration a combination of tropospheric (O'Connor et al., 2014) and
1969 stratospheric chemistry (Morgenstern et al., 2009, 2017).

1970

1971 Terrestrial biogeochemistry is represented by the JULES-ES model cycle (Wiltshire et al., in
1972 preparation). The land surface is represented by 13 plant functional types (PFTs) including 4
1973 managed crop and pasture land types. The height, leaf area index and spatial distribution of the
1974 PFTs are dynamic simulated by TRIFFID dynamic global vegetation model (Cox, 2001). Soil carbon
1975 is represented by the 4 pool Roth-C scheme (Coleman and Jenkinson, 1999). Terrestrial carbon
1976 uptake may be limited by the availability of nitrogen. Nitrogen does not directly affect
1977 photosynthetic capacity through leaf N concentrations but acts indirectly by controlling the
1978 biomass and leaf area index within the TRIFFID DGVM. A second mechanism acts through soil
1979 carbon by limiting the decomposition of litter into soil carbon in the RothC model. The vegetation
1980 model includes retranslocation of Nitrogen during senescence of leaves and roots into a labile
1981 pool to supply nutrients for the following seasonal leaf out. The soil model simulates
1982 mineralisation and immobilisation with mineralised nitrogen becoming available for plant uptake
1983 and ecosystem loss. Inorganic Nitrogen is represented by a single gridbox pool from which all
1984 PFTs have equal access. Nitrogen deposition is prescribed from ancillary data.

1985

1986 Land-use change is represented by the application of time-varying fields of crop and pasture to
1987 the DGVM, which allocates space dynamically to C₃ and C₄, crop and pasture types. Pasture is
1988 represented as natural grass whereas crops include a harvest parameterization and are fertilized.



1989 Biogenic Volatile Organic Compound (BVOC) emissions from vegetation are simulated and affect
1990 the formation of secondary organic aerosols. Mineral dust is emitted from bare soil and acts as
1991 both an aerosol and a fertiliser to the ocean.

1992

1993 Ocean biogeochemistry is represented by MEDUSA-2 (Yool et al., 2013) which resolves a dual
1994 size-structured ecosystem of small (nanophytoplankton and microzooplankton) and large
1995 (microphytoplankton and mesozooplankton) components. This explicitly includes the
1996 biogeochemical cycles of nitrogen, silicon and iron nutrients as well as the cycles of carbon,
1997 alkalinity and dissolved oxygen. Large phytoplankton are treated as diatoms and utilise silicic acid
1998 in addition to nitrogen, iron and carbon. Like the living components, the detrital components are
1999 split into two size classes. At the seafloor, MEDUSA-2 resolves 5 reservoirs to temporarily store
2000 sinking organic material reaching the sediment. The model's nitrogen, silicon and alkalinity cycles
2001 are closed and conservative (e.g. no riverine inputs), while the other three cycles (carbon, iron,
2002 oxygen) are open. The ocean's iron cycle includes aeolian (land derived dust) and benthic sources,
2003 and is depleted by scavenging. The ocean's carbon cycle exchanges CO₂ with the atmosphere.
2004 The ocean's oxygen cycle exchanges with the atmosphere, and dissolved oxygen is additionally
2005 created by primary production and depleted by remineralisation. Ocean biogeochemistry also
2006 feeds back on the atmosphere through the production of marine DMS and marine organic
2007 aerosols.

2008

2009 **A6. Contribution of uncertainties in $\Delta T_{2\times CO_2}$ and $\tilde{E}_{2\times CO_2}$ to TCRE.**



2010

2011 The uncertainty in TCRE, as indicated by its standard deviation (σ_{TCRE}), can be represented in
2012 terms of the standard deviation of $\Delta T_{2\times CO_2}$ ($\sigma_{\Delta T}$), standard deviation of $\tilde{E}_{2\times CO_2}$ (σ_E), and their
2013 means $\overline{\Delta T}$ and \overline{E} across the eleven CMIP6 models. Since $\Delta T_{2\times CO_2}$ and $\tilde{E}_{2\times CO_2}$ are nearly
2014 independent (correlation between these two quantities is only 0.02 across the eleven CMIP6
2015 models considered here), we can write

2016
$$\sigma_{TCRE} = \overline{TCRE} \cdot \sqrt{\left(\frac{\sigma_{\Delta T}}{\overline{\Delta T}}\right)^2 + \left(\frac{\sigma_E}{\overline{E}}\right)^2} \quad (A8)$$

2017 which allows to calculate to contributions of $\left(\frac{\sigma_{\Delta T}}{\overline{\Delta T}}\right)^2$ and $\left(\frac{\sigma_E}{\overline{E}}\right)^2$ to σ_{TCRE} .

2018

2019

2020

2021

2022

2023

2024

2025

2026

2027

2028



2029 References

2030

2031 Ainsworth, E. A. and Long, S. P.: What have we learned from 15 years of free-air CO₂ enrichment
2032 (FACE)? A meta-analytic review of the responses of photosynthesis, canopy properties and plant
2033 production to rising CO₂, *New Phytol.*, 165(2), 351–372, doi:10.1111/j.1469-8137.2004.01224.x, 2005.

2034 Arora, V. K. and Boer, G. J.: A parameterization of leaf phenology for the terrestrial ecosystem
2035 component of climate models, *Glob. Change Biol.*, 11(1), 39–59, doi:10.1111/j.1365-2486.2004.00890.x,
2036 2005.

2037 Arora, V. K. and Boer, G. J.: Uncertainties in the 20th century carbon budget associated with land use
2038 change, *Glob. Change Biol.*, 16(12), 3327–3348, doi:10.1111/j.1365-2486.2010.02202.x, 2010.

2039 Arora, V. K. and Scinocca, J. F.: Constraining the strength of the terrestrial CO₂ fertilization effect in the
2040 Canadian Earth system model version 4.2 (CanESM4.2), *Geosci. Model Dev.*, 9(7), 2357–2376,
2041 doi:10.5194/gmd-9-2357-2016, 2016.

2042 Arora, V. K., Scinocca, J. F., Boer, G. J., Christian, J. R., Denman, K. L., Flato, G. M., Kharin, V. V., Lee, W. G.
2043 and Merryfield, W. J.: Carbon emission limits required to satisfy future representative concentration
2044 pathways of greenhouse gases, *Geophys. Res. Lett.*, 38(5), doi:10.1029/2010GL046270, 2011.

2045 Arora, V. K., Boer, G. J., Friedlingstein, P., Eby, M., Jones, C. D., Christian, J. R., Bonan, G., Bopp, L.,
2046 Brovkin, V., Cadule, P., Hajima, T., Ilyina, T., Lindsay, K., Tjiputra, J. F. and Wu, T.: Carbon–Concentration
2047 and Carbon–Climate Feedbacks in CMIP5 Earth System Models, *J. Clim.*, 26(15), 5289–5314,
2048 doi:10.1175/JCLI-D-12-00494.1, 2013a.

2049 Arora, V. K., Boer, G. J., Friedlingstein, P., Eby, M., Jones, C. D., Christian, J. R., Bonan, G., Bopp, L.,
2050 Brovkin, V., Cadule, P., Hajima, T., Ilyina, T., Lindsay, K., Tjiputra, J. F. and Wu, T.: Carbon–Concentration
2051 and Carbon–Climate Feedbacks in CMIP5 Earth System Models, *J. Clim.*, 26(15), 5289–5314,
2052 doi:10.1175/JCLI-D-12-00494.1, 2013b.

2053 Arora, V. K., Melton, J. R. and Plummer, D.: An assessment of natural methane fluxes simulated by the
2054 CLASS-CTEM model, *Biogeosciences*, 15(15), 4683–4709, doi:10.5194/bg-15-4683-2018, 2018.

2055 Aumont, O., Ethé, C., Tagliabue, A., Bopp, L. and Gehlen, M.: PISCES-v2: an ocean biogeochemical model
2056 for carbon and ecosystem studies, *Geosci. Model Dev.*, 8(8), 2465–2513, doi:10.5194/gmd-8-2465-2015,
2057 2015.

2058 Bernard, B., Madec, G., Penduff, T., Molines, J.-M., Treguier, A.-M., Le Sommer, J., Beckmann, A.,
2059 Biastoch, A., Böning, C., Dengg, J., Derval, C., Durand, E., Gulev, S., Remy, E., Talandier, C., Theetten, S.,
2060 Maltrud, M., McClean, J. and De Cuevas, B.: Impact of partial steps and momentum advection schemes
2061 in a global ocean circulation model at eddy-permitting resolution, *Ocean Dyn.*, 56(5), 543–567,
2062 doi:10.1007/s10236-006-0082-1, 2006.

2063 Bernardello, R., Marinov, I., Palter, J. B., Sarmiento, J. L., Galbraith, E. D. and Slater, R. D.: Response of
2064 the Ocean Natural Carbon Storage to Projected Twenty-First-Century Climate Change, *J. Clim.*, 27(5),
2065 2033–2053, doi:10.1175/JCLI-D-13-00343.1, 2014.



- 2066 Bi, D., Dix, M., Marsland, S., O'Farrell, S., Rashid, H., Uotila, P., Hirst, A., Kowalczyk, E., Golebiewski, M.,
2067 Sullivan, A., Yan, H., Hannah, N., Franklin, C., Sun, Z., Vohralik, P., Watterson, I., Zhou, X., Fiedler, R.,
2068 Collier, M., Ma, Y., Noonan, J., Stevens, L., Uhe, P., Zhu, H., Griffies, S., Hill, R., Harris, C. and Puri, K.: The
2069 ACCESS coupled model: description, control climate and evaluation, *Aust Meteor Oceanogr J*, 63(1), 41–
2070 64, doi:<https://doi.org/10.22499/2.6301.004>, 2013.
- 2071 Boer, G. J. and Arora, V.: Geographic Aspects of Temperature and Concentration Feedbacks in the
2072 Carbon Budget, *J. Clim.*, 23(3), 775–784, doi:10.1175/2009JCLI3161.1, 2010.
- 2073 Bouillon, S., Maqueda, M. Á. M., Legat, V. and Fichet, T.: An elastic–viscous–plastic sea ice model
2074 formulated on Arakawa B and C grids, *Ocean Model.*, 27(3), 174–184,
2075 doi:<https://doi.org/10.1016/j.ocemod.2009.01.004>, 2009.
- 2076 Bounoua, L., Collatz, G. J., Sellers, P. J., Randall, D. A., Dazlich, D. A., Los, S. O., Berry, J. A., Fung, I.,
2077 Tucker, C. J., Field, C. B. and Jensen, T. G.: Interactions between Vegetation and Climate: Radiative and
2078 Physiological Effects of Doubled Atmospheric CO₂, *J. Clim.*, 12(2), 309–324, doi:10.1175/1520-
2079 0442(1999)012<0309:IBVACR>2.0.CO;2, 1999.
- 2080 Brovkin, V., Lorenz, S., Raddatz, T., Ilyina, T., Stemmler, I., Toohey, M. and Claussen, M.: What was the
2081 source of the atmospheric CO₂ increase during the Holocene?, *Biogeosciences*, 16(13), 2543–2555,
2082 doi:10.5194/bg-16-2543-2019, 2019.
- 2083 Cao, L., Bala, G., Caldeira, K., Nemani, R. and Ban-Weiss, G.: Importance of carbon dioxide physiological
2084 forcing to future climate change, *Proc. Natl. Acad. Sci.*, 107(21), 9513, doi:10.1073/pnas.0913000107,
2085 2010.
- 2086 Chadwick, R., Douville, H. and Skinner, C. B.: Timeslice experiments for understanding regional climate
2087 projections: applications to the tropical hydrological cycle and European winter circulation, *Clim. Dyn.*,
2088 49(9), 3011–3029, doi:10.1007/s00382-016-3488-6, 2017.
- 2089 Choudhury, B. J.: Carbon use efficiency, and net primary productivity of terrestrial vegetation, *Adv.*
2090 *Space Res.*, 26(7), 1105–1108, doi:[https://doi.org/10.1016/S0273-1177\(99\)01126-6](https://doi.org/10.1016/S0273-1177(99)01126-6), 2000.
- 2091 Christian, J. R., Arora, V. K., Boer, G. J., Curry, C. L., Zahariev, K., Denman, K. L., Flato, G. M., Lee, W. G.,
2092 Merryfield, W. J., Roulet, N. T. and Scinocca, J. F.: The global carbon cycle in the Canadian Earth system
2093 model (CanESM1): Preindustrial control simulation, *J. Geophys. Res. Biogeosciences*, 115(G3),
2094 doi:10.1029/2008JG000920, 2010.
- 2095 Coleman, K. and Jenkinson, D. S.: RothC-26.3 - A model for the turnover of carbon in soil: Model
2096 description and users guide, Rothamsted Research, Harpenden, U.K. [online] Available from:
2097 https://www.rothamsted.ac.uk/sites/default/files/RothC_guide_WIN.pdf, 1999.
- 2098 Collatz, G., Ribas-Carbo, M. and Berry, J.: Coupled Photosynthesis-Stomatal Conductance Model for
2099 Leaves of C₄ Plants, *Funct. Plant Biol.*, 19(5), 519–538, 1992.
- 2100 Cox, P.: Description of the TRIFFID Dynamic Global Vegetation Model, Hadley Centre Technical Note #
2101 24, UK Met Office. [online] Available from: [https://digital.nmla.metoffice.gov.uk/IO_cc8f146a-d524-
2102 4243-88fc-e3a3bcd782e7/](https://digital.nmla.metoffice.gov.uk/IO_cc8f146a-d524-4243-88fc-e3a3bcd782e7/), 2001.



- 2103 Cramer, W.: Using plant functional types in a global vegetation model, in Smith, T.M., Shugart, H.H. &
2104 Woodward, F.I. (eds.) Plant functional types: their relevance to ecosystem properties and global change,
2105 pp. 271–288, Cambridge University Press, Cambridge., 1997.
- 2106 Decharme, B., Delire, C., Minvielle, M., Colin, J., Vergnes, J.-P., Alias, A., Saint-Martin, D., Séférian, R.,
2107 Sénési, S. and Voldoire, A.: Recent Changes in the ISBA-CTRIP Land Surface System for Use in the CNRM-
2108 CM6 Climate Model and in Global Off-Line Hydrological Applications, *J. Adv. Model. Earth Syst.*, 11(5),
2109 1207–1252, doi:10.1029/2018MS001545, 2019.
- 2110 Delire, C., Séférian, R., Decharme, B., Alkama, R., Carrer, D., Joetzjer, E., Morel, X. and Rocher, M.: The
2111 global land carbon cycle simulated with ISBA, *Journal of Advances in Modeling Earth Systems*, JAMES,
2112 submitted, 2019.
- 2113 Donner, L. J., Wyman, B. L., Hemler, R. S., Horowitz, L. W., Ming, Y., Zhao, M., Golaz, J.-C., Ginoux, P., Lin,
2114 S.-J., Schwarzkopf, M. D., Austin, J., Alaka, G., Cooke, W. F., Delworth, T. L., Freidenreich, S. M., Gordon,
2115 C. T., Griffies, S. M., Held, I. M., Hurlin, W. J., Klein, S. A., Knutson, T. R., Langenhorst, A. R., Lee, H.-C.,
2116 Lin, Y., Magi, B. I., Malyshev, S. L., Milly, P. C. D., Naik, V., Nath, M. J., Pincus, R., Ploshay, J. J.,
2117 Ramaswamy, V., Seman, C. J., Shevliakova, E., Sirutis, J. J., Stern, W. F., Stouffer, R. J., Wilson, R. J.,
2118 Winton, M., Wittenberg, A. T. and Zeng, F.: The Dynamical Core, Physical Parameterizations, and Basic
2119 Simulation Characteristics of the Atmospheric Component AM3 of the GFDL Global Coupled Model CM3,
2120 *J. Clim.*, 24(13), 3484–3519, doi:10.1175/2011JCLI3955.1, 2011.
- 2121 Dunne, J. P., John, J. G., Adcroft, A. J., Griffies, S. M., Hallberg, R. W., Shevliakova, E., Stouffer, R. J.,
2122 Cooke, W., Dunne, K. A., Harrison, M. J., Krasting, J. P., Malyshev, S. L., Milly, P. C. D., Phillipps, P. J.,
2123 Sentman, L. T., Samuels, B. L., Spelman, M. J., Winton, M., Wittenberg, A. T. and Zadeh, N.: GFDL's ESM2
2124 Global Coupled Climate–Carbon Earth System Models. Part I: Physical Formulation and Baseline
2125 Simulation Characteristics, *J. Clim.*, 25(19), 6646–6665, doi:10.1175/JCLI-D-11-00560.1, 2012.
- 2126 Dunne, J. P., John, J. G., Shevliakova, E., Stouffer, R. J., Krasting, J. P., Malyshev, S. L., Milly, P. C. D.,
2127 Sentman, L. T., Adcroft, A. J., Cooke, W., Dunne, K. A., Griffies, S. M., Hallberg, R. W., Harrison, M. J.,
2128 Levy, H., Wittenberg, A. T., Phillips, P. J. and Zadeh, N.: GFDL's ESM2 Global Coupled Climate–Carbon
2129 Earth System Models. Part II: Carbon System Formulation and Baseline Simulation Characteristics, *J.*
2130 *Clim.*, 26(7), 2247–2267, doi:10.1175/JCLI-D-12-00150.1, 2013.
- 2131 Eyring, V., Bony, S., Meehl, G. A., Senior, C. A., Stevens, B., Stouffer, R. J. and Taylor, K. E.: Overview of
2132 the Coupled Model Intercomparison Project Phase 6 (CMIP6) experimental design and organization,
2133 *Geosci. Model Dev.*, 9(5), 1937–1958, doi:10.5194/gmd-9-1937-2016, 2016.
- 2134 Farquhar, G. D., von Caemmerer, S. and Berry, J. A.: A biochemical model of photosynthetic CO₂
2135 assimilation in leaves of C₃ species, *Planta*, 149(1), 78–90, doi:10.1007/BF00386231, 1980.
- 2136 Fichefet, T. and Morales Maqueda, M. A.: Sensitivity of a global sea ice model to the treatment of ice
2137 thermodynamics and dynamics, *J. Geophys. Res. Oceans*, 102(C6), 12609–12646,
2138 doi:10.1029/97JC00480, 1997.
- 2139 Fisher, R. A., Wieder, W. R., Sanderson, B. M., Koven, C. D., Oleson, K. W., Xu, C., Fisher, J. B., Shi, M.,
2140 Walker, A. P. and Lawrence, D. M.: Parametric Controls on Vegetation Responses to Biogeochemical
2141 Forcing in the CLM5, *J. Adv. Model. Earth Syst.*, 11, doi:10.1029/2019MS001609, 2019.



- 2142 Follows, M. J., Ito, T. and Dutkiewicz, S.: On the solution of the carbonate chemistry system in ocean
2143 biogeochemistry models, *Ocean Model.*, 12(3), 290–301,
2144 doi:<https://doi.org/10.1016/j.ocemod.2005.05.004>, 2006.
- 2145 Frame, D. J., Macey, A. H. and Allen, M. R.: Cumulative emissions and climate policy, *Nat. Geosci.*, 7, 692,
2146 2014.
- 2147 Friedlingstein, P., Cox, P., Betts, R., Bopp, L., von Bloh, W., Brovkin, V., Cadule, P., Doney, S., Eby, M.,
2148 Fung, I., Bala, G., John, J., Jones, C., Joos, F., Kato, T., Kawamiya, M., Knorr, W., Lindsay, K., Matthews, H.
2149 D., Raddatz, T., Rayner, P., Reick, C., Roeckner, E., Schnitzler, K.-G., Schnur, R., Strassmann, K., Weaver,
2150 A. J., Yoshikawa, C. and Zeng, N.: Climate–Carbon Cycle Feedback Analysis: Results from the C4MIP
2151 Model Intercomparison, *J. Clim.*, 19(14), 3337–3353, doi:10.1175/JCLI3800.1, 2006.
- 2152 Gillett, N. P., Arora, V. K., Matthews, D. and Allen, M. R.: Constraining the Ratio of Global Warming to
2153 Cumulative CO₂ Emissions Using CMIP5 Simulations, *J. Clim.*, 26(18), 6844–6858, doi:10.1175/JCLI-D-12-
2154 00476.1, 2013.
- 2155 Giorgetta, M. A., Jungclaus, J., Reick, C. H., Legutke, S., Bader, J., Böttinger, M., Brovkin, V., Crueger, T.,
2156 Esch, M., Fieg, K., Glushak, K., Gayler, V., Haak, H., Hollweg, H.-D., Ilyina, T., Kinne, S., Kornblueh, L.,
2157 Matei, D., Mauritsen, T., Mikolajewicz, U., Mueller, W., Notz, D., Pithan, F., Raddatz, T., Rast, S., Redler,
2158 R., Roeckner, E., Schmidt, H., Schnur, R., Segschneider, J., Six, K. D., Stockhause, M., Timmreck, C.,
2159 Wegner, J., Widmann, H., Wieners, K.-H., Claussen, M., Marotzke, J. and Stevens, B.: Climate and carbon
2160 cycle changes from 1850 to 2100 in MPI-ESM simulations for the Coupled Model Intercomparison
2161 Project phase 5, *J. Adv. Model. Earth Syst.*, 5(3), 572–597, doi:10.1002/jame.20038, 2013.
- 2162 Goll, D. S., Brovkin, V., Liski, J., Raddatz, T., Thum, T. and Todd-Brown, K. E. O.: Strong dependence of
2163 CO₂ emissions from anthropogenic land cover change on initial land cover and soil carbon
2164 parametrization, *Glob. Biogeochem. Cycles*, 29(9), 1511–1523, doi:10.1002/2014GB004988, 2015.
- 2165 Goll, D. S., Winkler, A. J., Raddatz, T., Dong, N., Prentice, I. C., Ciais, P. and Brovkin, V.: Carbon–nitrogen
2166 interactions in idealized simulations with JSBACH (version 3.10), *Geosci. Model Dev.*, 10(5), 2009–2030,
2167 doi:10.5194/gmd-10-2009-2017, 2017.
- 2168 Goodwin, P. and Lenton, T. M.: Quantifying the feedback between ocean heating and CO₂ solubility as
2169 an equivalent carbon emission, *Geophys. Res. Lett.*, 36(15), doi:10.1029/2009GL039247, 2009.
- 2170 Goudriaan, J., van Laar, H. H., van Keulen, H. and Louwarse, W.: Photosynthesis, CO₂ and Plant
2171 Production, in *Wheat Growth and Modelling*, edited by W. Day and R. K. Atkin, pp. 107–122, Springer
2172 US, Boston, MA., 1985.
- 2173 Grandpeix, J.-Y. and Lafore, J.-P.: A Density Current Parameterization Coupled with Emanuel’s
2174 Convection Scheme. Part I: The Models, *J. Atmospheric Sci.*, 67(4), 881–897,
2175 doi:10.1175/2009JAS3044.1, 2010.
- 2176 Grandpeix, J.-Y., Lafore, J.-P. and Cheruy, F.: A Density Current Parameterization Coupled with Emanuel’s
2177 Convection Scheme. Part II: 1D Simulations, *J. Atmospheric Sci.*, 67(4), 898–922,
2178 doi:10.1175/2009JAS3045.1, 2010.



- 2179 Gregory, J. M., Jones, C. D., Cadule, P. and Friedlingstein, P.: Quantifying Carbon Cycle Feedbacks, *J.*
2180 *Clim.*, 22(19), 5232–5250, doi:10.1175/2009JCLI2949.1, 2009.
- 2181 Griffies, S. M.: Elements of the Modular Ocean Model (MOM) (2012 release with update), GFDL Ocean
2182 Group Technical report No. 7, NOAA/GFDL., 2014.
- 2183 Gruber, N., Sarmiento, J. L. and Stocker, T. F.: An improved method for detecting anthropogenic CO₂ in
2184 the oceans, *Glob. Biogeochem. Cycles*, 10(4), 809–837, doi:10.1029/96GB01608, 1996.
- 2185 Hajima, T., Tachiiri, K., Ito, A. and Kawamiya, M.: Uncertainty of Concentration–Terrestrial Carbon
2186 Feedback in Earth System Models, *J. Clim.*, 27(9), 3425–3445, doi:10.1175/JCLI-D-13-00177.1, 2014.
- 2187 Hajima, T., Watanabe, M., Yamamoto, A., Tatebe, H., Noguchi, M. A., Abe, M., Ohgaito, R., Ito, A.,
2188 Yamazaki, D., Okajima, H., Ito, A., Takata, K., Ogochi, K., Watanabe, S. and Kawamiya, M.: Description of
2189 the MIROC-ES2L Earth system model and evaluation of its climate–biogeochemical processes and
2190 feedbacks, *Geosci. Model Dev. Discuss.*, 2019, 1–73, doi:10.5194/gmd-2019-275, 2019a.
- 2191 Hajima, T., Abe, M., Ito, A., Ito, A., Kawamiya, M., Noguchi, M. A., Ohgaito, R., Okajima, H., Takata, K.,
2192 Tatebe, H., Yamamoto, A., Watanabe, M., Watanabe, S. and Yamazaki, D.: Model description of a new
2193 Earth system model “MIROC-ES2L” and the sensitivity analysis of the biogeochemical feedbacks, , in
2194 preparation, 2019b.
- 2195 Hasumi, H.: CCSR Ocean Component Model (COCO) version 4.0, University of Tokyo. [online] Available
2196 from: <https://ccsr.aori.u-tokyo.ac.jp/~hasumi/COCO/coco4.pdf>, 2015.
- 2197 Hourdin, F., Couvreur, F. and Menut, L.: Parameterization of the Dry Convective Boundary Layer Based
2198 on a Mass Flux Representation of Thermals, *J. Atmospheric Sci.*, 59(6), 1105–1123, doi:10.1175/1520-
2199 0469(2002)059<1105:POTDCB>2.0.CO;2, 2002.
- 2200 Hourdin, F., Rio, C., Grandpeix, J.-Y., Madeleine, J.-B., Cheruy, F., Rochetin, N., Musat, I., Idelkadi, A.,
2201 Fairhead, L., Foujols, M.-A., Ghattas, J., Mellul, L., Traore, A.-K., Gastineau, G., Dufresne, J.-L., Lefebvre,
2202 M.-P., Millour, E., Vignon, E., Jouaud, J., Bonazzola, M. and Lott, F.: LMDZ6: the improved atmospheric
2203 component of the IPSL coupled model, submitted, 2019.
- 2204 Hunke, E. C. and Lipscomb, W. H.: The Los Alamos sea ice model documentation and software user’s
2205 manual, Version 4.1. LA-CC-06-012, Los Alamos National Laboratory., 2010.
- 2206 Hunke, E. C., Lipscomb, W. H., Turner, A. K., Jeffery, N. and Elliott, S.: CICE: The Los Alamos Sea Ice
2207 Model. Documentation and Software User’s Manual. Version 5.1, T-3 Fluid Dynamics Group, Los Alamos
2208 National Laboratory., 2015.
- 2209 Hurtt, G. C., Frohling, S., Fearon, M. G., Moore, B., Shevliakova, E., Malyshev, S., Pacala, S. W. and
2210 Houghton, R. A.: The underpinnings of land-use history: three centuries of global gridded land-use
2211 transitions, wood-harvest activity, and resulting secondary lands, *Glob. Change Biol.*, 12(7), 1208–1229,
2212 doi:10.1111/j.1365-2486.2006.01150.x, 2006.
- 2213 Ilyina, T., Six, K. D., Segschneider, J., Maier-Reimer, E., Li, H. and Núñez-Riboni, I.: Global ocean
2214 biogeochemistry model HAMOCC: Model architecture and performance as component of the MPI-Earth



- 2215 system model in different CMIP5 experimental realizations, *J. Adv. Model. Earth Syst.*, 5(2), 287–315,
2216 doi:10.1029/2012MS000178, 2013.
- 2217 Ito, A. and Inatomi, M.: Water-Use Efficiency of the Terrestrial Biosphere: A Model Analysis Focusing on
2218 Interactions between the Global Carbon and Water Cycles, *J. Hydrometeorol.*, 13(2), 681–694,
2219 doi:10.1175/JHM-D-10-05034.1, 2012.
- 2220 Ito, A. and Oikawa, T.: A simulation model of the carbon cycle in land ecosystems (Sim-CYCLE): a
2221 description based on dry-matter production theory and plot-scale validation, *Ecol. Model.*, 151(2), 143–
2222 176, doi:https://doi.org/10.1016/S0304-3800(01)00473-2, 2002.
- 2223 Ito, T. and Follows, M. J.: Preformed phosphate, soft tissue pump and atmospheric CO₂, *J. Mar. Res.*,
2224 63(4), 813–839, doi:doi:10.1357/0022240054663231, 2005.
- 2225 Jones, C. D., Arora, V., Friedlingstein, P., Bopp, L., Brovkin, V., Dunne, J., Graven, H., Hoffman, F., Ilyina,
2226 T., John, J. G., Jung, M., Kawamiya, M., Koven, C., Pongratz, J., Raddatz, T., Randerson, J. T. and Zaehle,
2227 S.: C4MIP – The Coupled Climate–Carbon Cycle Model Intercomparison Project: experimental protocol
2228 for CMIP6, *Geosci. Model Dev.*, 9(8), 2853–2880, doi:10.5194/gmd-9-2853-2016, 2016.
- 2229 Katavouta, A., Williams, R. G., Goodwin, P. and Roussenov, V.: Reconciling Atmospheric and Oceanic
2230 Views of the Transient Climate Response to Emissions, *Geophys. Res. Lett.*, 45(12), 6205–6214,
2231 doi:10.1029/2018GL077849, 2018.
- 2232 Koven, C. D., Chambers, J. Q., Georgiou, K., Knox, R., Negron-Juarez, R., Riley, W. J., Arora, V. K., Brovkin,
2233 V., Friedlingstein, P. and Jones, C. D.: Controls on terrestrial carbon feedbacks by productivity versus
2234 turnover in the CMIP5 Earth System Models, *Biogeosciences*, 12(17), 5211–5228, doi:10.5194/bg-12-
2235 5211-2015, 2015.
- 2236 Kowalczyk, E. A., Stevens, L., Law, R. M., Dix, M., Wang, Y. P., Harman, I. N., Haynes, K., Sribnovsky, J.,
2237 Pak, B. and Ziehn, T.: The land surface model component of ACCESS: description and impact on the
2238 simulated surface climatology, *Aust Meteor Oceanogr J*, 63, 65–82, 2013.
- 2239 Krasting, J. P., Blanton, C., McHugh, C., Radhakrishnan, A., John, J. G., Rand, K., Nikonov, S., Vahlenkamp,
2240 H., Zadeh, N. T., Dunne, J. P., Shevliakova, E., Horowitz, L. W., Stock, C., Malyshev, S., Ploshay, J.,
2241 Gauthier, P. P., Naik, V. and Winton, M.: NOAA-GFDL GFDL-ESM4 model output prepared for CMIP6
2242 C4MIP, *Earth Syst. Grid Fed.*, DOI:10.22033/ESGF/CMIP6.1405 [online] Available from: [http://esgf-
node.llnl.gov/search/cmip6/?mip_era=CMIP6&activity_id=C4MIP&institution_id=NOAA-
GFDL&source_id=GFDL-ESM4doi.org/10.22033/ESGF/CMIP6.1405](http://esgf-
2243 node.llnl.gov/search/cmip6/?mip_era=CMIP6&activity_id=C4MIP&institution_id=NOAA-
2244 GFDL&source_id=GFDL-ESM4doi.org/10.22033/ESGF/CMIP6.1405), 2019a.
- 2245 Krasting, J. P., John, J. G., Blanton, C., McHugh, C., Nikonov, S., Radhakrishnan, A., Rand, K., Zadeh, N. T.,
2246 Balaji, V., Durachta, J., Dupuis, C., Menzel, R., Robinson, T., Underwood, S., Vahlenkamp, H., Dunne, K.
2247 A., Gauthier, P. P., Ginoux, P., Griffies, S. M., Hallberg, R., Harrison, M., Hurlin, W., Malyshev, S., Naik, V.,
2248 Paulot, F., Paynter, D. J., Ploshay, J., Schwarzkopf, D. M., Seman, C. J., Silvers, L., Wyman, B., Zeng, Y.,
2249 Adcroft, A., Dunne, J. P., Guo, H., Held, I. M., Horowitz, L. W., Milly, P. C. D., Shevliakova, E., Stock, C.,
2250 Winton, M. and Zhao, M.: NOAA-GFDL GFDL-ESM4 model output prepared for CMIP6 CMIP, *Earth Syst.
2251 Grid Fed.*, DOI:10.22033/ESGF/CMIP6.1407 [online] Available from: [http://esgf-
node.llnl.gov/search/cmip6/?mip_era=CMIP6&activity_id=CMIP&institution_id=NOAA-
GFDL&source_id=GFDL-ESM4doi.org/10.22033/ESGF/CMIP6.1407](http://esgf-
2252 node.llnl.gov/search/cmip6/?mip_era=CMIP6&activity_id=CMIP&institution_id=NOAA-
2253 GFDL&source_id=GFDL-ESM4doi.org/10.22033/ESGF/CMIP6.1407), 2019b.



- 2254 Krinner, G., Viovy, N., de Noblet-Ducoudré, N., Ogée, J., Polcher, J., Friedlingstein, P., Ciais, P., Sitch, S.
2255 and Prentice, I. C.: A dynamic global vegetation model for studies of the coupled atmosphere-biosphere
2256 system: DVGM FOR COUPLED CLIMATE STUDIES, *Glob. Biogeochem. Cycles*, 19(1),
2257 doi:10.1029/2003GB002199, 2005.
- 2258 Lasslop, G., Thonicke, K. and Kloster, S.: SPITFIRE within the MPI Earth system model: Model
2259 development and evaluation, *J. Adv. Model. Earth Syst.*, 6(3), 740–755, doi:10.1002/2013MS000284,
2260 2014.
- 2261 Lauderdale, J. M., Garabato, A. C. N., Oliver, K. I. C., Follows, M. J. and Williams, R. G.: Wind-driven
2262 changes in Southern Ocean residual circulation, ocean carbon reservoirs and atmospheric CO₂, *Clim.*
2263 *Dyn.*, 41(7), 2145–2164, doi:10.1007/s00382-012-1650-3, 2013.
- 2264 Laufkötter, C., John, J. G., Stock, C. A. and Dunne, J. P.: Temperature and oxygen dependence of the
2265 remineralization of organic matter, *Glob. Biogeochem. Cycles*, 31(7), 1038–1050,
2266 doi:10.1002/2017GB005643, 2017.
- 2267 Law, R. M., Ziehn, T., Mearns, R. J., Lenton, A., Chamberlain, M. A., Stevens, L. E., Wang, Y.-P.,
2268 Sribinovsky, J., Bi, D., Yan, H. and Vohralik, P. F.: The carbon cycle in the Australian Community Climate
2269 and Earth System Simulator (ACCESS-ESM1) – Part 1: Model description and pre-industrial simulation,
2270 *Geosci. Model Dev.*, 10(7), 2567–2590, doi:10.5194/gmd-10-2567-2017, 2017.
- 2271 Lawrence, D., Fisher, R., Koven, C., Oleson, K., Swenson, S., Vertenstein, M., Andre, B., Bonan, G.,
2272 Ghimire, B., van Kampenhout, L., Kennedy, D., Kluzek, E., Knox, R., Lawrence, P., Li, F., Li, H.,
2273 Lombardozzi, D., Lu, Y., Perket, J., Riley, W., Sacks, W., Shi, M., Wieder, W. and Xu, C.: Technical
2274 Description of version 5.0 of the Community Land Model (CLM), NCAR, Boulder, USA, 329 pp., 2018.
- 2275 Li, W., Zhang, Y., Shi, X., Zhou, W., Huang, A., Mu, M., Qiu, B. and Ji, J.: Development of the Land Surface
2276 Model BCC_AVIM2.0 and Its Preliminary Performance in LS3MIP/CMIP6, *J. Meteorol. Res.*, 33(4), in
2277 press, doi:10.1007/s13351-019-9016-y, 2019.
- 2278 Lin, S.-J.: A “Vertically Lagrangian” Finite-Volume Dynamical Core for Global Models, *Mon. Weather Rev.*,
2279 132(10), 2293–2307, doi:10.1175/1520-0493(2004)132<2293:AVLFDC>2.0.CO;2, 2004.
- 2280 MacDougall, A. H.: The Transient Response to Cumulative CO₂ Emissions: a Review, *Curr. Clim. Change*
2281 *Rep.*, 2(1), 39–47, doi:10.1007/s40641-015-0030-6, 2016.
- 2282 Madec, G., Romain, B.-B., Pierre-Antoine, B., Clément, B., Diego, B., Daley, C., Jérôme, C., Emanuela, C.,
2283 Andrew, C., Damiano, D., Christian, E., Simona, F., Tim, G., James, H., Doroteaciro, I., Dan, L., Claire, L.,
2284 Tomas, L., Nicolas, M., Sébastien, M., Silvia, M., Julien, P., Clément, R., Dave, S., Andrea, S. and Martin,
2285 V.: NEMO ocean engine., 2017.
- 2286 Maher, N., Milinski, S., Suarez-Gutierrez, L., Botzet, M., Dobrynin, M., Kornblueh, L., Kröger, J., Takano,
2287 Y., Ghosh, R., Hedemann, C., Li, C., Li, H., Manzini, E., Notz, D., Putrasahan, D., Boysen, L., Claussen, M.,
2288 Ilyina, T., Olonscheck, D., Raddatz, T., Stevens, B. and Marotzke, J.: The Max Planck Institute Grand
2289 Ensemble: Enabling the Exploration of Climate System Variability, *J. Adv. Model. Earth Syst.*, 11(7),
2290 2050–2069, doi:10.1029/2019MS001639, 2019.



- 2291 Maier-Reimer, E., Kriest, I., Segschneider, J. and Wetzel, P.: The HAMBURG Ocean Carbon Cycle Model
2292 HAMOCC5.1 - Technical Description Release 1.1, Max Planck Institute for Meteorology, Hamburg,
2293 Germany, 50 pp., 2005.
- 2294 Mann, G. W., Carslaw, K. S., Spracklen, D. V., Ridley, D. A., Manktelow, P. T., Chipperfield, M. P.,
2295 Pickering, S. J. and Johnson, C. E.: Description and evaluation of GLOMAP-mode: a modal global aerosol
2296 microphysics model for the UKCA composition-climate model, *Geosci. Model Dev.*, 3(2), 519–551,
2297 doi:10.5194/gmd-3-519-2010, 2010.
- 2298 Martin, G. M., Milton, S. F., Senior, C. A., Brooks, M. E., Ineson, S., Reichler, T. and Kim, J.: Analysis and
2299 Reduction of Systematic Errors through a Seamless Approach to Modeling Weather and Climate, *J. Clim.*,
2300 23(22), 5933–5957, doi:10.1175/2010JCLI3541.1, 2010.
- 2301 Martin, G. M., Bellouin, N., Collins, W. J., Culverwell, I. D., Halloran, P. R., Hardiman, S. C., Hinton, T. J.,
2302 Jones, C. D., McDonald, R. E., McLaren, A. J., O’Connor, F. M., Roberts, M. J., Rodriguez, J. M.,
2303 Woodward, S., Best, M. J., Brooks, M. E., Brown, A. R., Butchart, N., Dearden, C., Derbyshire, S. H.,
2304 Dharssi, I., Doutriaux-Boucher, M., Edwards, J. M., Falloon, P. D., Gedney, N., Gray, L. J., Hewitt, H. T.,
2305 Hobson, M., Huddleston, M. R., Hughes, J., Ineson, S., Ingram, W. J., James, P. M., Johns, T. C., Johnson,
2306 C. E., Jones, A., Jones, C. P., Joshi, M. M., Keen, A. B., Liddicoat, S., Lock, A. P., Maidens, A. V., Manners, J.
2307 C., Milton, S. F., Rae, J. G. L., Ridley, J. K., Sellar, A., Senior, C. A., Totterdell, I. J., Verhoef, A., Vidale, P. L.
2308 and Wiltshire, A.: The HadGEM2 family of Met Office Unified Model climate configurations, *Geosci.*
2309 *Model Dev.*, 4(3), 723–757, doi:10.5194/gmd-4-723-2011, 2011.
- 2310 Martin, J. H., Knauer, G. A., Karl, D. M. and Broenkow, W. W.: VERTEX: carbon cycling in the northeast
2311 Pacific, *Deep Sea Res. Part Oceanogr. Res. Pap.*, 34(2), 267–285, doi:[https://doi.org/10.1016/0198-](https://doi.org/10.1016/0198-0149(87)90086-0)
2312 [0149\(87\)90086-0](https://doi.org/10.1016/0198-0149(87)90086-0), 1987.
- 2313 Mathiot, P., Jenkins, A., Harris, C. and Madec, G.: Explicit representation and parametrised impacts of
2314 under ice shelf seas in the Σz^{ast} coordinate ocean model NEMO 3.6, *Geosci. Model Dev.*, 10(7),
2315 2849–2874, doi:10.5194/gmd-10-2849-2017, 2017.
- 2316 Matthews, H. D., Gillett, N. P., Stott, P. A. and Zickfeld, K.: The proportionality of global warming to
2317 cumulative carbon emissions, *Nature*, 459(7248), 829–832, doi:10.1038/nature08047, 2009.
- 2318 Mauritsen, T., Bader, J., Becker, T., Behrens, J., Bittner, M., Brokopf, R., Brovkin, V., Claussen, M.,
2319 Crueger, T., Esch, M., Fast, I., Fiedler, S., Fläschner, D., Gayler, V., Giorgetta, M., Goll, D. S., Haak, H.,
2320 Hagemann, S., Hedemann, C., Hohenegger, C., Ilyina, T., Jahns, T., Jimenéz-de-la-Cuesta, D., Jungclaus, J.,
2321 Kleinen, T., Kloster, S., Kracher, D., Kinne, S., Kleberg, D., Lasslop, G., Kornblueh, L., Marotzke, J., Matei,
2322 D., Meraner, K., Mikolajewicz, U., Modali, K., Möbis, B., Müller, W. A., Nabel, J. E. M. S., Nam, C. C. W.,
2323 Notz, D., Nyawira, S.-S., Paulsen, H., Peters, K., Pincus, R., Pohlmann, H., Pongratz, J., Popp, M., Raddatz,
2324 T. J., Rast, S., Redler, R., Reick, C. H., Rohrschneider, T., Schemann, V., Schmidt, H., Schnur, R.,
2325 Schulzweida, U., Six, K. D., Stein, L., Stemmler, I., Stevens, B., von Storch, J.-S., Tian, F., Voigt, A., Vrese,
2326 P., Wieners, K.-H., Wilkenskjaeld, S., Winkler, A. and Roeckner, E.: Developments in the MPI-M Earth
2327 System Model version 1.2 (MPI-ESM1.2) and Its Response to Increasing CO₂, *J. Adv. Model. Earth Syst.*,
2328 11(4), 998–1038, doi:10.1029/2018MS001400, 2019.
- 2329 Millar, R., Allen, M., Rogelj, J. and Friedlingstein, P.: The cumulative carbon budget and its implications,
2330 *Oxf. Rev. Econ. Policy*, 32(2), 323–342, doi:10.1093/oxrep/grw009, 2016.



- 2331 Millar, R. J., Fuglestedt, J. S., Friedlingstein, P., Rogelj, J., Grubb, M. J., Matthews, H. D., Skeie, R. B.,
2332 Forster, P. M., Frame, D. J. and Allen, M. R.: Emission budgets and pathways consistent with limiting
2333 warming to 1.5 °C, *Nat. Geosci.*, 10, 741, 2017.
- 2334 Milly, P. C. D., Malyshev, S. L., Shevliakova, E., Dunne, K. A., Findell, K. L., Gleeson, T., Liang, Z., Philipps,
2335 P., Stouffer, R. J. and Swenson, S.: An Enhanced Model of Land Water and Energy for Global Hydrologic
2336 and Earth-System Studies, *J. Hydrometeorol.*, 15(5), 1739–1761, doi:10.1175/JHM-D-13-0162.1, 2014.
- 2337 Morgenstern, O., Braesicke, P., O'Connor, F. M., Bushell, A. C., Johnson, C. E., Osprey, S. M. and Pyle, J.
2338 A.: Evaluation of the new UKCA climate-composition model – Part 1: The stratosphere, *Geosci. Model
2339 Dev.*, 2(1), 43–57, doi:10.5194/gmd-2-43-2009, 2009.
- 2340 Morgenstern, O., Hegglin, M. I., Rozanov, E., O'Connor, F. M., Abraham, N. L., Akiyoshi, H., Archibald, A.
2341 T., Bekki, S., Butchart, N., Chipperfield, M. P., Deushi, M., Dhomse, S. S., Garcia, R. R., Hardiman, S. C.,
2342 Horowitz, L. W., Jöckel, P., Josse, B., Kinnison, D., Lin, M., Mancini, E., Manyin, M. E., Marchand, M.,
2343 Marécal, V., Michou, M., Oman, L. D., Pitari, G., Plummer, D. A., Revell, L. E., Saint-Martin, D., Schofield,
2344 R., Stenke, A., Stone, K., Sudo, K., Tanaka, T. Y., Tilmes, S., Yamashita, Y., Yoshida, K. and Zeng, G.:
2345 Review of the global models used within phase 1 of the Chemistry–Climate Model Initiative (CCMI),
2346 *Geosci. Model Dev.*, 10(2), 639–671, doi:10.5194/gmd-10-639-2017, 2017.
- 2347 O'Connor, F. M., Johnson, C. E., Morgenstern, O., Abraham, N. L., Braesicke, P., Dalvi, M., Folberth, G. A.,
2348 Sanderson, M. G., Telford, P. J., Voulgarakis, A., Young, P. J., Zeng, G., Collins, W. J. and Pyle, J. A.:
2349 Evaluation of the new UKCA climate-composition model – Part 2: The Troposphere, *Geosci. Model Dev.*,
2350 7(1), 41–91, doi:10.5194/gmd-7-41-2014, 2014.
- 2351 Oke, P. R., Griffin, D. A., Schiller, A., Matear, R. J., Fiedler, R., Mansbridge, J., Lenton, A., Cahill, M.,
2352 Chamberlain, M. A. and Ridgway, K.: Evaluation of a near-global eddy-resolving ocean model, *Geosci.
2353 Model Dev.*, 6(3), 591–615, doi:10.5194/gmd-6-591-2013, 2013.
- 2354 Orr, J. C. and Epitalon, J.-M.: Improved routines to model the ocean carbonate system: mocsy 2.0,
2355 *Geosci. Model Dev.*, 8(3), 485–499, doi:10.5194/gmd-8-485-2015, 2015.
- 2356 Orr, J. C., Najjar, R. G., Aumont, O., Bopp, L., Bullister, J. L., Danabasoglu, G., Doney, S. C., Dunne, J. P.,
2357 Dutay, J.-C., Graven, H., Griffies, S. M., John, J. G., Joos, F., Levin, I., Lindsay, K., Matear, R. J., McKinley,
2358 G. A., Mouchet, A., Oschlies, A., Romanou, A., Schlitzer, R., Tagliabue, A., Tanhua, T. and Yool, A.:
2359 Biogeochemical protocols and diagnostics for the CMIP6 Ocean Model Intercomparison Project (OMIP),
2360 *Geosci. Model Dev.*, 10(6), 2169–2199, doi:10.5194/gmd-10-2169-2017, 2017.
- 2361 Parton, W. J., Stewart, J. W. B. and Cole, C. V.: Dynamics of C, N, P and S in grassland soils: a model,
2362 *Biogeochemistry*, 5(1), 109–131, doi:10.1007/BF02180320, 1988.
- 2363 Paulsen, H., Ilyina, T., Six, K. D. and Stemmler, I.: Incorporating a prognostic representation of marine
2364 nitrogen fixers into the global ocean biogeochemical model HAMOCC, *J. Adv. Model. Earth Syst.*, 9(1),
2365 438–464, doi:10.1002/2016MS000737, 2017.
- 2366 Plattner, G.-K., Knutti, R., Joos, F., Stocker, T. F., von Bloh, W., Brovkin, V., Cameron, D., Driesschaert, E.,
2367 Dutkiewicz, S., Eby, M., Edwards, N. R., Fichefet, T., Hargreaves, J. C., Jones, C. D., Loutre, M. F.,
2368 Matthews, H. D., Mouchet, A., Müller, S. A., Nawrath, S., Price, A., Sokolov, A., Strassmann, K. M. and



- 2369 Weaver, A. J.: Long-Term Climate Commitments Projected with Climate–Carbon Cycle Models, *J. Clim.*,
2370 21(12), 2721–2751, doi:10.1175/2007JCLI1905.1, 2008.
- 2371 Prentice, I. C., Cramer, W., Harrison, S. P., Leemans, R., Monserud, R. A. and Solomon, A. M.: A Global
2372 Biome Model Based on Plant Physiology and Dominance, Soil Properties and Climate, *J. Biogeogr.*, 19(2),
2373 117–134, 1992.
- 2374 Qian, H., Joseph, R. and Zeng, N.: Enhanced terrestrial carbon uptake in the Northern High Latitudes in
2375 the 21st century from the Coupled Carbon Cycle Climate Model Intercomparison Project model
2376 projections, *Glob. Change Biol.*, 16(2), 641–656, doi:10.1111/j.1365-2486.2009.01989.x, 2010.
- 2377 Rabin, S. S., Ward, D. S., Malyshev, S. L., Magi, B. I., Shevliakova, E. and Pacala, S. W.: A fire model with
2378 distinct crop, pasture, and non-agricultural burning: use of new data and a model-fitting algorithm for
2379 FINAL.1, *Geosci. Model Dev.*, 11(2), 815–842, doi:10.5194/gmd-11-815-2018, 2018.
- 2380 Reick, C. H., Raddatz, T., Brovkin, V. and Gayler, V.: Representation of natural and anthropogenic land
2381 cover change in MPI-ESM, *J. Adv. Model. Earth Syst.*, 5(3), 459–482, doi:10.1002/jame.20022, 2013.
- 2382 Ridley, J. K., Blockley, E. W., Keen, A. B., Rae, J. G. L., West, A. E. and Schroeder, D.: The sea ice model
2383 component of HadGEM3-GC3.1, *Geosci. Model Dev.*, 11(2), 713–723, doi:10.5194/gmd-11-713-2018,
2384 2018.
- 2385 Rio, C. and Hourdin, F.: A Thermal Plume Model for the Convective Boundary Layer: Representation of
2386 Cumulus Clouds, *J. Atmospheric Sci.*, 65(2), 407–425, doi:10.1175/2007JAS2256.1, 2008.
- 2387 Rio, C., Hourdin, F., Couvreux, F. and Jam, A.: Resolved Versus Parametrized Boundary-Layer Plumes.
2388 Part II: Continuous Formulations of Mixing Rates for Mass-Flux Schemes, *Bound.-Layer Meteorol.*,
2389 135(3), 469–483, doi:10.1007/s10546-010-9478-z, 2010.
- 2390 Rogelj, J., Forster, P. M., Kriegler, E., Smith, C. J. and Séférian, R.: Estimating and tracking the remaining
2391 carbon budget for stringent climate targets, *Nature*, 571(7765), 335–342, doi:10.1038/s41586-019-
2392 1368-z, 2019.
- 2393 Rousset, C., Vancoppenolle, M., Madec, G., Fichet, T., Flavoni, S., Barthélemy, A., Benshila, R., Chanut,
2394 J., Levy, C., Masson, S. and Vivier, F.: The Louvain-La-Neuve sea ice model LIM3.6: global and regional
2395 capabilities, *Geosci. Model Dev.*, 8(10), 2991–3005, doi:10.5194/gmd-8-2991-2015, 2015.
- 2396 Roy, T., Bopp, L., Gehlen, M., Schneider, B., Cadule, P., Frölicher, T. L., Segschneider, J., Tjiputra, J.,
2397 Heinze, C. and Joos, F.: Regional Impacts of Climate Change and Atmospheric CO₂ on Future Ocean
2398 Carbon Uptake: A Multimodel Linear Feedback Analysis, *J. Clim.*, 24(9), 2300–2318,
2399 doi:10.1175/2010JCLI3787.1, 2011.
- 2400 Salas Mélia, D.: A global coupled sea ice–ocean model, *Ocean Model.*, 4(2), 137–172,
2401 doi:[https://doi.org/10.1016/S1463-5003\(01\)00015-4](https://doi.org/10.1016/S1463-5003(01)00015-4), 2002.
- 2402 von Salzen, K., Scinocca, J. F., McFarlane, N. A., Li, J., Cole, J. N. S., Plummer, D., Verseghy, D., Reader, M.,
2403 C., Ma, X., Lazare, M. and Solheim, L.: The Canadian Fourth Generation Atmospheric Global Climate
2404 Model (CanAM4). Part I: Representation of Physical Processes, *Atmosphere-Ocean*, 51(1), 104–125,
2405 doi:10.1080/07055900.2012.755610, 2013.



- 2406 Schwinger, J. and Tjiputra, J.: Ocean Carbon Cycle Feedbacks Under Negative Emissions, *Geophys. Res. Lett.*, 45(10), 5062–5070, doi:10.1029/2018GL077790, 2018.
- 2408 Schwinger, J., Tjiputra, J. F., Heinze, C., Bopp, L., Christian, J. R., Gehlen, M., Ilyina, T., Jones, C. D., Salas-Mélia, D., Segschneider, J., Séférian, R. and Totterdell, I.: Nonlinearity of Ocean Carbon Cycle Feedbacks in CMIP5 Earth System Models, *J. Clim.*, 27(11), 3869–3888, doi:10.1175/JCLI-D-13-00452.1, 2014.
- 2411 Schwinger, J., Goris, N., Tjiputra, J. F., Kriest, I., Bentsen, M., Bethke, I., Ilicak, M., Assmann, K. M. and Heinze, C.: Evaluation of NorESM-OC (versions 1 and 1.2), the ocean carbon-cycle stand-alone configuration of the Norwegian Earth System Model (NorESM1), *Geosci. Model Dev.*, 9(8), 2589–2622, doi:10.5194/gmd-9-2589-2016, 2016.
- 2415 Séférian, R., Delire, C., Decharme, B., Voldoire, A., Salas y Melia, D., Chevallier, M., Saint-Martin, D., Aumont, O., Calvet, J.-C., Carrer, D., Douville, H., Franchistéguy, L., Joetzjer, E. and Sénési, S.: Development and evaluation of CNRM Earth system model – CNRM-ESM1, *Geosci. Model Dev.*, 9(4), 1423–1453, doi:10.5194/gmd-9-1423-2016, 2016.
- 2419 Séférian, R., Nabat, P., Michou, M., Saint-Martin, D., Voldoire, A., Colin, J., Decharme, B., Delire, C., Berthet, S., Chevallier, M., Sénési, S., Franchistéguy, L., Vial, J., Mallet, M., Joetzjer, E., Geoffroy, O., Guérémy, J.-F., Moine, M.-P., Msadek, R., Ribes, A., Rocher, M., Roehrig, R., Salas-y-Mélia, D., Sanchez, E., Terray, L., Valcke, S., Waldman, R., Aumont, O., Bopp, L., Deshayes, J., Éthé, C. and Madec, G.: Evaluation of CNRM Earth-System model, CNRM-ESM2-1 : role of Earth system processes in present-day and future climate, *J. Adv. Model. Earth Syst.*, submitted, 2019.
- 2425 Sellar, A. A., Jones, C. G., Mulcahy, J., Tang, Y., Yool, A., Wiltshire, A., O’Connor, F. M., Stringer, M., Hill, R., Palmieri, J., Woodward, S., de Mora, L., Kuhlbrodt, T., Rumbold, S., Kelley, D. I., Ellis, R., Johnson, C. E., Walton, J., Abraham, N. L., Andrews, M. B., Andrews, T., Archibald, A. T., Berthou, S., Burke, E., Blockley, E., Carslaw, K., Dalvi, M., Edwards, J., Folberth, G. A., Gedney, N., Griffiths, P. T., Harper, A. B., Hendry, M. A., Hewitt, A. J., Johnson, B., Jones, A., Jones, C. D., Keeble, J., Liddicoat, S., Morgenstern, O., Parker, R. J., Predoi, V., Robertson, E., Siahann, A., Smith, R. S., Swaminathan, R., Woodhouse, M. T., Zeng, G. and Zerroukat, M.: UKESM1: Description and evaluation of the UK Earth System Model, *J. Adv. Model. Earth Syst.*, accepted, doi:10.1029/2019MS001739, 2019.
- 2433 Skinner, C. B., Poulsen, C. J., Chadwick, R., Diffenbaugh, N. S. and Fiorella, R. P.: The Role of Plant CO₂ Physiological Forcing in Shaping Future Daily-Scale Precipitation, *J. Clim.*, 30(7), 2319–2340, doi:10.1175/JCLI-D-16-0603.1, 2017.
- 2436 Stock, C. A., Dunne, J. P. and John, J. G.: Drivers of trophic amplification of ocean productivity trends in a changing climate, *Biogeosciences*, 11(24), 7125–7135, doi:10.5194/bg-11-7125-2014, 2014a.
- 2438 Stock, C. A., Dunne, J. P. and John, J. G.: Global-scale carbon and energy flows through the marine planktonic food web: An analysis with a coupled physical–biological model, *Prog. Oceanogr.*, 120, 1–28, doi:10.1016/j.pocean.2013.07.001, 2014b.
- 2441 Storkey, D., Blaker, A. T., Mathiot, P., Megann, A., Aksenov, Y., Blockley, E. W., Calvert, D., Graham, T., Hewitt, H. T., Hyder, P., Kuhlbrodt, T., Rae, J. G. L. and Sinha, B.: UK Global Ocean GO6 and GO7: a traceable hierarchy of model resolutions, *Geosci. Model Dev.*, 11(8), 3187–3213, doi:10.5194/gmd-11-3187-2018, 2018.



- 2445 Sulman, B. N., Shevliakova, E., Brzostek, E. R., Kivlin, S. N., Malyshev, S., Menge, D. N. L. and Zhang, X.:
2446 Diverse Mycorrhizal Associations Enhance Terrestrial C Storage in a Global Model, *Glob. Biogeochem.*
2447 *Cycles*, 33(4), 501–523, doi:10.1029/2018GB005973, 2019.
- 2448 Swart, N. C., Cole, J. N. S., Kharin, V. V., Lazare, M., Scinocca, J. F., Gillett, N. P., Anstey, J., Arora, V.,
2449 Christian, J. R., Hanna, S., Jiao, Y., Lee, W. G., Majaess, F., Saenko, O. A., Seiler, C., Seinen, C., Shao, A.,
2450 Solheim, L., von Salzen, K., Yang, D. and Winter, B.: The Canadian Earth System Model version 5
2451 (CanESM5.0.3), *Geosci. Model Dev. Discuss.*, 2019, 1–68, doi:10.5194/gmd-2019-177, 2019.
- 2452 Takata, K., Emori, S. and Watanabe, T.: Development of the minimal advanced treatments of surface
2453 interaction and runoff, *Glob. Planet. Change*, 38(1), 209–222, doi:https://doi.org/10.1016/S0921-
2454 8181(03)00030-4, 2003.
- 2455 Takemura, T., Okamoto, H., Maruyama, Y., Numaguti, A., Higurashi, A. and Nakajima, T.: Global three-
2456 dimensional simulation of aerosol optical thickness distribution of various origins, *J. Geophys. Res.*
2457 *Atmospheres*, 105(D14), 17853–17873, doi:10.1029/2000JD900265, 2000.
- 2458 Tatebe, H., Tanaka, Y., Komuro, Y. and Hasumi, H.: Impact of deep ocean mixing on the climatic mean
2459 state in the Southern Ocean, *Sci. Rep.*, 8(1), 14479, doi:10.1038/s41598-018-32768-6, 2018.
- 2460 Tatebe, H., Ogura, T., Nitta, T., Komuro, Y., Ogochi, K., Takemura, T., Sudo, K., Sekiguchi, M., Abe, M.,
2461 Saito, F., Chikira, M., Watanabe, S., Mori, M., Hirota, N., Kawatani, Y., Mochizuki, T., Yoshimura, K.,
2462 Takata, K., O’ishi, R., Yamazaki, D., Suzuki, T., Kurogi, M., Kataoka, T., Watanabe, M. and Kimoto, M.:
2463 Description and basic evaluation of simulated mean state, internal variability, and climate sensitivity in
2464 MIROC6, *Geosci. Model Dev.*, 12(7), 2727–2765, doi:10.5194/gmd-12-2727-2019, 2019.
- 2465 Taylor, K. E., Stouffer, R. J. and Meehl, G. A.: An Overview of CMIP5 and the Experiment Design, *Bull. Am.*
2466 *Meteorol. Soc.*, 93(4), 485–498, doi:10.1175/BAMS-D-11-00094.1, 2012.
- 2467 Tjiputra, J. F., Assmann, K., Bentsen, M., Bethke, I., Otter\aa, O. H., Sturm, C. and Heinze, C.: Bergen
2468 Earth system model (BCM-C): model description and regional climate-carbon cycle feedbacks
2469 assessment, *Geosci. Model Dev.*, 3(1), 123–141, doi:10.5194/gmd-3-123-2010, 2010.
- 2470 Tjiputra, J. F., Roelandt, C., Bentsen, M., Lawrence, D. M., Lorentzen, T., Schwinger, J., Seland, Ø. and
2471 Heinze, C.: Evaluation of the carbon cycle components in the Norwegian Earth System Model (NorESM),
2472 *Geosci. Model Dev.*, 6(2), 301–325, doi:10.5194/gmd-6-301-2013, 2013.
- 2473 Valcke, S.: The OASIS3 coupler: a European climate modelling community software, *Geosci. Model Dev.*,
2474 6(2), 373–388, doi:10.5194/gmd-6-373-2013, 2013.
- 2475 Vancoppenolle, M., Fichefet, T. and Goosse, H.: Simulating the mass balance and salinity of Arctic and
2476 Antarctic sea ice. 2. Importance of sea ice salinity variations, *Ocean Model.*, 27(1), 54–69,
2477 doi:https://doi.org/10.1016/j.ocemod.2008.11.003, 2009.
- 2478 Versegny, D. L.: The Canadian land surface scheme (CLASS): Its history and future, *Atmosphere-Ocean*,
2479 38(1), 1–13, doi:10.1080/07055900.2000.9649637, 2000.
- 2480 Walters, D., Baran, A. J., Boutle, I., Brooks, M., Earnshaw, P., Edwards, J., Furtado, K., Hill, P., Lock, A.,
2481 Manners, J., Morcrette, C., Mulcahy, J., Sanchez, C., Smith, C., Stratton, R., Tennant, W., Tomassini, L.,



- 2482 Van Weverberg, K., Vosper, S., Willett, M., Browse, J., Bushell, A., Carslaw, K., Dalvi, M., Essery, R.,
2483 Gedney, N., Hardiman, S., Johnson, B., Johnson, C., Jones, A., Jones, C., Mann, G., Milton, S., Rumbold,
2484 H., Sellar, A., Ujiie, M., Whittall, M., Williams, K. and Zerroukat, M.: The Met Office Unified Model Global
2485 Atmosphere 7.0/7.1 and JULES Global Land 7.0 configurations, *Geosci. Model Dev.*, 12(5), 1909–1963,
2486 doi:10.5194/gmd-12-1909-2019, 2019.
- 2487 Wang, Y. P., Law, R. M. and Pak, B.: A global model of carbon, nitrogen and phosphorus cycles for the
2488 terrestrial biosphere, *Biogeosciences*, 7(7), 2261–2282, doi:10.5194/bg-7-2261-2010, 2010.
- 2489 Wang, Y.-P. and Leuning, R.: A two-leaf model for canopy conductance, photosynthesis and partitioning
2490 of available energy I: Model description and comparison with a multi-layered model, *Agric. For.*
2491 *Meteorol.*, 91(1), 89–111, doi:https://doi.org/10.1016/S0168-1923(98)00061-6, 1998.
- 2492 Wanninkhof, R.: Relationship between wind speed and gas exchange over the ocean revisited, *Limnol.*
2493 *Oceanogr. Methods*, 12(6), 351–362, doi:10.4319/lom.2014.12.351, 2014.
- 2494 Watanabe, M., Suzuki, T., O’ishi, R., Komuro, Y., Watanabe, S., Emori, S., Takemura, T., Chikira, M.,
2495 Ogura, T., Sekiguchi, M., Takata, K., Yamazaki, D., Yokohata, T., Nozawa, T., Hasumi, H., Tatebe, H. and
2496 Kimoto, M.: Improved Climate Simulation by MIROC5: Mean States, Variability, and Climate Sensitivity, *J.*
2497 *Clim.*, 23(23), 6312–6335, doi:10.1175/2010JCLI3679.1, 2010.
- 2498 Watanabe, S., Hajima, T., Sudo, K., Nagashima, T., Takemura, T., Okajima, H., Nozawa, T., Kawase, H.,
2499 Abe, M., Yokohata, T., Ise, T., Sato, H., Kato, E., Takata, K., Emori, S. and Kawamiya, M.: MIROC-ESM
2500 2010: model description and basic results of CMIP5-20c3m experiments, *Geosci. Model Dev.*, 4(4), 845–
2501 872, doi:10.5194/gmd-4-845-2011, 2011.
- 2502 Weng, E. S., Malyshev, S., Lichstein, J. W., Farrior, C. E., Dybzinski, R., Zhang, T., Shevliakova, E. and
2503 Pacala, S. W.: Scaling from individual trees to forests in an Earth system modeling framework using a
2504 mathematically tractable model of height-structured competition, *Biogeosciences*, 12(9), 2655–2694,
2505 doi:10.5194/bg-12-2655-2015, 2015.
- 2506 Wenzel, S., Cox, P. M., Eyring, V. and Friedlingstein, P.: Emergent constraints on climate-carbon cycle
2507 feedbacks in the CMIP5 Earth system models, *J. Geophys. Res. Biogeosciences*, 119(5), 794–807,
2508 doi:10.1002/2013JG002591, 2014.
- 2509 Wieder, W. R., Lawrence, D. M., Fisher, R. A., Bonan, G. B., Cheng, S. J., Goodale, C. L., Grandy, A. S.,
2510 Koven, C. D., Lombardozzi, D. L., Oleson, K. W. and Thomas, R. Q.: Beyond static benchmarking: Using
2511 experimental manipulations to evaluate land model assumptions, *Glob. Biogeochem. Cycles*,
2512 0(accepted), doi:10.1029/2018GB006141, 2019.
- 2513 Williams, K. D., Copsey, D., Blockley, E. W., Bodas-Salcedo, A., Calvert, D., Comer, R., Davis, P., Graham,
2514 T., Hewitt, H. T., Hill, R., Hyder, P., Ineson, S., Johns, T. C., Keen, A. B., Lee, R. W., Megann, A., Milton, S.
2515 F., Rae, J. G. L., Roberts, M. J., Scaife, A. A., Schiemann, R., Storkey, D., Thorpe, L., Watterson, I. G.,
2516 Walters, D. N., West, A., Wood, R. A., Woollings, T. and Xavier, P. K.: The Met Office Global Coupled
2517 Model 3.0 and 3.1 (GC3.0 and GC3.1) Configurations, *J. Adv. Model. Earth Syst.*, 10(2), 357–380,
2518 doi:10.1002/2017MS001115, 2018.
- 2519 Williams, R. G. and Follows, M. J.: *Ocean Dynamics and the Carbon Cycle: Principles and Mechanisms*,
2520 Cambridge University Press., 2011.



- 2521 Williams, R. G., Goodwin, P., Roussenov, V. M. and Bopp, L.: A framework to understand the transient
2522 climate response to emissions, *Environ. Res. Lett.*, 11(1), 015003, doi:10.1088/1748-9326/11/1/015003,
2523 2016.
- 2524 Williams, R. G., Roussenov, V., Goodwin, P., Resplandy, L. and Bopp, L.: Sensitivity of Global Warming to
2525 Carbon Emissions: Effects of Heat and Carbon Uptake in a Suite of Earth System Models, *J. Clim.*, 30(23),
2526 9343–9363, doi:10.1175/JCLI-D-16-0468.1, 2017.
- 2527 Williams, R. G., Katavouta, A. and Goodwin, P.: Carbon-cycle feedbacks operating in the climate system,
2528 *Curr. Clim. Change Rep.*, in press, 2019.
- 2529 Wu, T., Yu, R., Zhang, F., Wang, Z., Dong, M., Wang, L., Jin, X., Chen, D. and Li, L.: The Beijing Climate
2530 Center atmospheric general circulation model: description and its performance for the present-day
2531 climate, *Clim. Dyn.*, 34(1), 123–147, doi:10.1007/s00382-008-0487-2, 2008.
- 2532 Wu, T., Li, W., Ji, J., Xin, X., Li, L., Wang, Z., Zhang, Y., Li, J., Zhang, F., Wei, M., Shi, X., Wu, F., Zhang, L.,
2533 Chu, M., Jie, W., Liu, Y., Wang, F., Liu, X., Li, Q., Dong, M., Liang, X., Gao, Y. and Zhang, J.: Global carbon
2534 budgets simulated by the Beijing Climate Center Climate System Model for the last century, *J. Geophys.*
2535 *Res. Atmospheres*, 118(10), 4326–4347, doi:10.1002/jgrd.50320, 2013.
- 2536 Wu, T., Lu, Y., Fang, Y., Xin, X., Li, L., Li, W., Jie, W., Zhang, J., Liu, Y., Zhang, L., Zhang, F., Zhang, Y., Wu,
2537 F., Li, J., Chu, M., Wang, Z., Shi, X., Liu, X., Wei, M., Huang, A., Zhang, Y. and Liu, X.: The Beijing Climate
2538 Center Climate System Model (BCC-CSM): the main progress from CMIP5 to CMIP6, *Geosci. Model Dev.*,
2539 12(4), 1573–1600, doi:10.5194/gmd-12-1573-2019, 2019.
- 2540 Wullschleger, S. D., Epstein, H. E., Box, E. O., Euskirchen, E. S., Goswami, S., Iversen, C. M., Kattge, J.,
2541 Norby, R. J., van Bodegom, P. M. and Xu, X.: Plant functional types in Earth system models: past
2542 experiences and future directions for application of dynamic vegetation models in high-latitude
2543 ecosystems, *Ann. Bot.*, 114(1), 1–16, doi:10.1093/aob/mcu077, 2014.
- 2544 Yamada, T.: Simulations of Nocturnal Drainage Flows by a q2l Turbulence Closure Model, *J. Atmospheric*
2545 *Sci.*, 40(1), 91–106, doi:10.1175/1520-0469(1983)040<0091:SONDFB>2.0.CO;2, 1983.
- 2546 Yin, X.: Responses of leaf nitrogen concentration and specific leaf area to atmospheric CO₂ enrichment:
2547 a retrospective synthesis across 62 species, *Glob. Change Biol.*, 8(7), 631–642, doi:10.1046/j.1365-
2548 2486.2002.00497.x, 2002.
- 2549 Yool, A., Popova, E. E. and Anderson, T. R.: MEDUSA-2.0: an intermediate complexity biogeochemical
2550 model of the marine carbon cycle for climate change and ocean acidification studies, *Geosci. Model*
2551 *Dev.*, 6(5), 1767–1811, doi:10.5194/gmd-6-1767-2013, 2013.
- 2552 Yoshikawa, C., Kawamiya, M., Kato, T., Yamanaka, Y. and Matsuno, T.: Geographical distribution of the
2553 feedback between future climate change and the carbon cycle, *J. Geophys. Res. Biogeosciences*,
2554 113(G3), doi:10.1029/2007JG000570, 2008.
- 2555 Zhao, M., Golaz, J.-C., Held, I. M., Guo, H., Balaji, V., Benson, R., Chen, J.-H., Chen, X., Donner, L. J.,
2556 Dunne, J. P., Dunne, K., Durachta, J., Fan, S.-M., Freidenreich, S. M., Garner, S. T., Ginoux, P., Harris, L.
2557 M., Horowitz, L. W., Krasting, J. P., Langenhorst, A. R., Liang, Z., Lin, P., Lin, S.-J., Malyshev, S. L., Mason,
2558 E., Milly, P. C. D., Ming, Y., Naik, V., Paulot, F., Paynter, D., Phillipps, P., Radhakrishnan, A., Ramaswamy,



- 2559 V., Robinson, T., Schwarzkopf, D., Seman, C. J., Shevliakova, E., Shen, Z., Shin, H., Silvers, L. G., Wilson, J.
2560 R., Winton, M., Wittenberg, A. T., Wyman, B. and Xiang, B.: The GFDL Global Atmosphere and Land
2561 Model AM4.0/LM4.0: 1. Simulation Characteristics With Prescribed SSTs, *J. Adv. Model. Earth Syst.*,
2562 10(3), 691–734, doi:10.1002/2017MS001208, 2018.
- 2563 Zickfeld, K., Eby, M., Matthews, H. D., Schmittner, A. and Weaver, A. J.: Nonlinearity of Carbon Cycle
2564 Feedbacks, *J. Clim.*, 24(16), 4255–4275, doi:10.1175/2011JCLI3898.1, 2011.
- 2565 Ziehn, T., Lenton, A., Law, R. M., Matear, R. J. and Chamberlain, M. A.: The carbon cycle in the Australian
2566 Community Climate and Earth System Simulator (ACCESS-ESM1) – Part 2: Historical simulations, *Geosci.*
2567 *Model Dev.*, 10(7), 2591–2614, doi:10.5194/gmd-10-2591-2017, 2017.
- 2568
- 2569